CHAPTER 4 RESULTS AND DISCUSSION

4.1 Introduction

This research involved the syntheses and characterization (structural, thermal, magnetic and mesomorphic properties) of cobalt(II) and iron(II) complexes with spin-crossover and mesogenic properties. The complexes (total of 14) were of general formula $[M(L^n)_2]X_2$, where M = Co(II), Fe(II), L^n = Schiff bases formed from 2,6-pyridinedicarboxaldehyde and 1-aminoalkanes ($C_nH_{2n+1}NH_2$) of different chain lengths (n=6, 8, 10, 12, 14, 16), and X = BF_4, ClO_4 and PF_6. These complexes were synthesized by a one-pot method.

4.2 $[Co(L^n)_2](BF_4)_2$

The first part of this research was changing the length of the alkyl chain only, while maintaining the anion as BF_4^- ion. The objective was to study the 'fastening' effect of the alkyl chain on the spin-crossover [1] and mesogenic properties.

4.2.1 $[Co(L^6)_2](BF_4)_2.½H_2O$

2,6-Pyridinedicarboxaldehyde, 1-aminohexane and $Co(BF_4)_2.6H_2O$ reacted in methanol to form a red-brick powder (**Complex 1**) in good yield (89.1%). The powder was readily soluble in CH_3OH, CH_3CH_2OH, CH_3Cl, CH_2Cl_2 and $CH_2(NO_2)_2$.

(a) Deduction of structural formula

The structure of **Complex 1** (**Figure 4.1**) was deduced based on the results of the elemental analyses, ESI mass spectrometry, FTIR and UV-visible spectroscopies, and magnetic susceptibility.

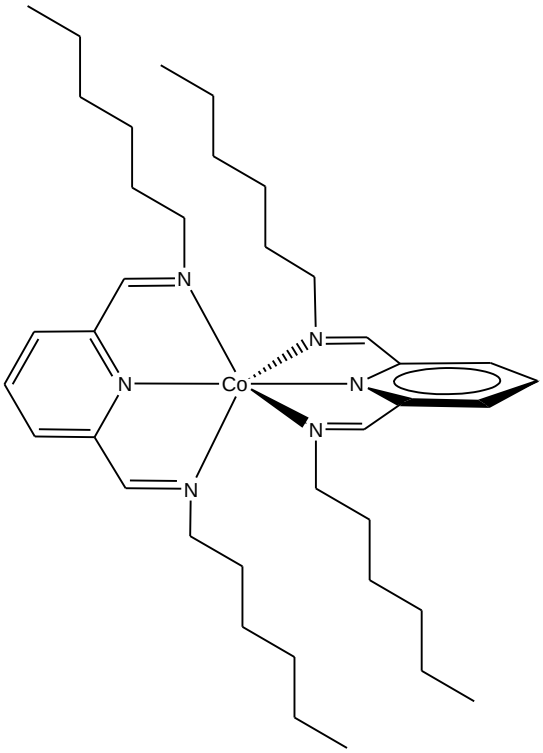

Figure 4.1 The proposed structural formula of $[Co(L^6)_2]^{2+}$

The results of the **elemental analyses** for carbon, hydrogen and nitrogen (**Table 4.1**) are in good agreement with those calculated for the chemical formula, $[Co(L^6)_2](BF_4)_2.½H_2O$ ($C_{38}H_{63}B_2CoF_8N_6O_{½}$, formula weight 844.48 g mol^{-1}).

Table 4.1 Elemental analytical data for **Complex 1**

Element	**(%)**	
	Calculated	**Found**
Carbon	53.99	54.55
Hydrogen	7.46	7.50
Nitrogen	9.95	10.00

Its **ESI-MS** spectrum (**Figure 4.2**) shows peaks at m/z = 612.3 for $[(L^6)_4\text{-}2H]^{2+}.H_2O$ (calculated, 612.9), 346.2 for $[Co(L^6)_2]^{2+}.CH_3OH$ (calculated, 346.7), 330.7 for $[Co(L^6)_2]^{2+}$(calculated, 330.9), and 302.3 for $[(L^6)\text{-}H]^+$ (calculated, 302.3).

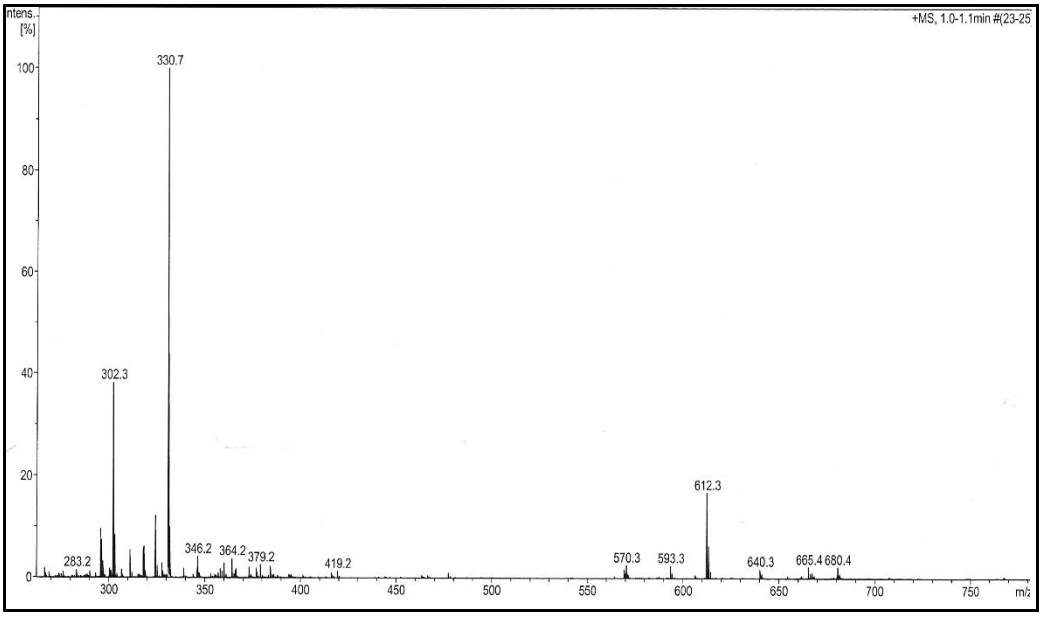

Figure 4.2 The ESI-MS spectrum of **Complex 1**

Its **FTIR** spectrum (**Figure 4.3**) shows two strong peaks at 2928 cm^{-1} and 2859 cm^{-1} for CH_2 asymmetric and symmetric vibrations respectively, a medium peak at 1590 cm^{-1} for aromatic C=C, and two strong overlapping peaks at 1056 cm^{-1} for C-N and BF_4^- ion [2].

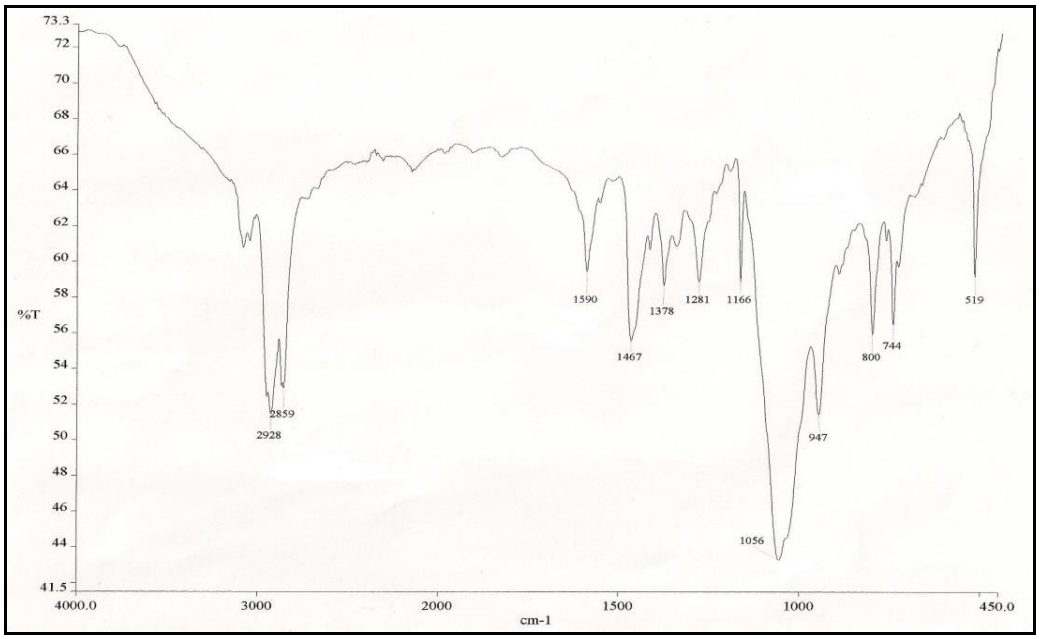

Figure 4.3 FTIR spectrum of **Complex 1**

Its **UV-vis** spectrum in $CHCl_3$ (**Figure 4.4**) shows a broad *d-d* band at 650 nm (ε, 267 M^{-1} cm^{-1}) and three overlapping metal-to-ligand charge transfer (MLCT) [3]

bands at 545 nm (ε, 921 M^{-1} cm^{-1}), 471 nm (ε, 1203 M^{-1} cm^{-1}) and 381 nm (ε, 1798 M^{-1} cm^{-1}). The *d-d* band suggests an octahedral (point group, O_h) and low-spin (LS) mononuclear Co(II) complex, reported in the literature to have maximum absorbance values in the range of 645 – 740 nm [4]. Accordingly, the broad *d-d* band is assigned to overlapping $^2E_g \rightarrow {}^2T_{1g}$ (P) and $^2E_g \rightarrow {}^2T_{2g}$ electronic transitions.

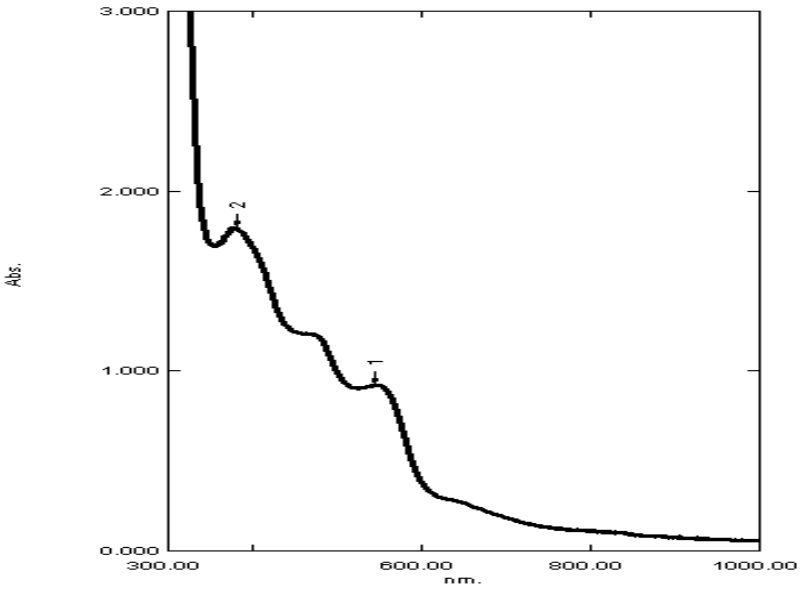

Figure 4.4 UV-vis spectrum of **Complex 1**

(b) Spin-crossover behavior

The $\chi_M^{corr}T$ value for **Complex 1**, calculated from its proposed chemical formula (FW = 844.48 g mol^{-1}), χ_g (3.49 x 10^{-6} cm^3 g^{-1}), χ_M (2.95 x 10^{-3} cm^3 mol^{-1}), χ_{dia} (-441.88 x 10^{-6} cm^3 mol^{-1}) and χ_M^{corr} (3.39 x 10^{-3} cm^3 mol^{-1}), was 0.99 cm^3 K mol^{-1} at 293 K. The theoretical value for a high spin (HS) Co(II) complex (S = $^3/_2$) is 1.876 cm^3 K mol^{-1}, while for a LS Co(II) complex (S = ½) is 0.375 cm^3 K mol^{-1} [5]. From this, it may be inferred that this complex was made up of 41.0% HS and 59.0% LS Co(II) at this temperature [6,7]. Hence, $T_{½}$ for the complex (a temperature at which there was 50% HS and 50% LS cobalt(II)) is postulated to be above 293 K.

Its **temperature-dependence molar absorptivities (ε_{max})** were measured in $CHCl_3$ at 650 nm as this corresponds to the electronic transition involving LS Co(II). The results (**Figure 4.5**) show that on cooling, the ε_{max} values remained almost unchanged at about 265 M^{-1} cm^{-1} from 298 K to 288 K, and then decreased abruption to about 73 M^{-1} cm^{-1} (or the presence of 16.4% LS Co(II)) at 278 K. Upon heating from this temperature, the values increased abruptly back to about 265 M^{-1} cm^{-1} at 288 K, and then remained almost unchanged on further heating to 328 K followed by cooling back to 298 K. It is to note that the highest temperature measurement was governed by the solvent (bpt 334 K) and instrument (minimum 276 K; maximum 343 K). From these results, it may be inferred that **Complex 1** showed a normal and reversible spin crossover (SCO) behavior in solution (HS-to-LS transition on cooling; LS-to-HS transition on heating).

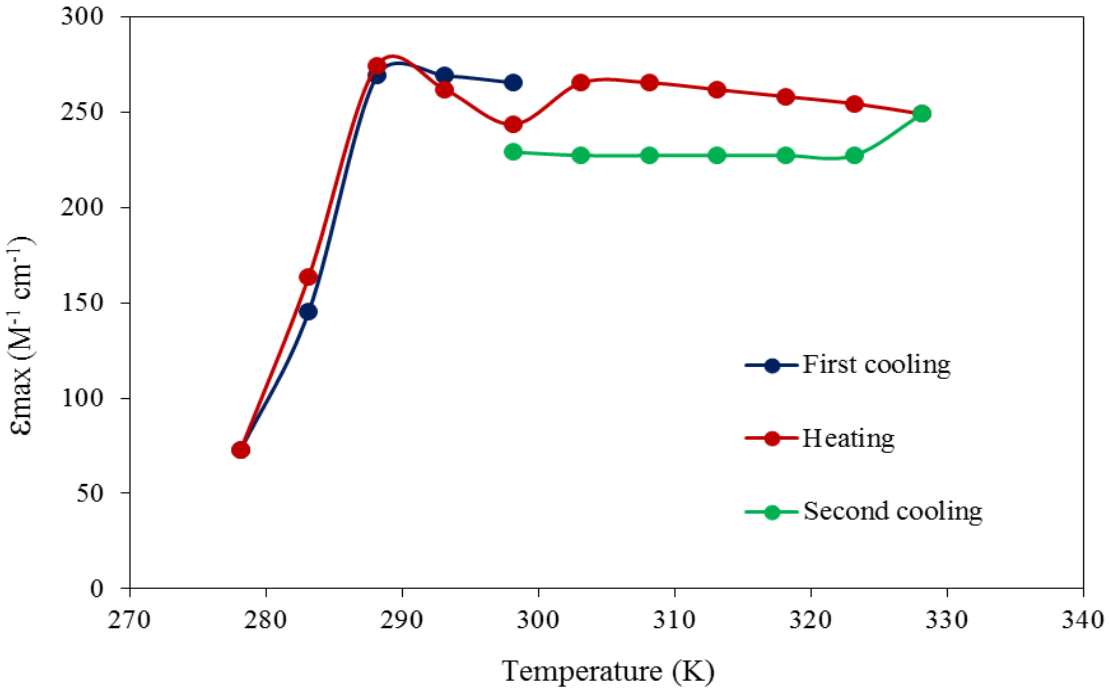

Figure 4.5 Temperature-dependence ε_{max} values for **Complex 1** at 650 nm

(c) Thermal and mesomorphic properties

The thermogravimetric trace (**TGA)** of **Complex 1** (**Figure 4.6**) shows an initial weight loss of 1.6% from 49 °C to 97 °C due to loss of lattice H_2O (expected, 1.1%). It then suffered a weight loss of 15.5% in the temperature range of 97 – 261 °C due to loss of two BF_3 molecules (from the dissociation of two BF_4^- ions; expected, 16.2%), followed by 74.0% from 261 °C to 890 °C due to the decomposition of two L^6 molecules (expected, 71.4%). The amount of residue at temperatures above 876 °C was 8.9%, which was in good agreement with the expected amount of 11.5 % (assuming pure CoF_2). The TGA result further supports its proposed structure. It is probable that the decomposition of BF_4^- ions and L^6 molecules arose from hydrolyses of B-F and C=N bonds, respectively.

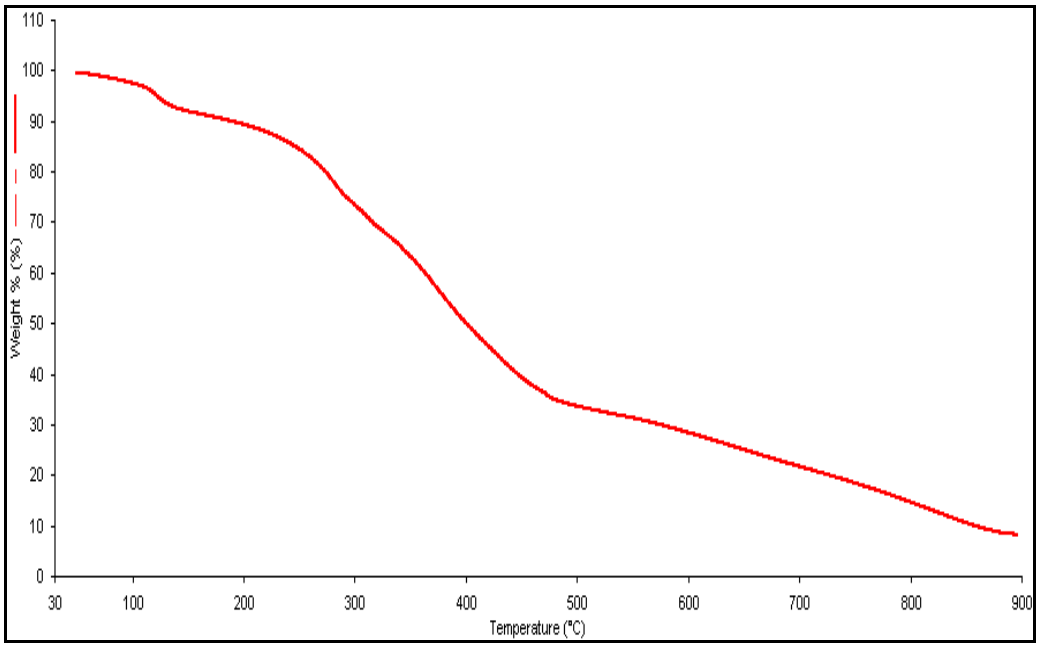

Figure 4.6 TGA of **Complex 1**

Its differential scanning calorimetric scans (**DSC**) (**Figure 4.7**) were recorded for two heating-cooling cycles in the temperature range 25 – 120 °C. The data and assignments were collected in **Table 4.2**. The weak endothermic peaks observed in both heating cycles are probably due to loss of BF_3, as suggested from TGA. The absence of

any peaks during the first and second cooling cycles indicates no bond forming processes.

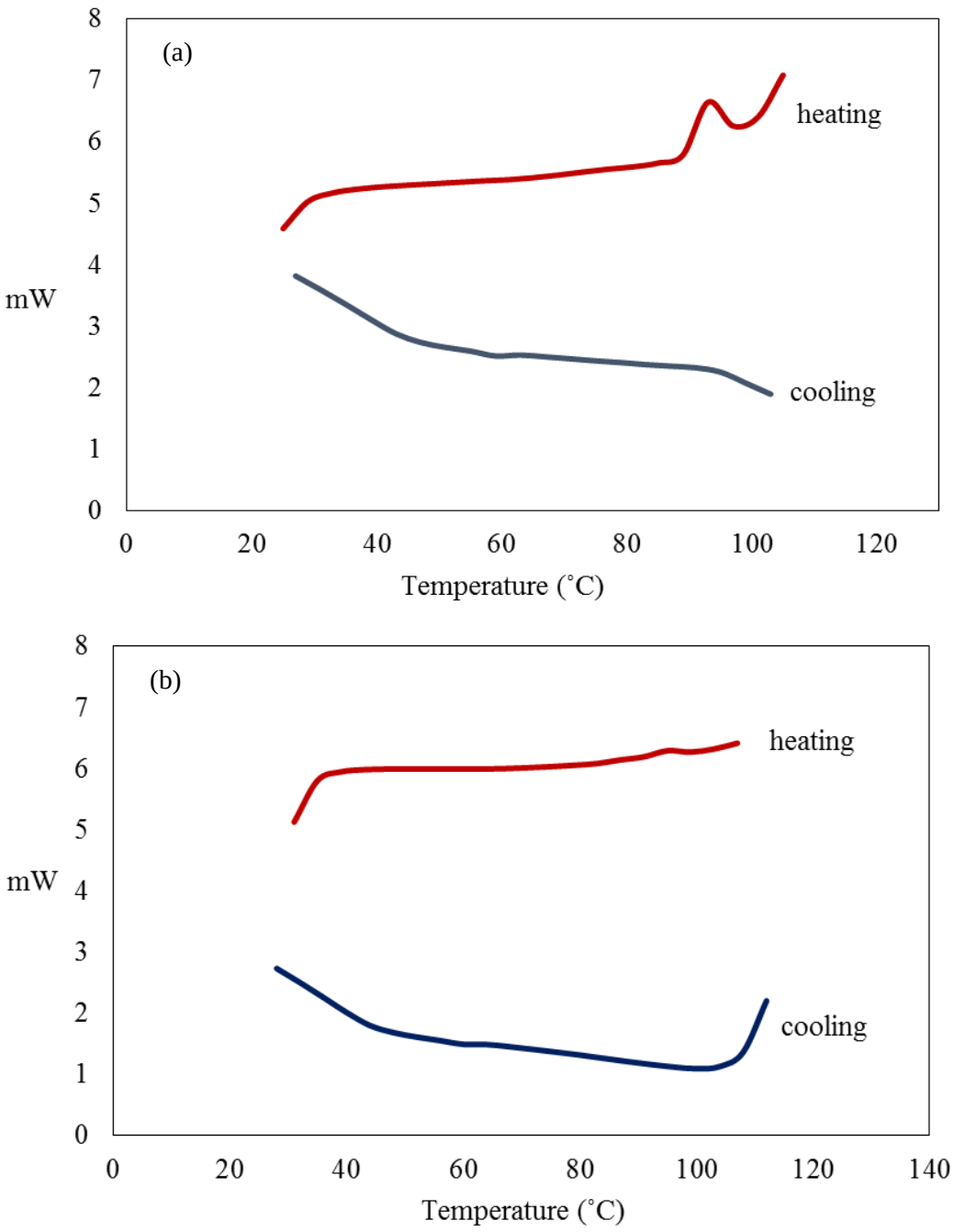

Figure 4.7 DSC of **Complex 1**: (a) first cycle; (b) second cycle. Endothermic peak up

Table 4.2 DSC data for **Complex 1**

Cycle		Temperature (˚C)	ΔH (kJ mol^{-1})	Assignment
1	Heating	93.5	+1.48	Loss of BF_3
	Cooling	-	-	-
2	Heating	92.8	+0.36	Further loss of BF_3
	Cooling	-	-	-

Viewed under a polarizing optical microscope (**POM**), **Complex 1** was observed to start melting at about 60 °C and to clear at 75 °C, though both transitions were not detected by DSC. On cooling from the isotropic liquid, it developed rod-like textures at 50 °C, which corresponded to the formation of a crystalline phase (**Figure 4.8**). Hence, it may be concluded that **Complex 1** did not have mesomorphic properties. The result is consistent with DSC.

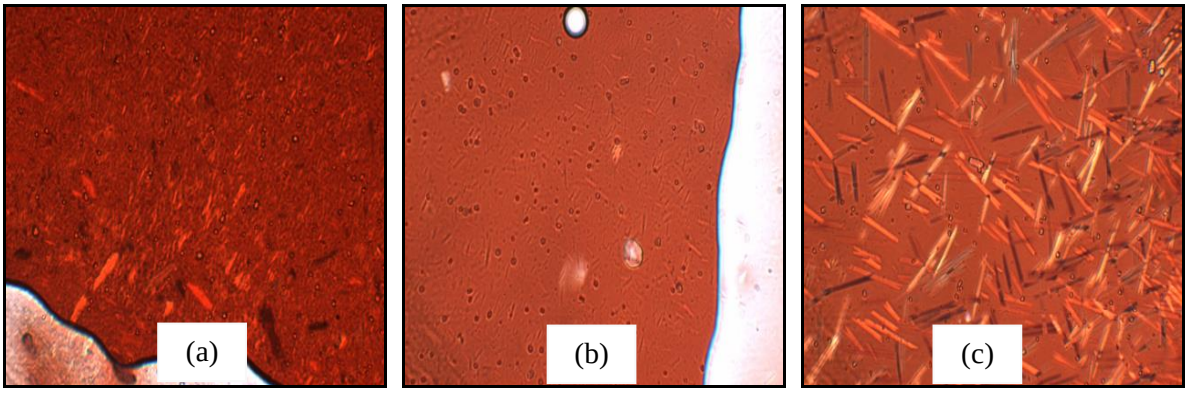

Figure 4.8 Photomicrographs of **Complex 1** on: (a) heating at 70.0 °C; (b) heating at 79.0°C; and (c) cooling at 50.0 °C

4.2.2 $[Co(L^8)](BF_4)_2.H_2O$

2,6-Pyridinedicarboxaldehyde, 1-aminooctane and $Co(BF_4)_2.6H_2O$ reacted in methanol to form a red-brick powder (**Complex 2**) in good yield (82.9%). The powder was readily soluble in the same solvents as **Complex 1**. It is noted that the powder changed to a gummy solid within a few minutes at room temperature. This was likely due to

rapid absorption of atmospheric moisture since the powder form was again recovered after the sample was heated in a warm oven.

(a) Deduction of structural formula

Based on the same instrumental analyses as previously discussed, it is proposed that the structure of **Complex 2** was similar to that of **Complex 1** (**Figure 4.1**).

The results of **elemental analyses** for carbon, hydrogen and nitrogen (**Table 4.3**) are in excellent agreement with those calculated for the chemical formula $[Co(L^8)_2](BF_4)_2.H_2O$ ($C_{46}H_{80}B_2CoF_8N_6O$; formula weight 965.71 g mol^{-1}).

Table 4.3 Elemental analytical data for **Complex 2**

Element	**(%)**	
	Calculated	**Found**
Carbon	57.21	57.05
Hydrogen	8.35	8.30
Nitrogen	8.70	8.80

Its **ESI-MS** spectrum (**Figure 4.9**) shows peaks at m/z = 860.6 for $[Co(L^8)_2(BF_4)]^+$ ion (calculated, 860.6), 792.6 for $[Co(L^8)_2F]^+$ (calculated, 792.6), 386.8 for $[Co(L^8)_2]^{2+}$ ion (calculated, 386.8), and 130.2 for $[CH_3(CH_2)_7N\text{-}H]^+$ ion (calculated, 128.1).

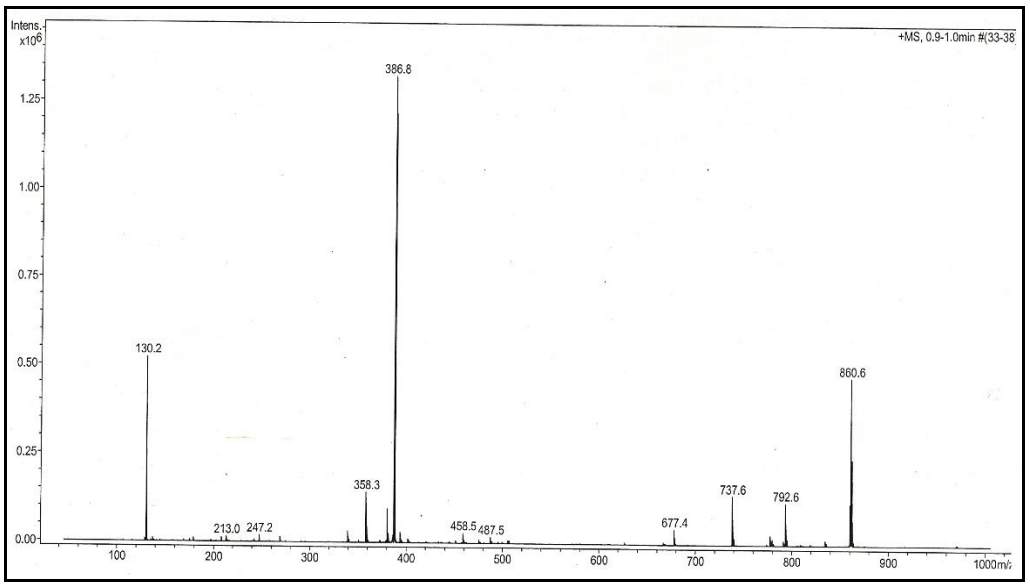

Figure 4.9 ESI-MS spectrum of **Complex 2**

Its **FTIR** spectrum (**Figure 4.10**) shows a broad peak at 3277 cm^{-1} for H_2O, and peaks at 2925 cm^{-1}, 2856 cm^{-1}, 1592 cm^{-1} and 1045 cm^{-1}. These peaks may be similarly assigned as for **Complex 1**.

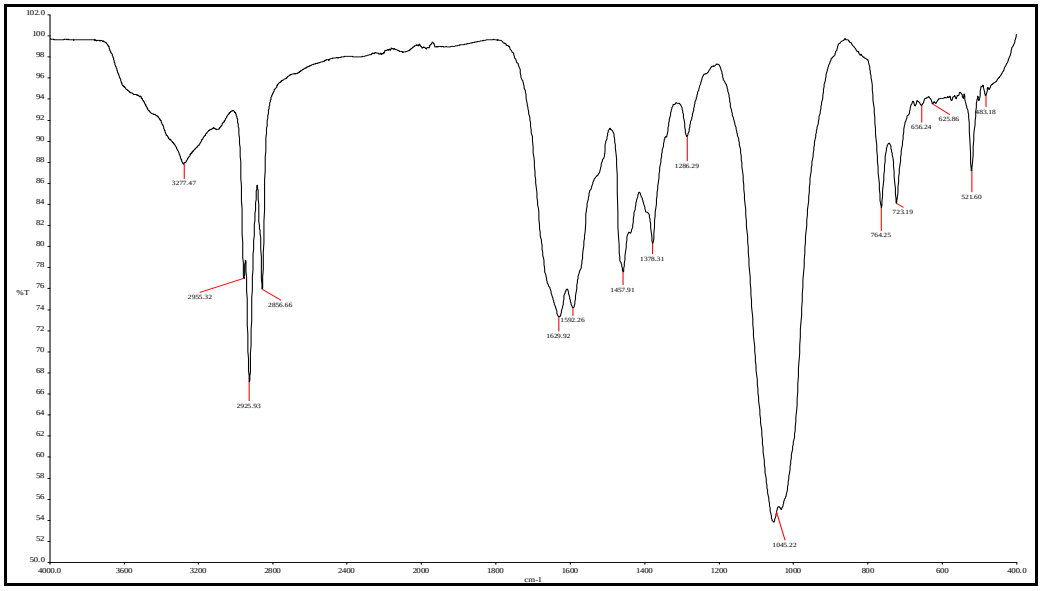

Figure 4.10 FTIR spectrum of **Complex 2**

Its **UV-visible** spectrum in $CHCl_3$ (**Figure 4.11**) shows broad *d-d* bands at 684 nm (ε, 273 M^{-1} cm^{-1}) and 507 nm (ε, 759 M^{-1} cm^{-1}), and a broad shoulder at 402 nm (ε, 2088 M^{-1} cm^{-1}). These electronic transitions may be similarly assigned as for **Complex 1**.

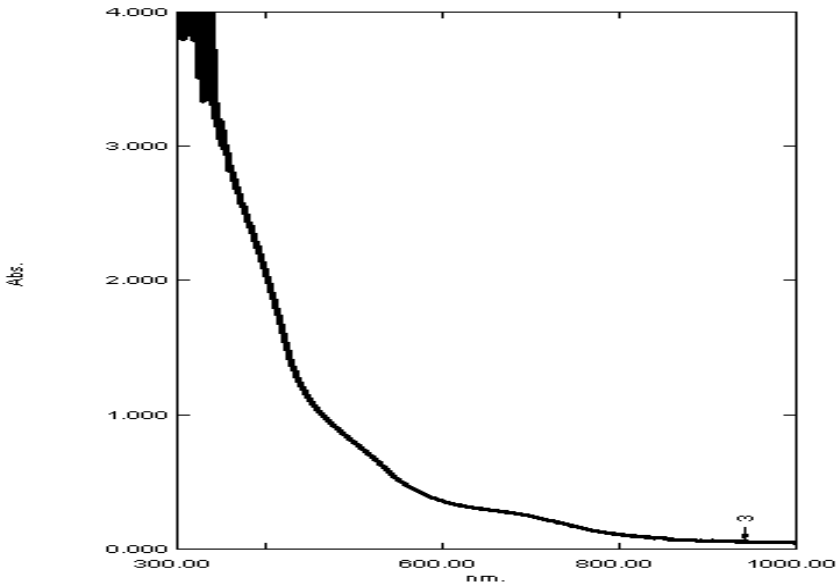

Figure 4.11 UV-visible spectrum of **Complex 2**

(b) Spin-crossover behaviour

The value of $\chi_M^{corr}T$ for **Complex 2**, calculated from its proposed chemical formula (FW = 965.71 g mol^{-1}), χ_g (4.34 x 10^{-6} cm^3 g^{-1}), χ_M (4.19 x 10^{-3} cm^3 mol^{-1}), χ_{dia} (-543.26 x 10^{-6} cm^3 mol^{-1}) and χ_M^{corr} (4.73 x 10^{-3} cm^3 mol^{-1}), was 1.39 cm^3 mol^{-1} K at 293 K. Accordingly, this complex was made up of 67.6% HS and 32.4% LS. Co(II) at this temperature. Hence, it has a higher percentage of HS Co(II) compared to **Complex 1**. The result is consistent with a stronger fastening effect of the longer alkyl chain [1], which led to weaker Co(II)-L^n bonds, hence HS Co(II).

Its **temperature-dependence** ε_{max} values were similarly measured as for **Complex 1**. The results (**Figure 4.12**) show that on cooling from 298 K to 288 K, the ε_{max} values remained almost unchanged at about 180 M^{-1} cm^{-1}, and then decreased abruption to about 49 M^{-1} cm^{-1} (or the presence of about 5.8% LS Co(II)) at 278 K. Upon heating from 278 K, the values increased abruptly, showing two maximum values of 212 M^{-1} cm^{-1} and 293 M^{-1} cm^{-1} at 283 K and 298 K respectively. The values then dropped to 171 M^{-1} cm^{-1} and remained almost unchanged on further heating to 328 K, and then cooling back to 298 K. From these, it may be inferred that **Complex 2** also

showed a normal and reversible spin crossover (SCO) behavior in solution, but the concentration of LS Co(II) was lower (32.4%) compared to that of **Complex 1** (59.0%) at the same temperature. This is consistent with the stronger fastening effect of the longer alkyl chain in **Complex 2**.

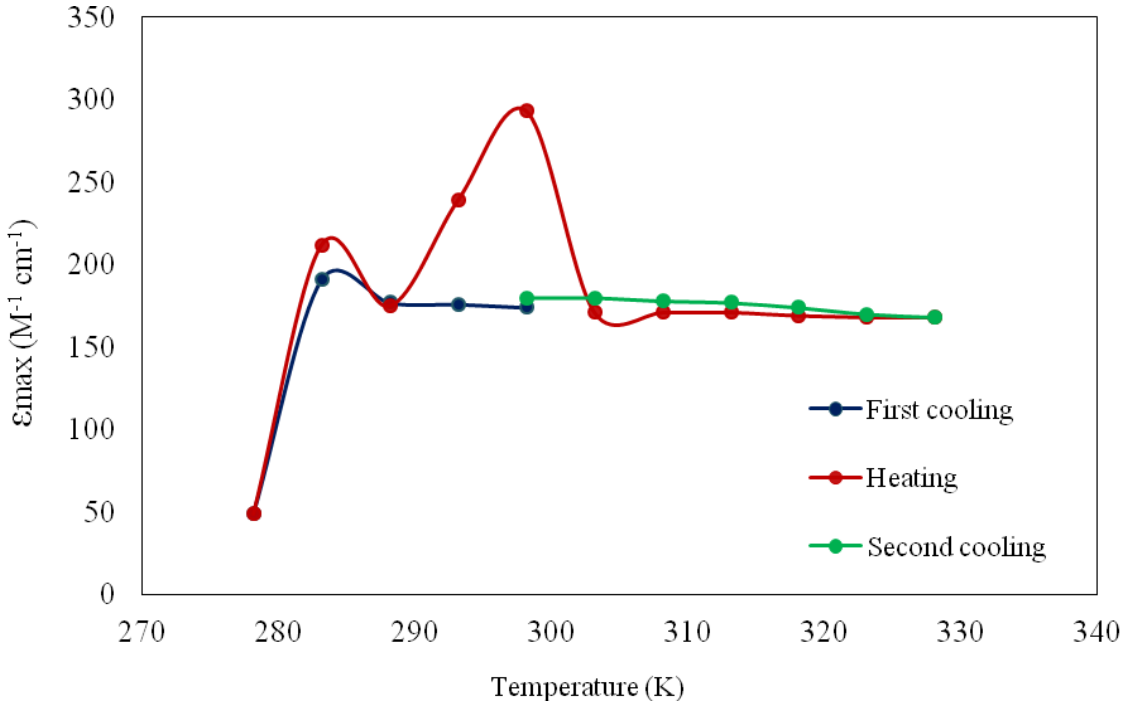

Figure 4.12 Temperature-dependence ε_{max} values for **Complex 2** at 684 nm

(c) Thermal and mesomorphic properties

The **TGA** trace of **Complex 2** (**Figure 4.13**) is similar to **Complex 1**. It suffered weight losses of 2.9% from 67 °C to 118 °C due to the evaporation of lattice H_2O (expected, 1.9%), and 87.0% (expected, 88.1%) from 118 °C to 812 °C due to loss of two BF_3 molecules and decomposition of two L^8 ligands. The amount of residue at temperatures above 812 °C was 10.1%, which is in good agreement with the expected amount of 10.0% (assuming CoF_2). It is noted that the mass loss from **Complex 2** occurred at a slightly higher temperature (118 °C) compared to **Complex 1** (97 °C). This may be due to the longer alkyl chain in the former complex, which acted as a 'trap' for BF_3 molecules from escaping.

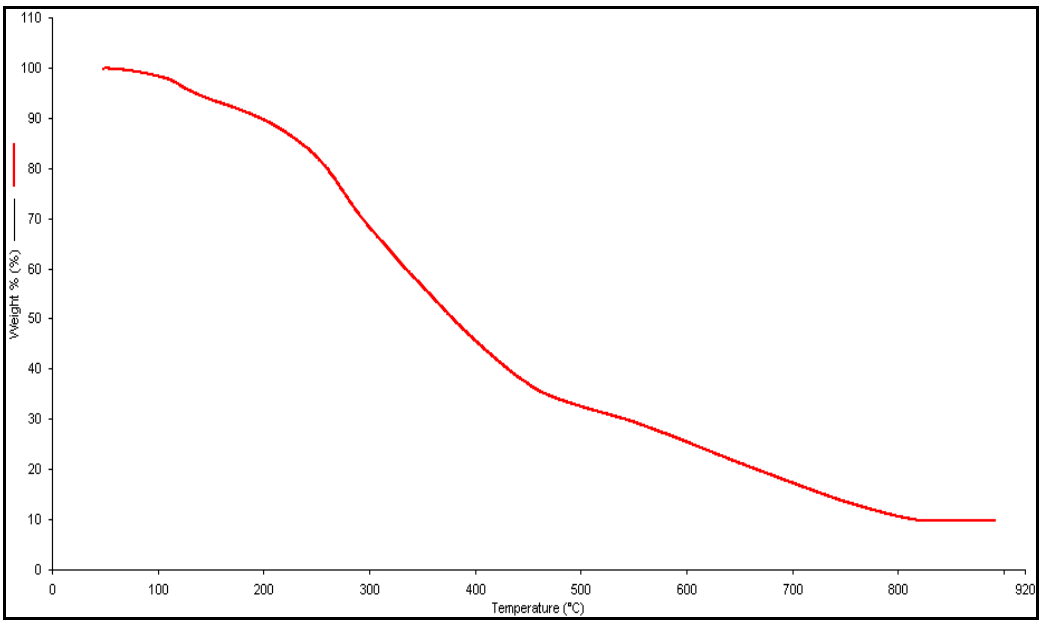

Figure 4.13 TGA of **Complex 2**

Viewed under **POM, Complex 2** was observed to start melting at about 80 °C and to clear to an isotropic liquid at 150 °C. However, on cooling from the isotropic liquid phase, there were no optical textures formed. Hence, as for **Complex 1**, this complex also did not exhibit any mesomorphic properties.

4.2.3 $[Co(L^{10})](BF_4)_2.½H_2O$

2,6-Pyridinedicarboxaldehyde, 1-aminodecane and $Co(BF_4)_2.6H_2O$ reacted in methanol to forma red-brick powder (**Complex 3**) in good yield (90.7%). The powder was readily soluble in the same solvents as **Complexes 1** and **2**. Also similar observed for **Complex 2**, the powder changed to a gummy solid within a few minutes at room temperature.

(a) Deduction of structural formula

Based on the same instrumental analyses, it is proposed that the structure of **Complex 3** was similar to those of **Complex 1** (**Figure 4.1**).

The results of **elemental analyses** for carbon, hydrogen and nitrogen (**Table 4.4**) are in excellent agreement with those calculated for chemical formula $[Co(L^{10})_2](BF_4)_2.½H_2O$ ($C_{54}H_{95}B_2CoF_8N_6O_{½;}$ formula weight 1068.91 g mol^{-1}).

Table 4.4 Elemental analytical data for **Complex 3**

Element	(%)	
	Calculated	**Found**
Carbon	60.67	60.85
Hydrogen	8.96	8.85
Nitrogen	7.86	7.70

Its **ESI-MS** spectrum (**Figure 4.14**) shows peaks at m/z 972.7 for $[Co(L^{10})_2(BF_4)]^+$ ion (calculated, 972.7), 904.7 for $[Co(L^{10})_2F]^+$ ion (calculated, 904.7), and 443.8 for $[Co(L^{10})_2]^{2+}$ ion (calculated, 442.8).

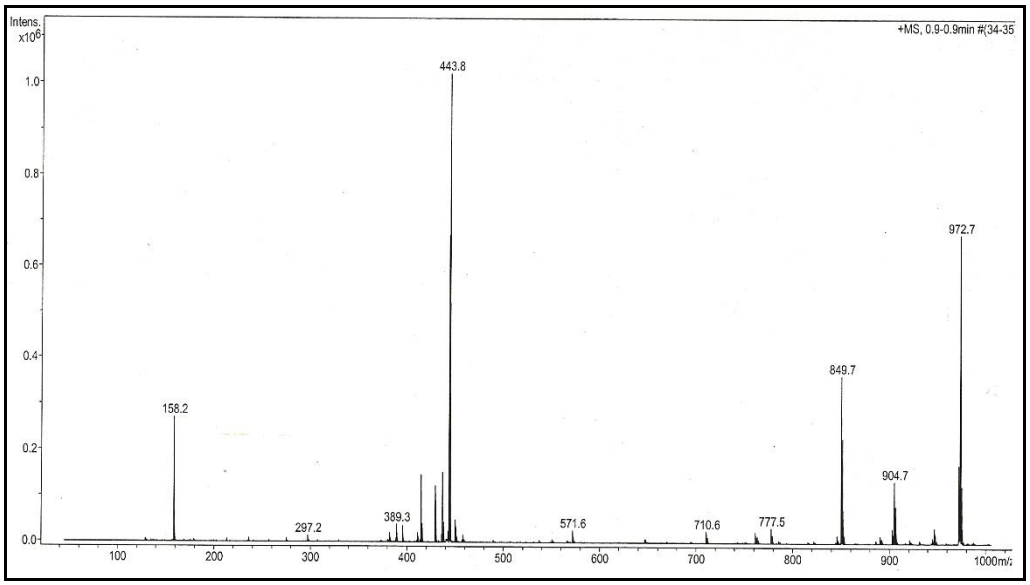

Figure 4.14 ESI-MS spectrum of **Complex 3**

Its **FTIR** spectrum (**Figure 4.15**) shows peaks at 3268 cm^{-1}, 2923 cm^{-1}, 2854 cm^{-1}, 1591 cm^{-1} and 1049 cm^{-1}. These peaks may be similarly assigned as for **Complexes 1** and **2**.

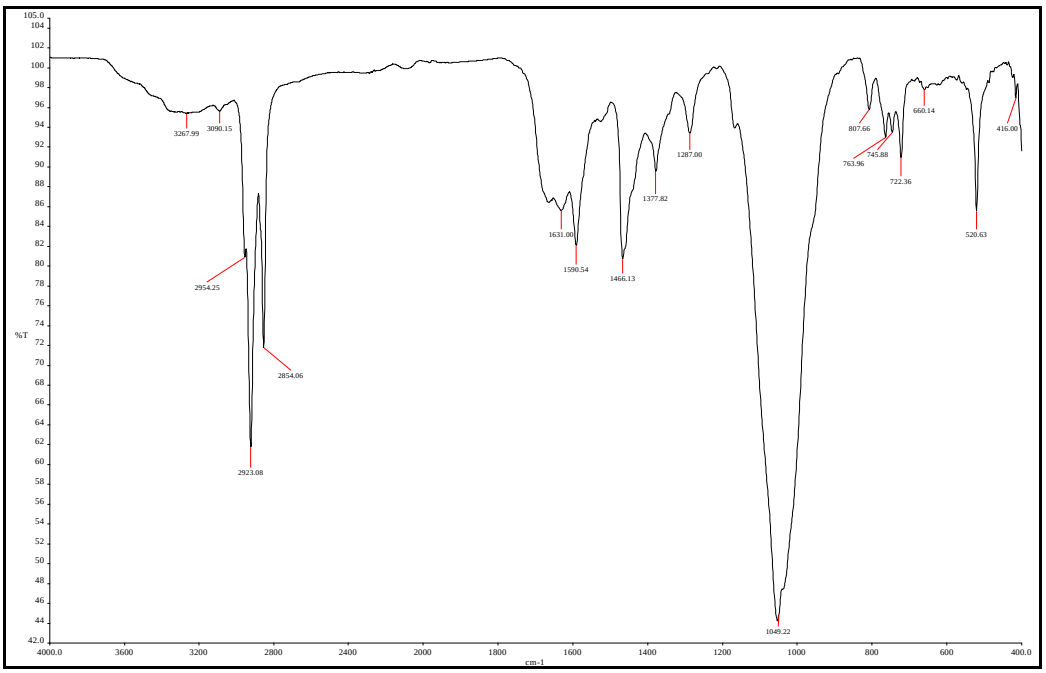

Figure 4.15 FTIR spectrum of **Complex 3**

Its **UV-visible** spectrum in $CHCl_3$ (**Figure 4.16**) shows broad overlapping bands at 664 nm (ε, 248 M^{-1} cm^{-1}), 555 nm (ε, 818 M^{-1} cm^{-1}), and 480 nm (ε, 2088 M^{-1} cm^{-1}). These electronic transitions may be similarly assigned as for **Complexes 1** and **2**.

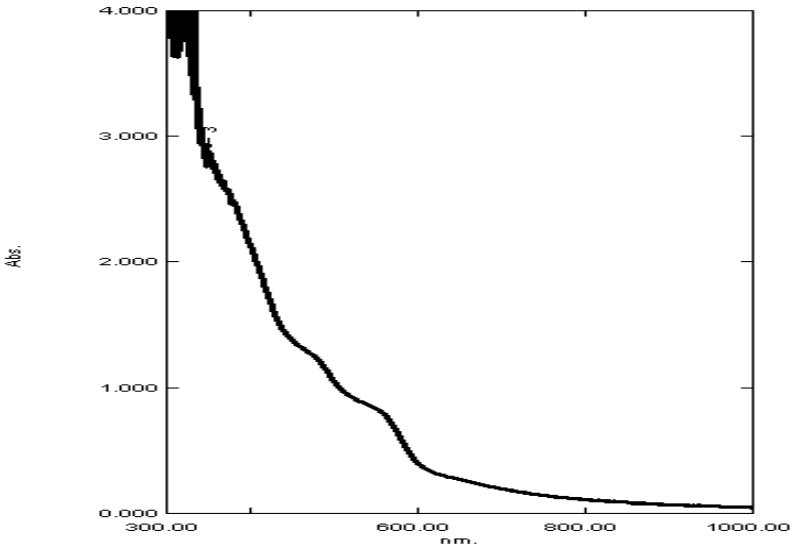

Figure 4.16 UV-visible spectrum of **Complex 3**

(b) Spin-crossover behavior

The $\chi_M^{corr}T$ value for **Complex 3**, similarly calculated as previously done from its proposed chemical formula (FW = 1068.9 g mol^{-1}), χ_g (2.82 x 10^{-6} cm^3 g^{-1}), χ_M (3.01 x 10^{-3} cm^3 mol^{-1}), χ_{dia} (-638.14 x 10^{-6} cm^3 mol^{-1}) and χ_M^{corr} (3.65 x 10^{-3} cm^3 mol^{-1}), was 1.07 cm^3 mol^{-1} K at 293 K. Thus, this complex was made up of 46.3% HS and 53.7% LS Co(II) at this temperature. From this, it may be inferred that the fastening effect of the alkyl chains was similar in **Complexes 1** (*n* = 6) and **3** (*n* = 10), and less significant when compared to **Complex 2** (*n* = 8).

Its **temperature-dependence** ε_{max} values were similarly recorded as for previous complexes. The results (**Figure 4.17**) show the values remained almost unchanged at about 250 M^{-1} cm^{-1} on cooling-heating-cooling steps. This means that the amount of HS and LS Co(II) in this complex remained unaffected in the temperature range of 278 – 328 K.

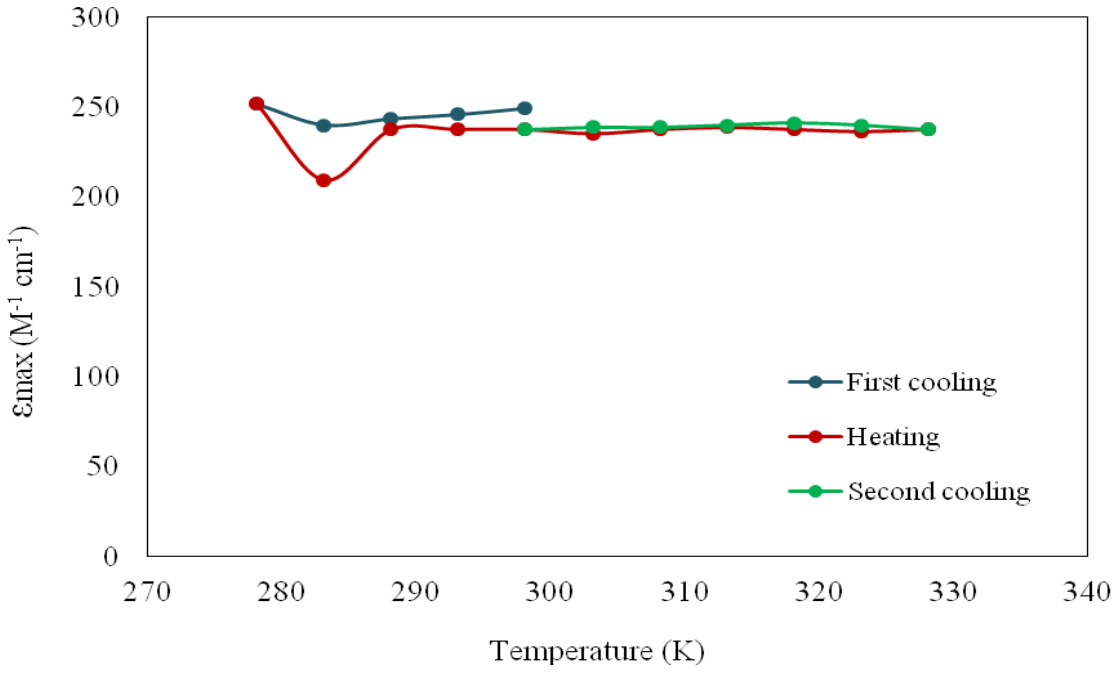

Figure 4.17 Temperature-dependence of ε_{max} values for **Complex 3** at 664 nm

(c) Thermal and mesomorphic properties

The **TGA** trace of **Complex 3** (**Figure 4.18**) shows similar thermal behavior as **Complexes 1** and **2**. The complex suffered weight losses of 1.0% at 166 °C to 195 °C due to the evaporation of lattice H_2O (expected, 0.8%), and 84.4% in the temperature range of 209 – 889 °C due to loss of two BF_3 molecules and two L^{10} ligands (expected, 90.1%). The amount of residue at temperatures above 889 °C cannot be ascertained as there was no plateau above this temperature. Hence, the mass loss of this complex occurred at a significantly higher temperature (209 °C) compared to **Complexes 2** (118 °C) and **1** (97 °C), consistent with the increase in the alkyl chain length.

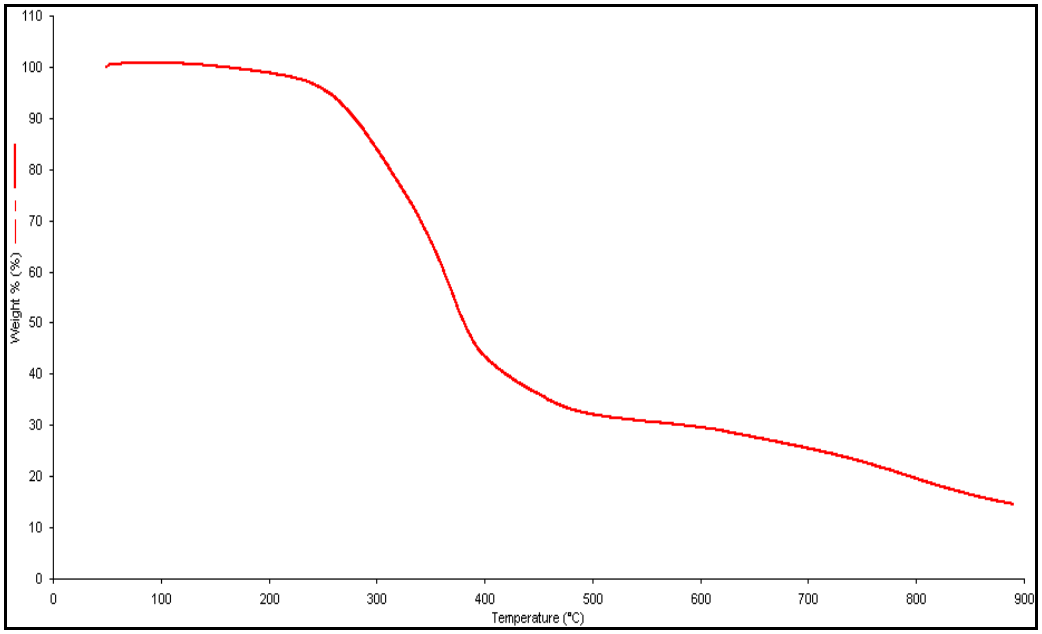

Figure 4.18 TGA of **Complex 3**

Viewed under **POM**, **Complex 3** was observed to start melting at about 70 °C and to clear to an isotropic liquid at 99 °C. However, there were no optical textures when the isotropic liquid was cooled. Hence, as similarly observed for **Complexes 1** and **2**, this complex was also not mesomorphic.

4.2.4 $[Co(L^{12})_2](BF_4)_2$

2,6-pyridinedicarboxaldehyde, 1-aminododecane and $Co(BF_4)_2.6H_2O$ reacted in methanol to form a red-brick powder (**Complex 4**) in good yield (76.2%).The powder was readily soluble in the same solvents as **Complexes 1-3**.

(a) Deduction of structural formula

Based on the same instrumental analyses as previously discussed, it is proposed that the structure of **Complex 4** was similar to that of **Complexes 1-3** (**Figure 4.1**).

The results of **elemental analyses** for carbon, hydrogen and nitrogen (**Table 4.5**) are in excellent agreement with those calculated for chemical formula $[Co(L^{12})_2](BF_4)_2$ ($C_{62}H_{110}B_2CoF_8N_6$; formula weight 856.80 g mol^{-1}).

Table 4.5 Elemental analytical data for **Complex 4**

Element	(%)	
	Calculated	**Found**
Carbon	63.53	63.25
Hydrogen	9.46	9.45
Nitrogen	7.17	7.00

Its **ESI-MS** spectrum (**Figure 4.19**) shows a peak at m/z 498.9 for $[Co(L^{12})_2]^{2+}$ ion (calculated, 498.9).

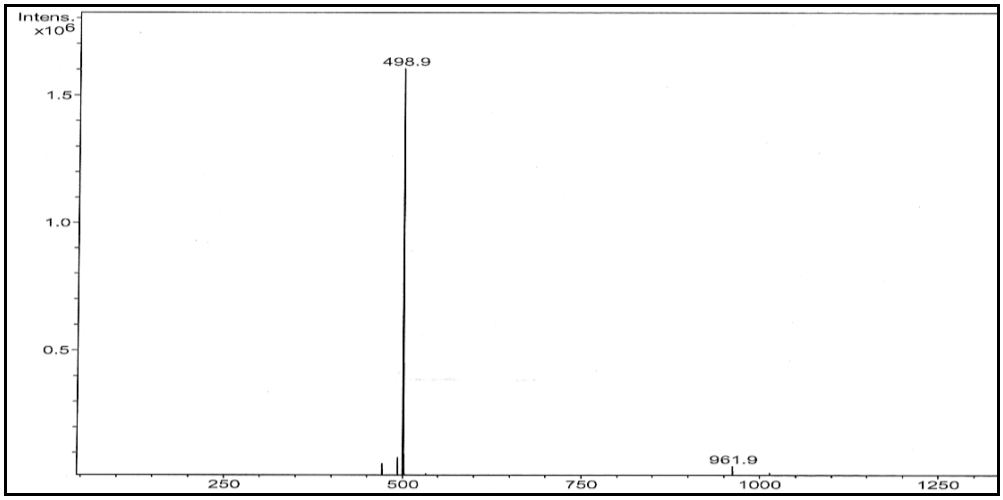

Figure 4.19 ESI-MS spectrum of **Complex 4**

Its **FTIR** spectrum (**Figure 4.20**) shows peaks at 2918 cm^{-1}, 2852 cm^{-1}, 1592 $cm^{-1}$and 1057 cm^{-1}. These peaks may be similarly assigned as for **Complexes 1-3.**

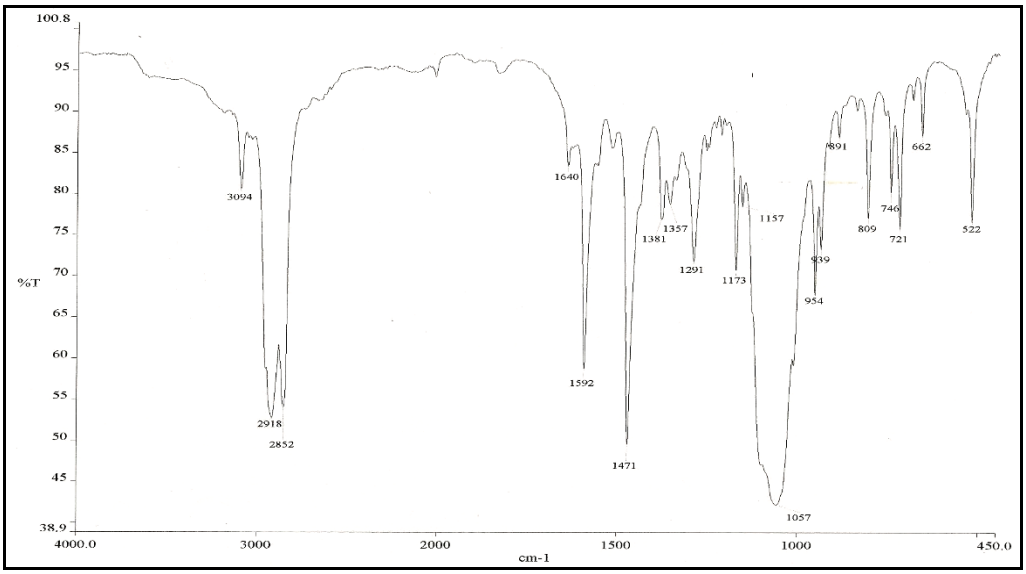

Figure 4.20 FTIR spectrum of **Complex 4**

Its **UV-visible** spectrum in $CHCl_3$ (**Figure 4.21**) shows bands at 822 nm (ε, 100 M^{-1} cm^{-1}), 650 nm (ε, 229 M^{-1} cm^{-1}), 549 nm (ε, 1295 M^{-1} cm^{-1}), 472 nm (ε, 1755 M^{-1} cm^{-1}), and 391 nm (ε, 2346 M^{-1} cm^{-1}). The lowest energy band is assigned to *d-d* transition for HS Co(II) ($^4T_{1g}$ → $^4T_{2g}$), while the higher energy bands are similarly assigned as for **Complexes 1-3**.

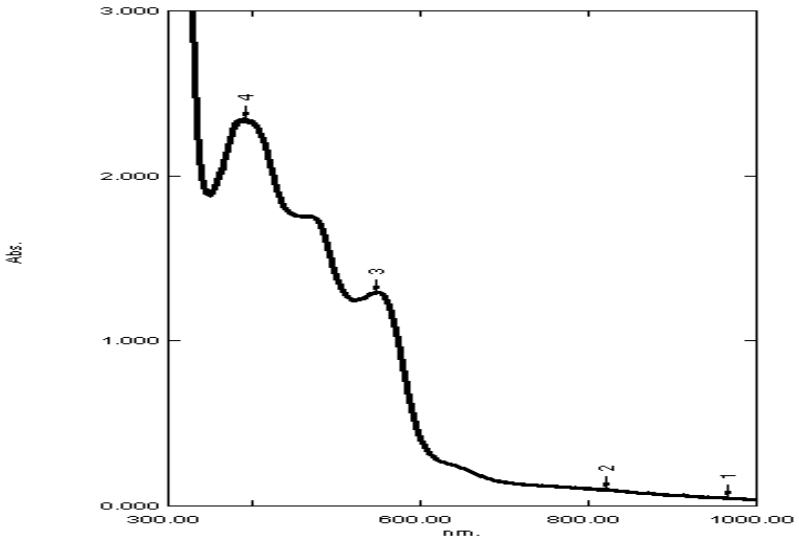

Figure 4.21 UV-visible spectrum of **Complex 4**

On recrystallisation in methanol with slow diffusion of diethyl ether, the complex formed needle-like dark maroon crystals. Its structure was then confirmed by single crystal **X-ray crystallography** (**Figure 4.22**). The crystal structure shows that the complex crystallized in the monoclinic system, and that the Co(II) ion in $[Co(L^{12})_2]^{2+}$ was in an octahedral geometry, while two BF_4^- ions were not coordinated. The packing pattern is shown on **Figure 4.23**.

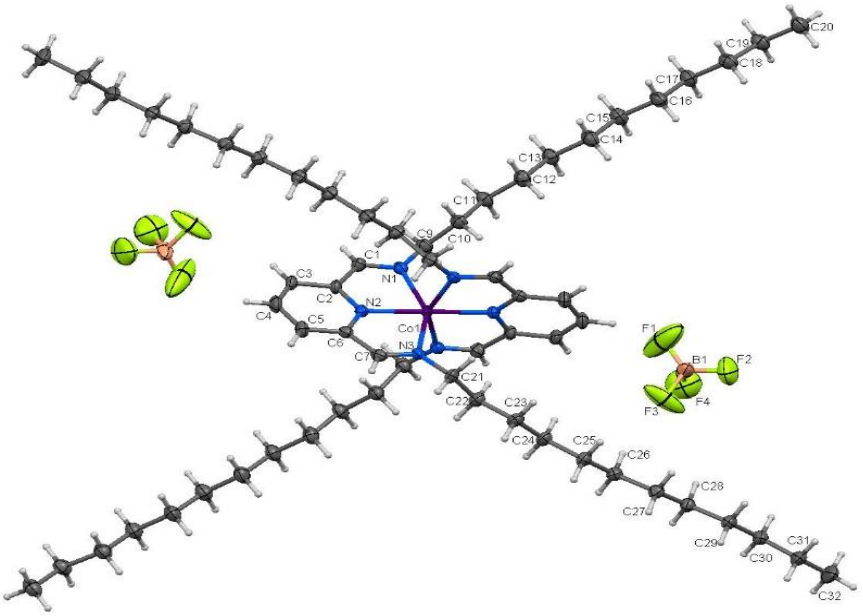

Figure 4.22 Molecular structure of **Complex 4,** showing displacement ellipsoids

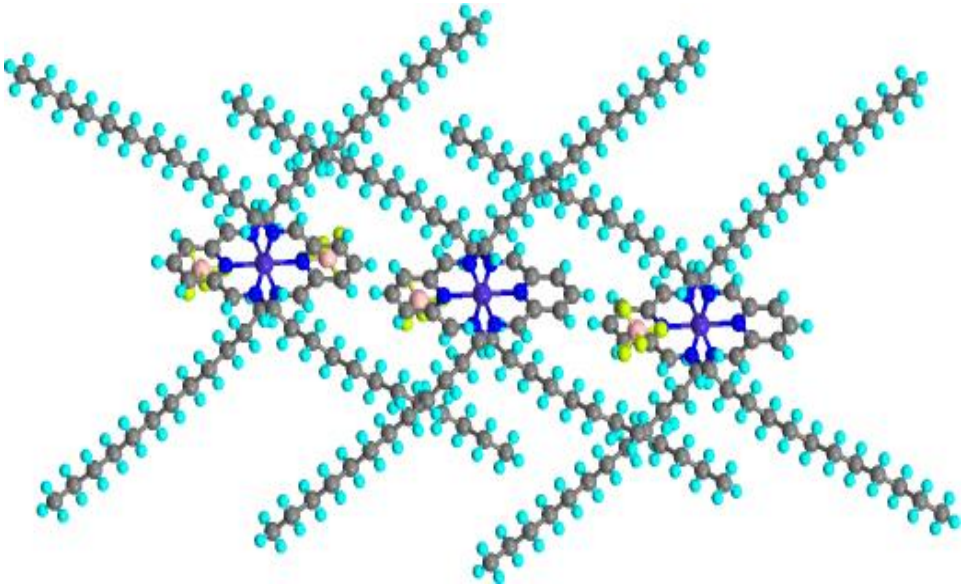

Figure 4.23 The packing pattern of **Complex 4**, viewed along the crystallographic *b*-direction

The crystal data and structure refinement details for **Complex 4** are shown in **Table 4.6**, while the selected bond lengths are shown in **Table 4.7**.

Table 4.6 Crystallography and refinement details of **Complex 4**

Empirical formula	$C_{62}H_{110}B_2CoF_8N_6$
Formula weight	1172.11
Temperature	293 K
Wavelength	0.71073 Å
Crystal system, space group	Monoclinic, P2/n
Unit cell dimension	a = 17.1066(3) Å α = 90˚ b = 9.3515(19) Å β = 107.6370(3)˚ c = 21.8195(2) Å γ = 90˚
Volume	3326.39 (12) A^3
Z, Calculated density	2, 1.868 g/cm^3
Absorption coefficient	0.321 mm^{-1}
F(000)	1266
θ range for data collection	1.3, 25.0˚
Limiting indices (±*h*, ±*k*, ±*l*)	-20/20, -11/11, -25/25
Data / restrains / parameters	5851 / 0 / 357
Goodness-of-fit on F^2	2.24
Final R indices [I > 2σ(I)]	R1 = 0.0975, wR2 = 0.2831

Table 4.7 Selected bond lengths (Å) for **Complex4**

Co1 – N1	2.216(4)	N1– C1	1.283(5)
Co1 – N2	2.038(4)	N2 – C2	1.343(6)
Co1 – N3	2.218(4)	N3 – C7	1.262(5)

(b) Spin-crossover behavior

The $\chi_M^{corr}T$ value for **Complex 4,** similarly calculated as previously done from its proposed chemical formula (**FW** = 1172.12 g mol^{-1}), χ_g (5.07 x 10^{-6} cm^3 g^{-1}), χ_M (5.94 x 10^{-3} cm^3 mol^{-1}), χ_{dia} (-726.52 x 10^{-6} cm^3 mol^{-1}), and

χ_M^{corr} (6.67 x 10^{-3} cm^3 mol^{-1}), is 1.95 cm^3 mol^{-1} K. Thus, this complex was made up of 100% HS Co(II) at this temperature. This may be due to absence of lattice H_2O and effective fastening effect of the longer alkyl chains.

The variable-temperature magnetic susceptibilities for the powder were measured for two cooling and heating cycles using the **SQUID** magnetometer. For the first cycle, the sample was first cooled from 300 K to 4 K, and then heated from 4 K to 372 K. For the second cycle, the sample was cooled to 4 K, and then heated to 385 K. The $\chi_M T$ vs. T plots are shown in **Figure 4.24**.

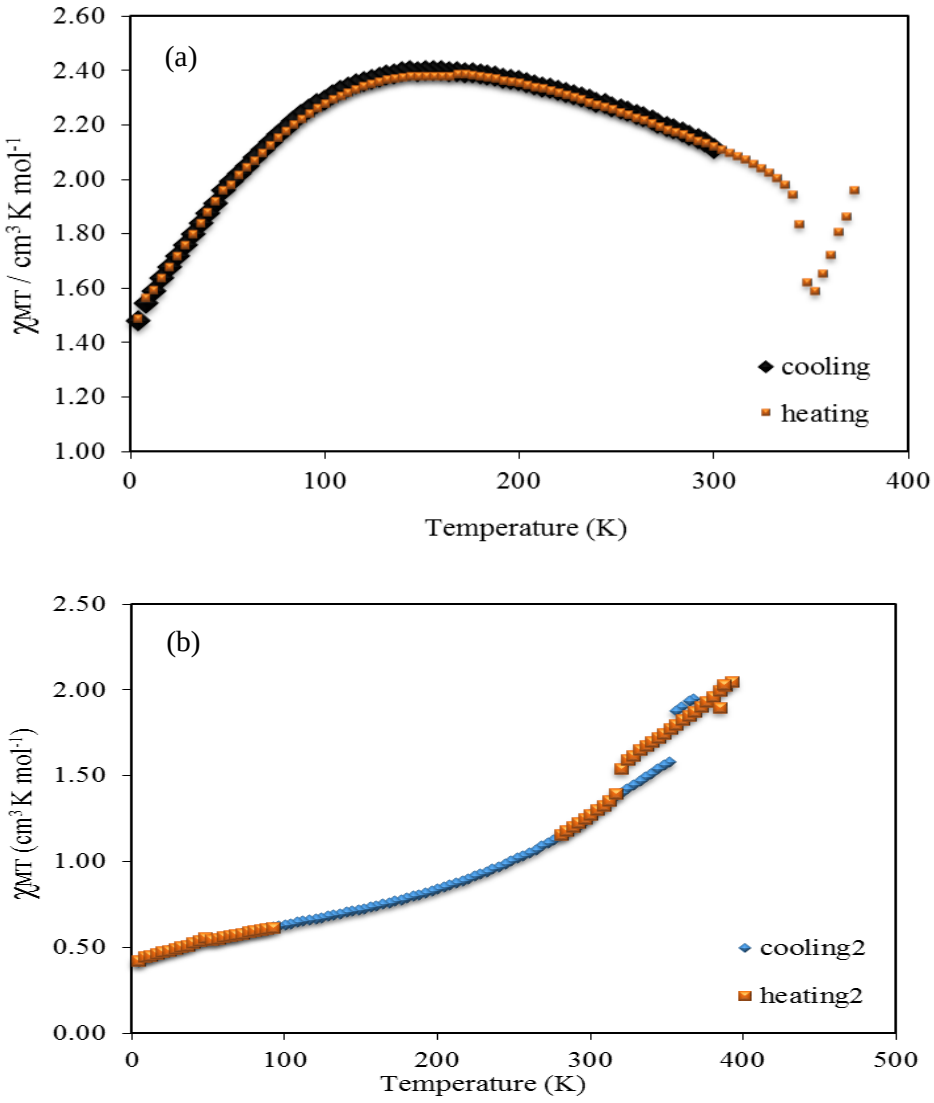

Figure 4.24 Plots of $\chi_M T$ vs. T for **Complex 4**: (a) first cycle (372 K to 4 K); and (b) second cycle (385 K to 4 K)

During the first cycle, the $\chi_M T$ values increased gradually from 2.10 cm^3 K mol^{-1} at 300 K to a maximum value of 2.40 cm^3 K mol^{-1} at 144 K, and then decreased gradually to 1.48 cm^3 K mol^{-1} at 4 K. When the sample was reheated, the $\chi_M T$ values increased gradually to 2.38 cm^3 K mol^{-1} at 168 K, then decreased to 1.59 cm^3 K mol^{-1} at 352 K, and finally increased to 1.96 cm^3 K mol^{-1} at 372 K. No thermal hysteresis was observed from this cycle.

However, on the second cycle different trend was observed. Upon cooling, the $\chi_M T$ values decreased gradually from 1.94 cm^3 K mol^{-1} at 367 K to 1.88 cm^3 K mol^{-1} at 356 K, and then it decreased abruptly to 1.58 cm^3 K mol^{-1}at 352 K. On further cooling, the $\chi_M T$ values decreased gradually to 0.42 cm^3 K mol^{-1} at 4 K. When the sample was reheated, the $\chi_M T$ values increased gradually to 1.38 cm^3 K mol^{-1} at 316 K following the same trend as previous cooling, then increased abruptly to 1.54 cm^3 K mol^{-1} at 320 K. On further heating, the values increased gradually to 2.04 cm^3 K mol^{-1} at 392 K. Hence, a wide hysteresis loop (ΔT = 36 K) observed during the second cycle was due to the occurrence of spin crossover ($T_{½}\downarrow$= 355 K and $T_{½}\uparrow$ = 319 K).

Its **temperature-dependence ε_{max}** values were similarly measured as for previous complexes, but at 820 nm (which relates to HS Co(II)). The results (**Figure 4.25**) were expectedly different compared to **Complexes 1-3**. During initial cooling, the ε_{max} values remained almost unchanged at about 140 M^{-1} cm^{-1} from 298 to 283 K, and then increased abruptly to 300 M^{-1} cm^{-1} at 278 K. Upon heating, the ε_{max} value decreased abruptly to about 50 M^{-1} cm^{-1} at 283 K, and then increased back to about 140 M^{-1} cm^{-1} and remained unchanged on further heating to 330 K and cooling back to room temperature. The unexpected behavior at low temperature may not be due to SCO transition as the complex was 100% HS at room temperature. The apparent increase in the concentration of HS Co(II) may be due to cooperative phenomenon.

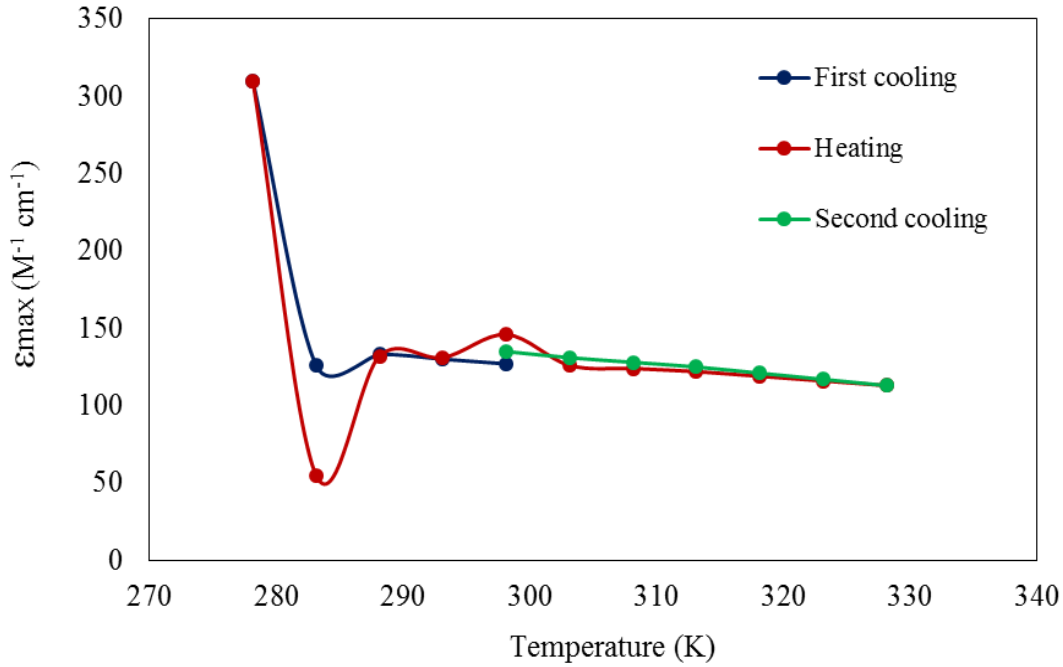

Figure 4.25 Temperature dependence of ε_{max} for **Complex 4** at 820 nm

(c) Thermal and mesomorphic properties

The **TGA** trace of **Complex 4** (**Figure 4.26**) shows almost similar thermal behavior as previously discussed complexes. The complex suffered a total weight loss of 88.2% at 246 °C to 690 °C due to loss of two BF_3 molecules and two L^{12} ligands (expected, 91.7%). The amount of residue at temperatures above 691 °C was 11.8%, which is in good agreement with the expected amount of 8.3% (assuming CoF_2). Its higher decomposition temperature (246 °C) compared to **Complexes 1-3** may be due to the absence of lattice H_2O (no hydrolyses of BF_4^- ion and C=N bonds of L^{12} ligands).

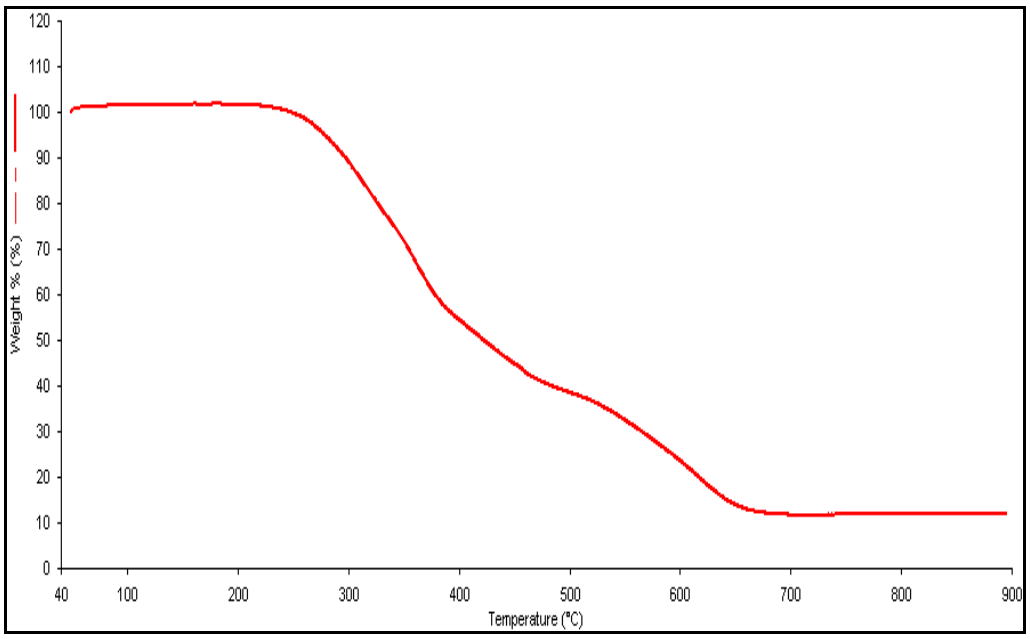

Figure 4.26 TGA trace of **Complex 4**

Its **DSC** scans (**Figure 4.27**) were similarly recorded for one heating-cooling cycle from 25 °C to 170 °C. On heating, there was an endothermic peak at 56.9 °C (ΔH = +71.4 kJ mol^{-1}), assigned to its melting temperature. However, there was no corresponding peak on cooling, which may indicate slow rate of phase formation.

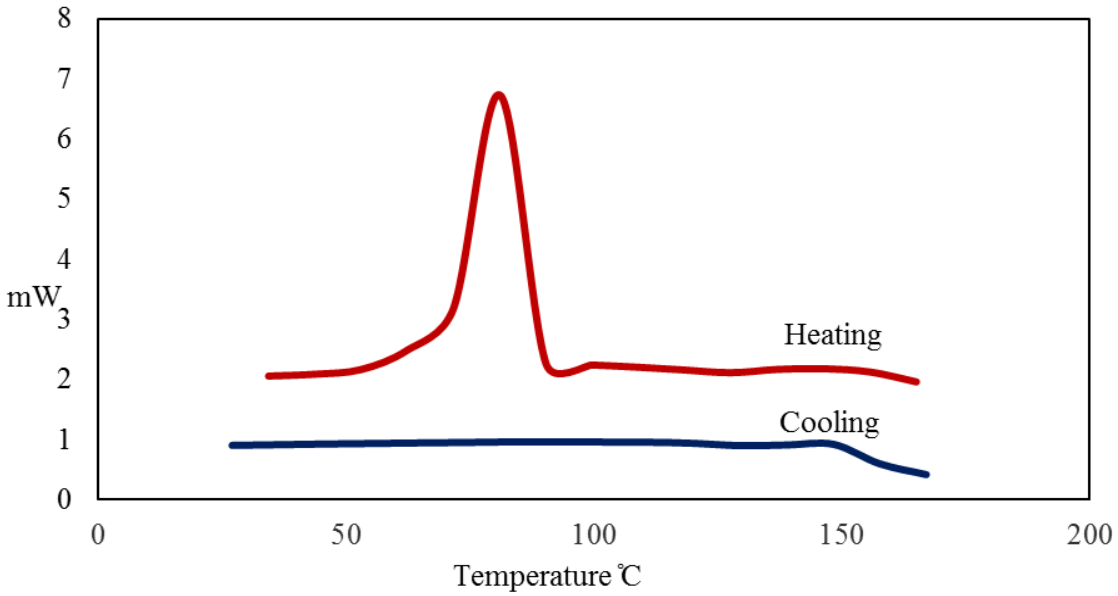

Figure 4.27 DSC of **Complex 4**. Endothermic peak up

Viewed under **POM**, **Complex 4** was observed to start melting at about 70 °C and to clear to an isotropic liquid (I) at 147 °C. On cooling from the isotropic liquid

phase, leaf-like optical textures developed at 140 °C (**Figure 4.28a**). When the sample was reheated and then cooled, similar optical texture was again observed at 115 °C (**Figure 4.28b**). The texture may be assigned to a columnar mesophase (*Col*). On further cooling, this texture gradually transformed to the spherulite texture of a crystalline phase (**Figure 4.28c**).

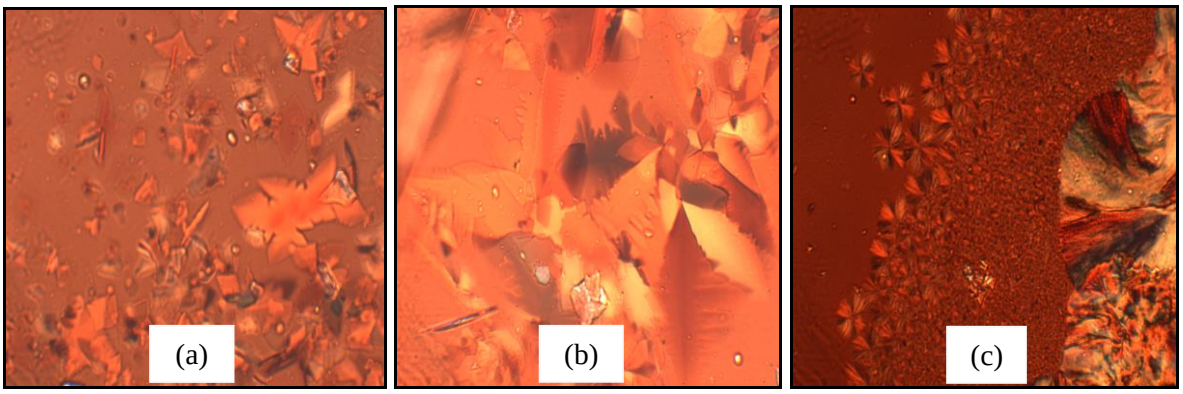

Figure 4.28 Photomicrographs of **Complex 4** on cooling from I at: (a) 140 °C; (b) 115 °C; and (c) room temperature

Similar mesophase was found for bis[1-(3',4',5'-trioctyloxyphenyl)-3-(3"-methyl-4"-octyl-oxyphenyl)propane-1,3-diketonate]copper(II) (**Figure 4.29**) reported by C. K. Lai *et. al* [8].

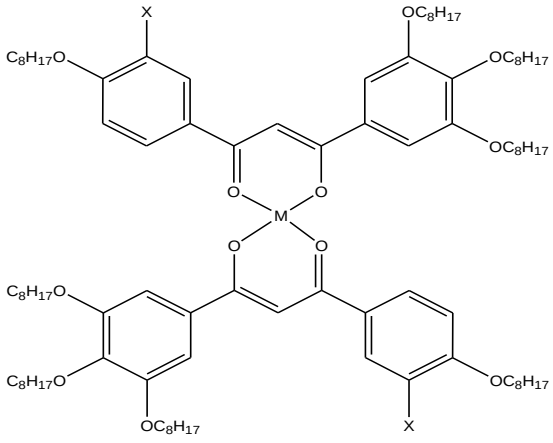

Figure 4.29 Molecular structure of bis[1-(3',4',5'-trioctyloxyphenyl)-3-(3"-methyl-4"-octyl-oxyphenyl)propane-1,3-diketonate]copper(II), M = Cu, X = CH_3 [8]

4.2.5 $[Co(L^{14})_2](BF_4)_2.H_2O$

2,6-Pyridinedicarboxaldehyde, 1-aminotetradecane and $Co(BF_4)_2.6H_2O$ reacted in methanol to form a red-brick powder (**Complex 5**) in good yield (88.8%). The powder was readily soluble in solvents similar to **Complexes 1-4**.

(a) Deduction of structural formula

Based on the same instrumental analyses as previously discussed, it is proposed that the structure of **Complex 5** was similar to that of **Complexes 1-4** (**Figure 4.1**).

The results of **elemental analyses** for carbon, hydrogen and nitrogen (**Table 4.8**) are in excellent agreement with those calculated for chemical formula $[Co(L^{14})_2](BF_4)_2.H_2O$ ($C_{70}H_{128}B_2CoF_8N_6O$; formula weight 1302.35 g mol^{-1}).

Table 4.8 Elemental analytical data for **Complex 5**

Element	**(%)**	
	Calculated	**Found**
Carbon	64.56	64.90
Hydrogen	9.91	9.90
Nitrogen	6.45	6.45

Its **ESI-MS** spectrum (**Figure 4.30**) shows peaks at m/z 1196.9 for $[Co(L^{14})_2(BF_3)]^+$ ion (calculated, 1196.9), 1128.9 for $[Co(L^{14})_2F]^+$ ion (calculated, 1129.1), and 555.0 for $[Co(L^{14})_2]^{2+}$ion (calculated, 555.1).

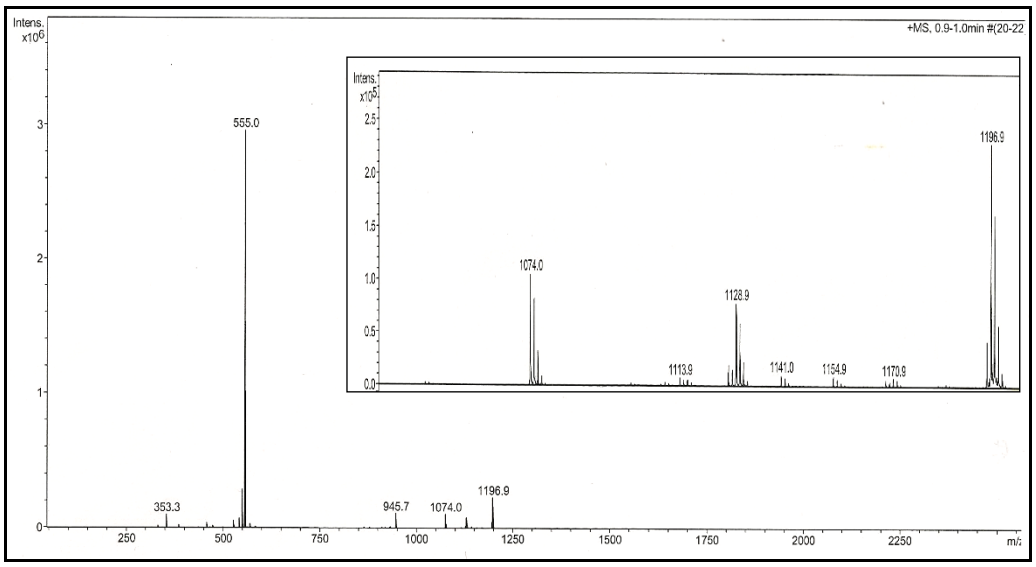

Figure 4.30 ESI-MS spectrum of **Complex 5**

Its **FTIR** spectrum (**Figure 4.31**) shows peaks at 2917 cm^{-1}, 1593 cm^{-1} and 1055 cm^{-1}. These peaks may be similarly assigned as for **Complexes 1-4.**

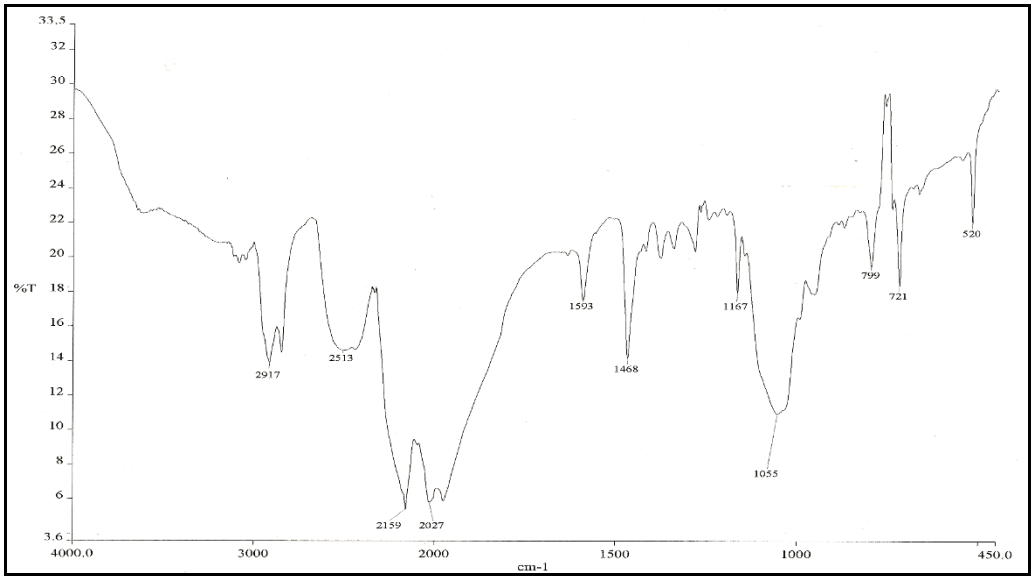

Figure 4.31 FTIR spectrum of **Complex 5**

Its **UV-visible** spectrum in $CHCl_3$ (**Figure 4.32**) shows bands at 756 nm (ε, 116 M^{-1} cm^{-1}), 650 nm (ε, 217 M^{-1} cm^{-1}), 548 nm (ε, 1153 M^{-1} cm^{-1}), 469 nm (ε, 1604 M^{-1} cm^{-1}), and 384 nm (ε, 2340 M^{-1} cm^{-1}). These electronic transitions may be similarly assigned as for **Complex 4**.

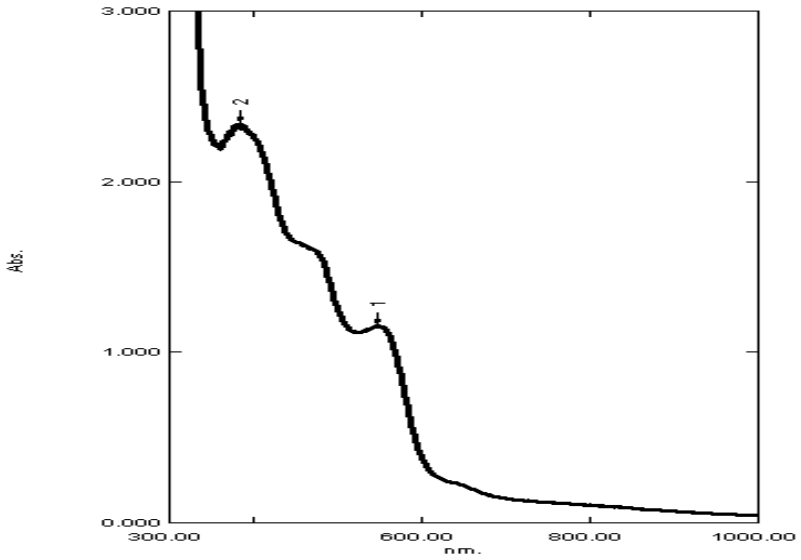

Figure 4.32 UV-visible spectrum of **Complex 5**

(b) Spin-crossover behavior

The $\chi_M^{corr}T$ value for **Complex 5,** similarly calculated as previously done from its proposed chemical formula (FW = 1302.35 g mol^{-1}), χ_g (3.38 x 10^{-6} cm^3 g^{-1}), χ_M (4.40 x 10^{-3} cm^3 mol^{-1}), χ_{dia} (-834.40 x 10^{-6} cm^3 mol^{-1}), and χ_M^{corr} (5.23 x 10^{-3} cm^3 mol^{-1}), is 1.53 cm^3 mol^{-1} K at 293 K. Thus, this complex was made up of 76.9% HS and 23.1% LS Co(II) at room temperature. Compared to **Complex 4**, the lower percentage of HS Co(II) in **Complex 5** is consistent with the presence of lattice H_2O in the latter complex.

The **temperature-dependence** ε_{max} values for **Complex 5** were similarly recorded as for **Complex 4**. The results (**Figure 4.33**) show almost similar behavior for the two complexes, and may be similarly explained.

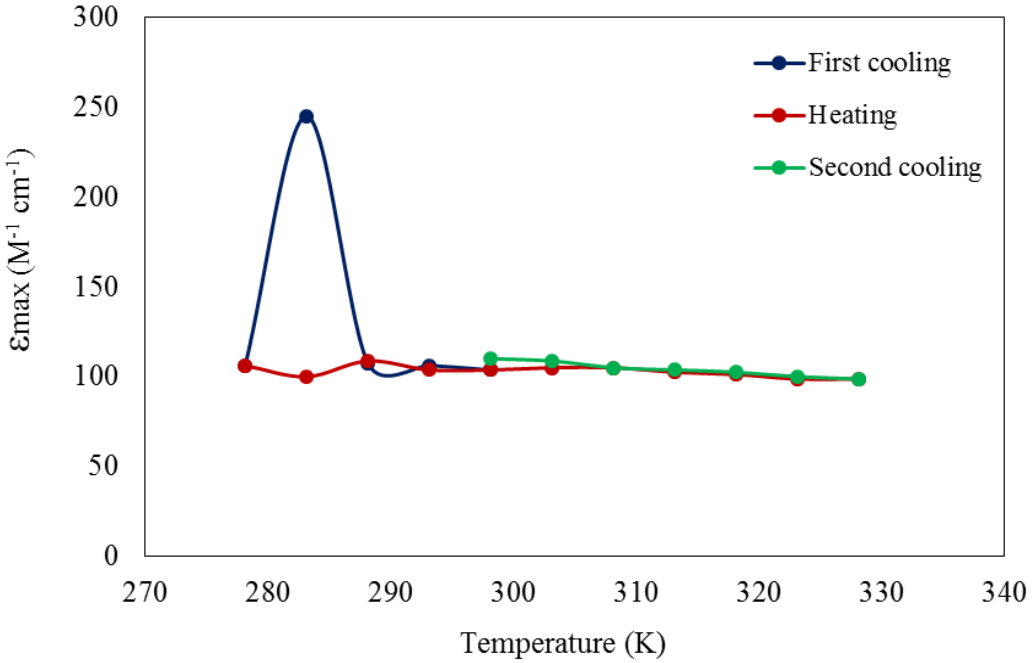

Figure 4.33 Temperature dependence of ε_{max} for **Complex 5** at 756 nm

(c) Thermal and mesomorphic properties

The **TGA** trace of **Complex 5** (**Figure 4.34**) shows similar thermal behavior as previously discussed complexes. The complex suffered weight losses of 1.0% at 85 °C to 192 °C due to the evaporation of lattice H_2O (expected, 1.4%) and 91.6% in the temperature range of 206 - 800 °C due to loss of two BF_3 molecules and two L^{14} ligands (expected, 91.2%). The amount of residue at temperatures above 800 °C was 7.3%, which is in good agreement with the expected amount of 7.4% (assuming CoF_2). Hence, its decomposition temperature (206 °C) was lower than **Complex 4** (T_{dec} = 246 °C), consistent with the presence of lattice H_2O in the former complex.

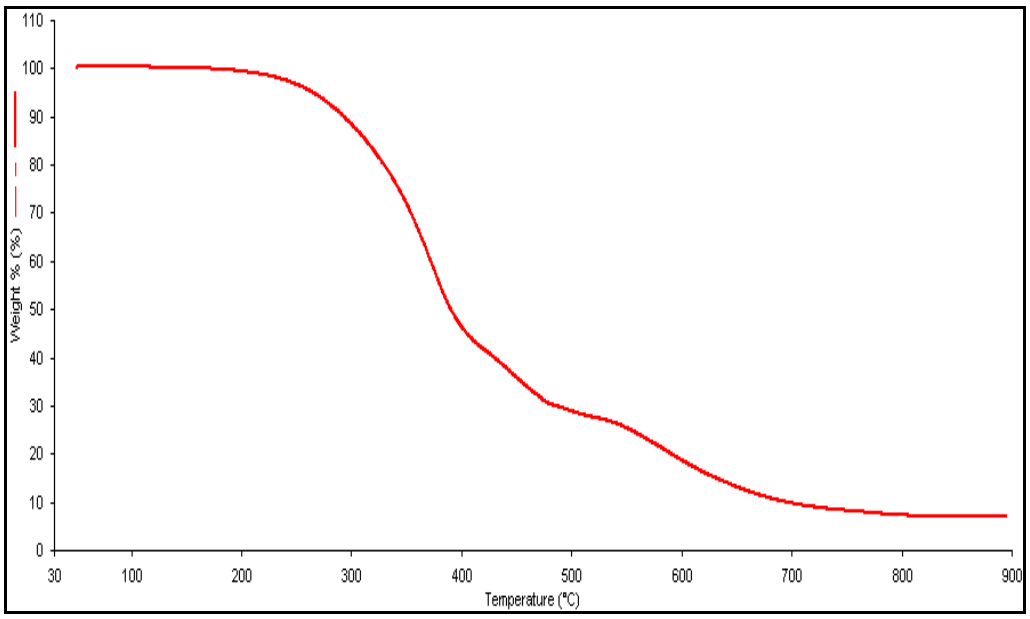

Figure 4.34 TGA trace of **Complex 5**

Its **DSC** scans (**Figure 4.35a** and **4.35b**) were similarly recorded as for previous complexes. There was a strong endothermic peak at 74.9 °C (ΔH = +68.5 kJ mol^{-1}) during first heating scan, assigned to its melting temperature. However, there was a weaker endothermic peak at 47.2 °C (ΔH = +24.7 kJ mol^{-1}) during second heating scan, and no peaks during first and second cooling scans. It may inferred from this that the complex underwent a structural change when heated, forming a new complex with a lower melting temperature.

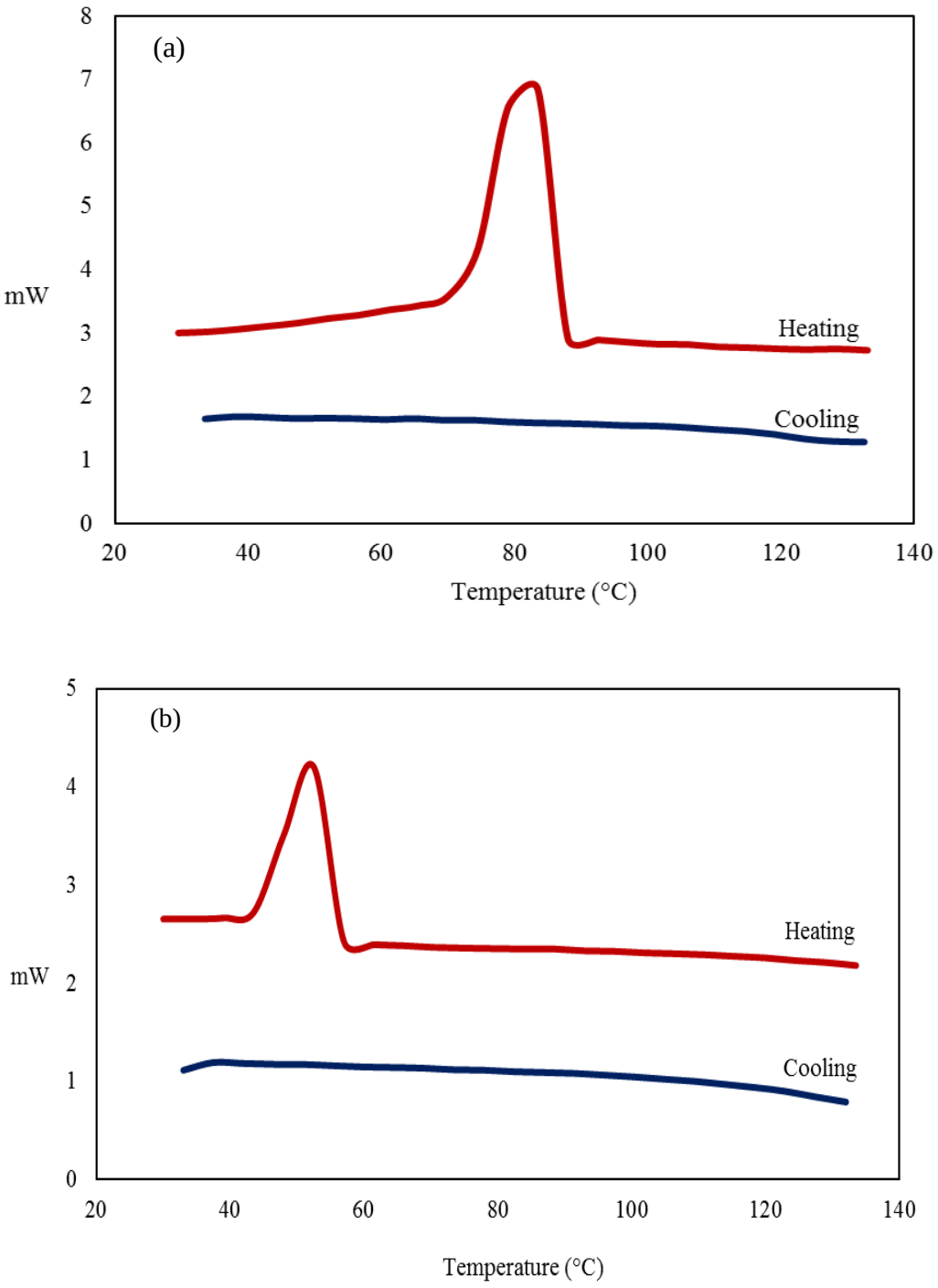

Figure 4.35 DSC of **Complex 5**: (a) first cycle; (b) second cycle. Endothermic peak up

Viewed under **POM**, **Complex 5** was observed to start melting at about 75 °C, showed an optical texture at 145 °C (**Figure 4.36a**), and cleared to an isotropic liquid at 164 °C. On cooling from the isotropic liquid phase, a fan-like optical texture, assigned to a hexagonal columnar (Col_h) mesophase, developed at 131 °C (**Figure 4.36b**). This mesophase then transformed to a broken-fan texture at 117.0 °C (**Figure 4.36c**). When

the sample was reheated and then cooled, similar optical texture was again observed at the same temperature. Hence, similar to **Complex 4**, this complex also exhibited liquid crystal properties of a discotic mesogen (*Col$_h$)* [9].

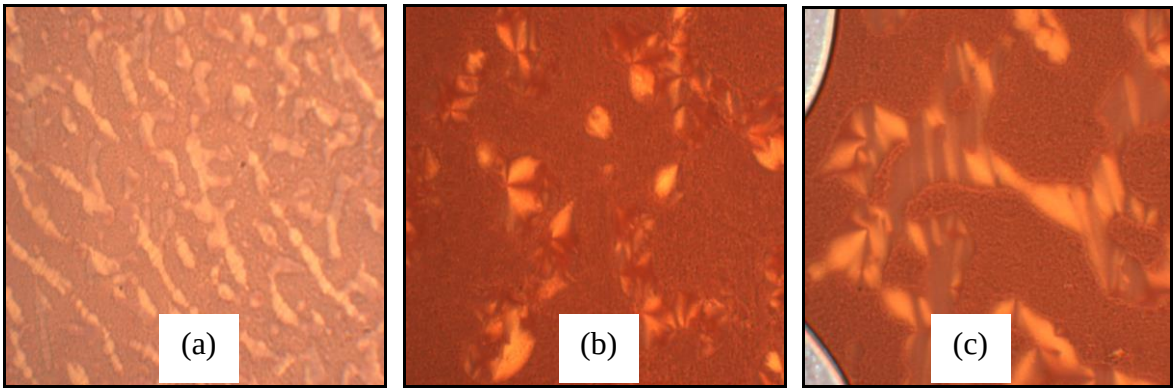

Figure 4.36 Photomicrographs of **Complex 5** on: (a) heating at 145 °C; (b) cooling at 131 °C; and (c) cooling at 117 °C

4.2.6 [Co(L^{16})$_2$](BF$_4$)$_2$.H$_2$O

2,6-Pyridinedicarboxaldehyde, 1-aminohexadecaneand $Co(BF_4)_2.6H_2O$ reacted in methanol to form a fine red-brick powder (**Complex 6**) in good yield (92.0%). The powder was readily soluble in solvents similar to **Complexes 1**-**5**.

(a) Deduction of structural formula

Based on the same instrumental analyses as previously discussed, it is proposed that the structure of **Complex 6** was similar to that of **Complex 1** (**Figure 4.1**).

The results of **elemental analyses** for carbon, hydrogen and nitrogen (**Table 4.9**) are in excellent agreement with those calculated for chemical formula, $[Co(L^{16})_2](BF_4)_2.H_2O$ ($C_{78}H_{144}B_2CoF_8N_6O$; formula weight 1414.56 g mol^{-1}).

Table 4.9 Elemental analytical data for **Complex 6**

Element	(%)	
	Calculated	**Found**
Carbon	66.23	66.65
Hydrogen	10.26	10.30
Nitrogen	5.94	5.95

Its **ESI-MS** spectrum (**Figure 4.37**) shows peaks at m/z 1309.1 for $\{[Co(L^{16})_2](BF_4)\}^+$ ion (calculated, 1309.1), and 611.0 for $[Co(L^{16})_2]^{2+}$ ion (calculated, 611.1).

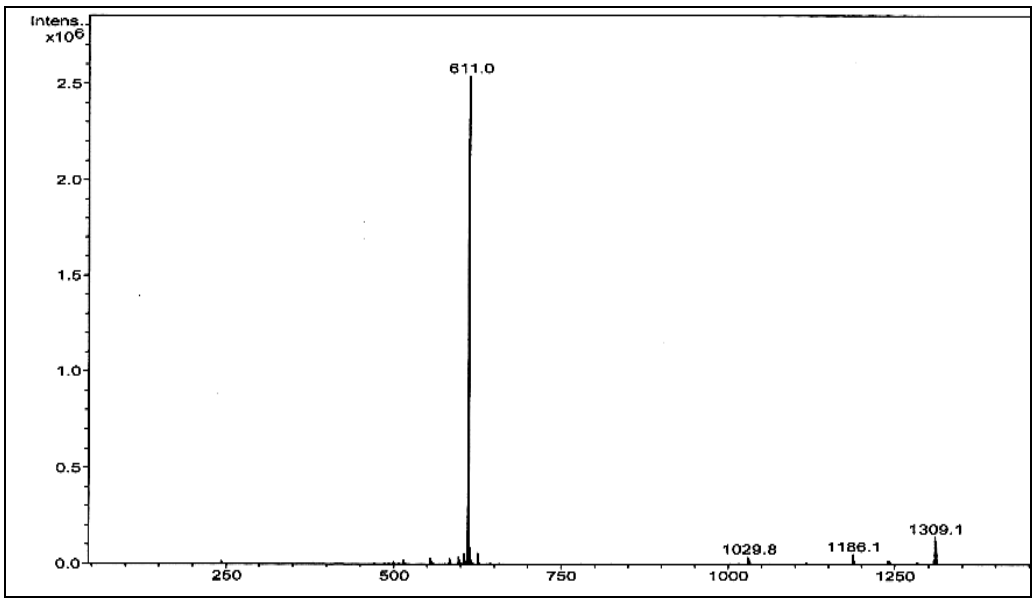

Figure 4.37 ESI-MS spectrum of **Complex 6**

Its **FTIR** spectrum (**Figure 4.38**) shows peaks at 2918 cm^{-1}, 2850 cm^{-1}, 1591 cm^{-1} and 1058 cm^{-1}. These peaks may be similarly assigned as for **Complexes 1-5**.

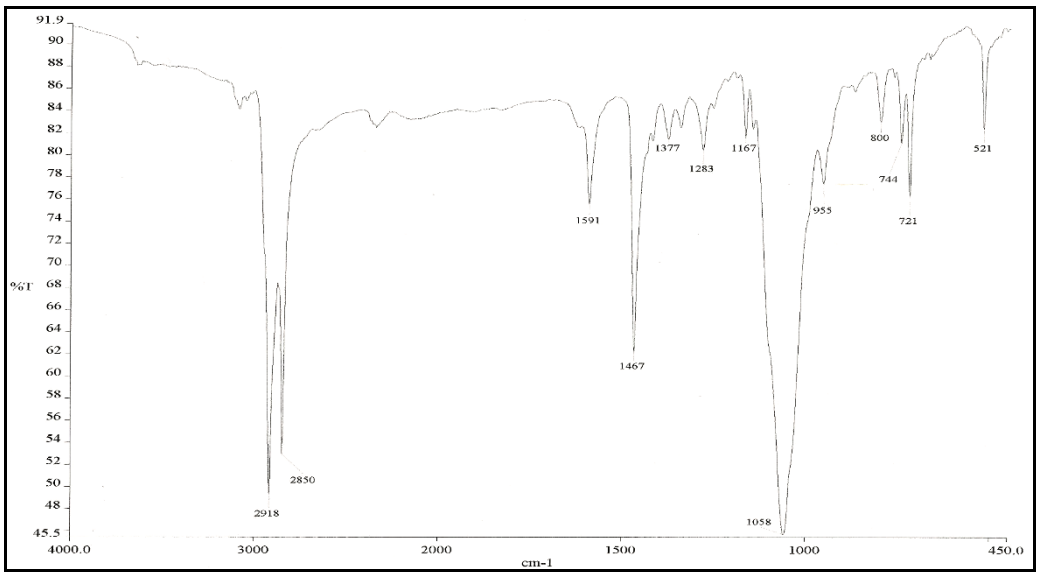

Figure 4.38 FTIR spectrum of **Complex 6**

Its **UV-visible** spectrum in $CHCl_3$ (**Figure 4.39**) shows broad *d-d* bands at 815 nm (ε, 104 M^{-1} cm^{-1}), 648 nm (ε, 226 M^{-1} cm^{-1}), and 550 nm (ε, 1359 M^{-1} cm^{-1}). These electronic transitions may be similarly assigned as for **Complexes 4** and **5**.

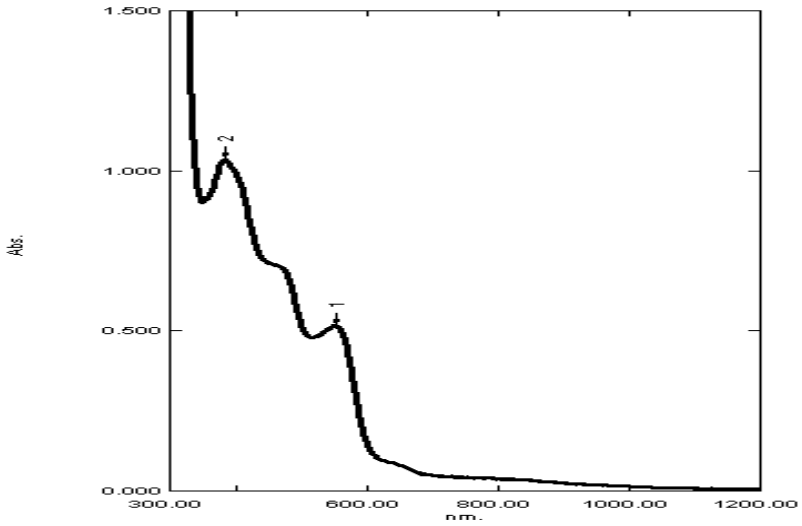

Figure 4.39 UV-visible spectrum of **Complex 6**

(b) Spin-crossover behavior

The $\chi_M^{corr}T$ value for **Complex 6,** similarly calculated as previously done from its proposed chemical formula (FW = 1414.56 g mol^{-1}), χ_g (5.20 x 10^{-6} cm^3 g^{-1}),

χ_M (5.94 x 10^{-3} cm^3 mol^{-1}), χ_{dia} (-726.52 x 10^{-6} cm^3 mol^{-1}) and χ_M^{corr} (6.67 x 10^{-3} cm^3 mol^{-1}), was 1.94 cm^3 K mol^{-1} at 293 K. Hence, similar to **Complex 4**, this complex was made up of 100% HS Co(II) at room temperature. From this, it may be inferred that the fastening effect of the long alkyl chain was the dominant factor compared to lattice H_2O in determining the spin state of this complex.

Its **variable-temperature magnetic susceptibilities** were measured for three cooling and heating cycles using the **SQUID** magnetometer. For the first cycle, the sample was first cooled from 300 K to 5 K, and then heated from 5 K to 370 K. For the second cycle, the sample was cooled to 156 K, and then heated to 370 K. For the third cycle, the sample was cooled to 317 K, and then heated to 360 K. The $\chi_M T$ vs. T plots are shown in **Figure 4.40**.

During the first cycle, the $\chi_M T$ values decreased gradually from 1.40 cm^3 K mol^{-1} at 296 K to a minimum value of 0.44 cm^3 K mol^{-1} at 4 K. When the sample was reheated, the $\chi_M T$ values increased gradually following similar trend as initial cooling to a maximum value of 2.13 cm^3 K mol^{-1} at 372 K. No thermal hysteresis was observed from this cycle.

However, during the second cycle, a different trend was observed. Upon cooling from 372 K, the $\chi_M T$ values initially decreased gradually from 2.13 cm^3 K mol^{-1} to 1.73 cm^3 K mol^{-1} at 327 K and then decreased abruptly to 1.41 cm^3 K mol^{-1} at 324 K. On further cooling, the value decreased gradually to a minimum value of 0.71 cm^3 K mol^{-1} at 156 K. Upon heating, the value increased gradually to 1.50 cm^3 K mol^{-1} at 340 K following the same trend as previous cooling. The $\chi_M T$ value then increased abruptly to 1.87 cm^3 K mol^{-1} at 348 K. On further heating, the value increased gradually to 2.02 cm^3 K mol^{-1} at 368 K. Wide hysteresis loop (ΔT = 19 K) was observed as its spin crossover at $T_{½}\downarrow$= 326 K and $T_{½}\uparrow$= 345 K.

On the third cycle, similar trend as second cycle was observed. Upon cooling from 368 K, the $\chi_M T$ values decrease gradually from 2.02 cm^3 K mol^{-1} to 1.72 cm^3 K mol^{-1} at 328 K and then decreased abruptly at 1.39 cm^3 K mol^{-1} at 324 K. On further cooling, the $\chi_M T$ was decreased gradually to 1.32 cm^3 K mol^{-1} at 316 K. Upon heating, the $\chi_M T$ was increased gradually to 1.58 cm^3 K mol^{-1} at 342 K following the same trend as previous cooling, and then increased abruptly to 1.80 cm^3 K mol^{-1} at 346 K. On further heating, the values increased gradually to 1.91 cm^3 K mol^{-1} at 360 K. Wide hysteresis loop (ΔT = 18 K) was again observed as its spin crossover at $T_{½}\downarrow$= 326 K and $T_{½}\uparrow$= 344 K. Thus, from second and third cycle, the SCO of **Complex 6** was reversible.

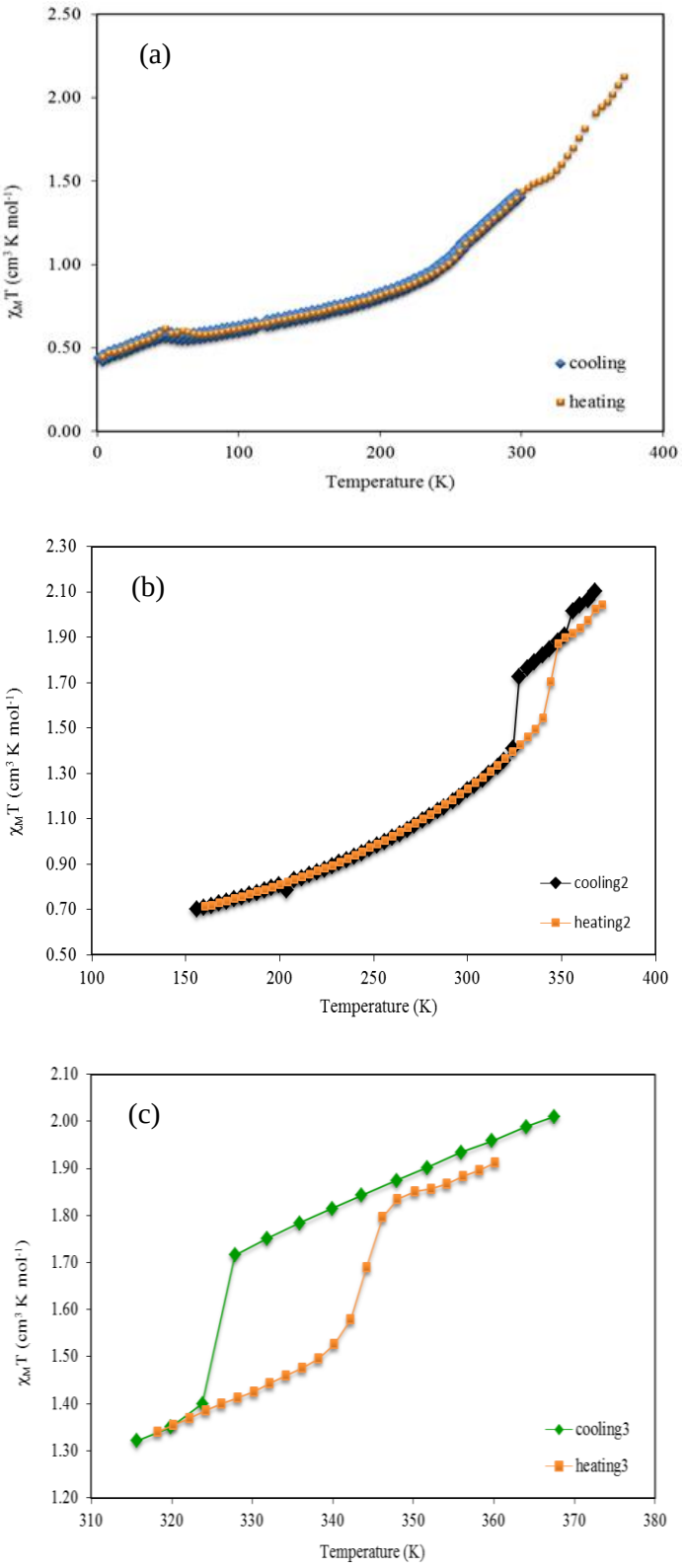

Figure 4.40 Plots of $\chi_M T$ vs. T for **Complex 6**: (a) first cycle (300 K to 5 K); (b) second cycle (370 K to 156 K); and (c) third cycle (370 K to 317 K)

Its **temperature-dependence ε_{max}** were similarly recorded as for **Complexes 4** and **5**. The results (**Figure 4.41**) show almost similar behavior as these complexes and may be similarly explained.

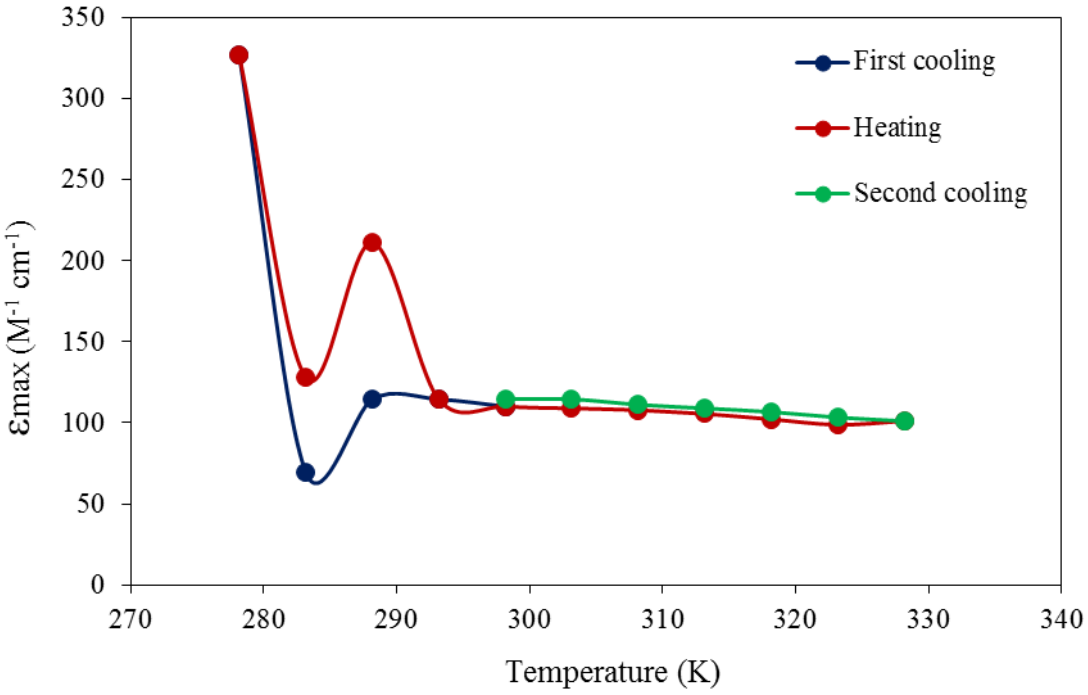

Figure 4.41 Temperature dependence of ε_{max} for **Complex 6** at 795 nm

(c) Thermal and mesomorphic properties

The **TGA** trace of **Complex 6** (**Figure 4.42**) shows similar thermal behavior as previously discussed complexes. It suffered weight losses of 0.9% at 92 °C to 180 °C due to the evaporation of lattice H_2O (expected, 1.3%) and 91.5% in the temperature range of 245 - 657 °C due to loss of two BF_3 molecules and two L^{16} ligands (expected, 91.9%). The amount of residue at temperatures above 657 °C was 7.6%, which is in good agreement with the expected amount of 6.9% (assuming CoF_2). Hence, its decomposition temperature (245 °C) was higher than **Complex 5** (T_{dec} = 206 °C) but similar to **Complex 4** (T_{dec} = 246 °C), consistent with the increase in the alkyl chain length and presence of lattice H_2O.

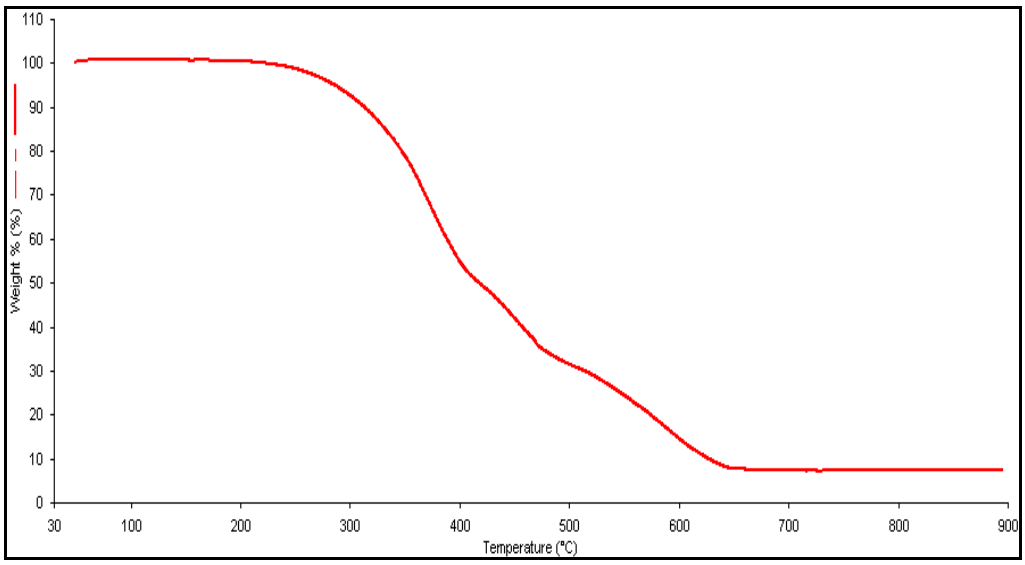

Figure 4.42 TGA thermograph of **Complex 6**

Its **DSC** scans (**Figure 4.43a** and **4.43b**) were similarly recorded as for previous complexes. The data and assignment were collected in **Table 4.10**. The phase changes were similar to **Complex 5**, and may be similarly explained.

Table 4.10 DSC data for **Complex 6**

Cycle		**Temperature (˚C)**	**ΔH (kJ mol^{-1})**	**Assignment**
1	Heating	72.6	+11.2	Cr-Cr transition
		82.3	+97.0	Melting temperature
	Cooling	46.6	-44.0	Recrystallization temperature
		40.0	-7.4	Cr-Cr transition
2	Heating	42.2	+16.4	Cr-Cr transition
		53.7	+56.6	Melting temperature
		72.0	+7.7	N-Col transition
	Cooling	45.8	-6.4	Cr-Cr transition
		40.5	-28.4	Recrystallization temperature

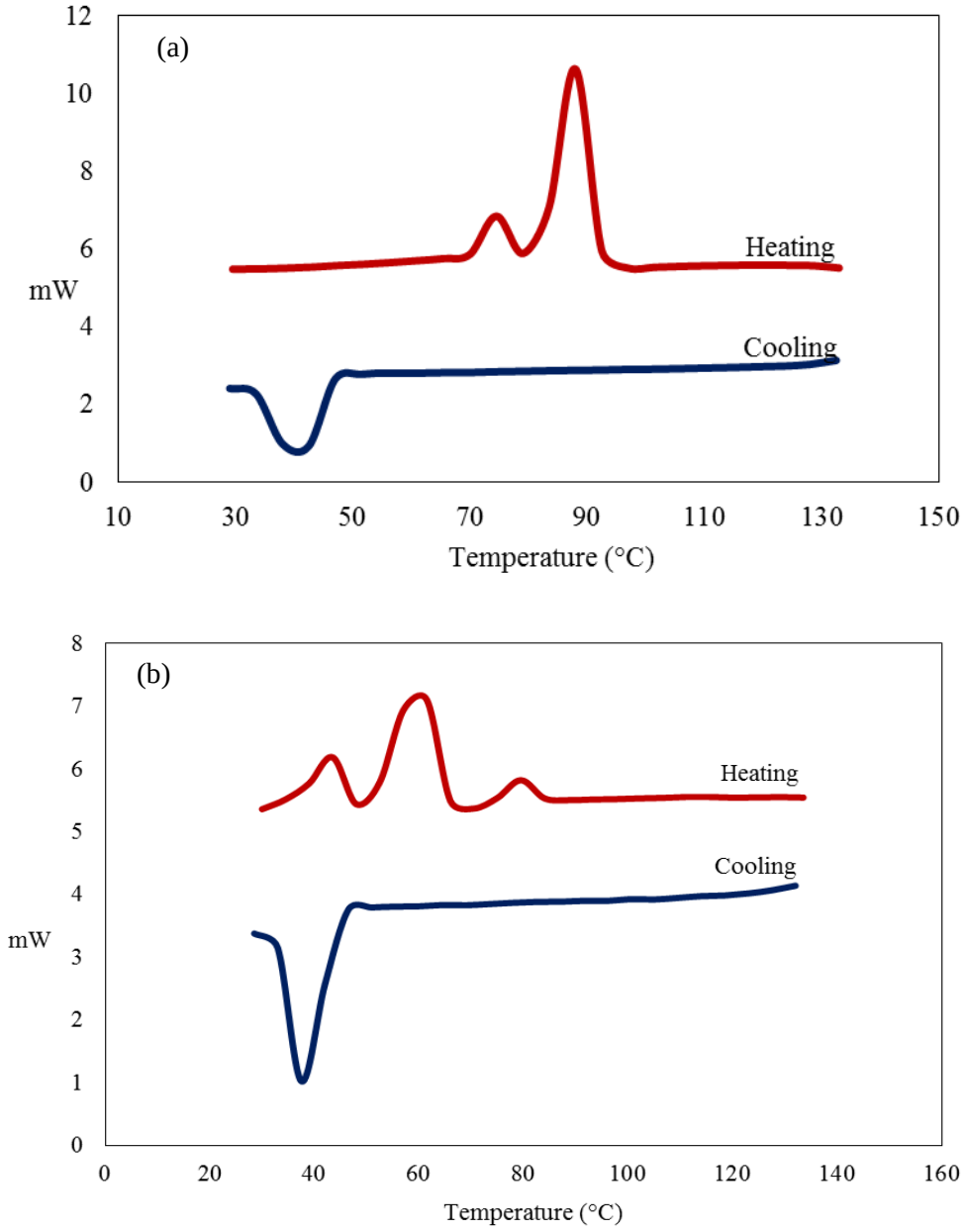

Figure 4.43 DSC of **Complex 6**: (a) first cycle; (b) second cycle. Endothermic peak up

Viewed under **POM**, **Complex 6** was observed to start melting at about 80 °C and to clear to an isotropic liquid at about 160 °C. However, the *Col* mesophase (**Figure 4.44**) was only observed on heating, consistent with structural changes noted above.

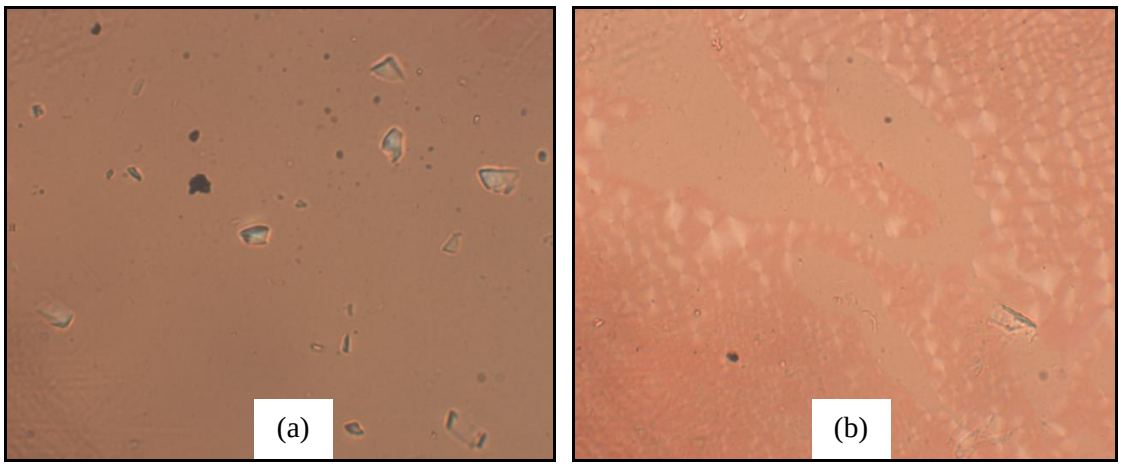

Figure 4.44 Photomicrographs of **Complex 6** on: (a) first heating at 154 °C; and (b) second heating at 150 °C

4.2.7 Summary

All experimental data for $[Co(L^n)_2](BF_4)_2$ are summarized in **Table 4.11** and **Table 4.12**. Several general points are: (a) all complexes were octahedral, and except for **Complex 4**, were hydrated; (b) HS complexes were preferred for long alkyl chains and in the absence of lattice H_2O; (c) the decomposition temperatures increased with alkyl chain length (from 97 to 246 °C), and were lowered by lattice H_2O; and (d) complexes with n = 12, 14, and 16 exhibited liquid crystal properties.

Table 4.11 Summary for **Complexes 1-3**

Complex	**1**	**2**	**3**
Structural formula	$[Co(L^6)_2](BF_4)_2.½H_2O$	$[Co(L^8)_2](BF_4)_2.H_2O$	$[Co(L^{10})_2](BF_4)_2.½H_2O$
λ_{max}/nm (ε_{max}/M^{-1} cm^{-1})	650 (267), 545 (921)	684 (273), 507 (759)	664 (248), 555 (818)
T_{dec}/°C	97	118	209
$\chi_M T$ (cm^3 K mol^{-1})	0.99 (41.0% HS; 59.0% LS)	1.39 (67.6% HS; 32.4% LS)	1.07 (46.3% HS; 53.2% LS)
Liquid crystal properties	Not mesogenic	Not mesogenic	Not mesogenic

Table 4.12 Summary for **Complexes 4-5**

Complex	**4**	**5**	**6**
Structural formula	$[Co(L^{12})_2](BF_4)_2$	$[Co(L^{14})_2](BF_4)_2.H_2O$	$[Co(L^{16})_2](BF_4)_2.H_2O$
λ_{max}/nm (ε_{max}/M^{-1} cm^{-1})	822 (100), 650 (229)	756 (116), 650 (217)	815 (104), 648 (226)
T_{dec}/°C	246	206	245
$\chi_M T$ (cm^3 K mol^{-1})	1.95 (100% HS)	1.53 (76.9% HS; 23.1% LS)	1.43 (100% HS)
Liquid crystal properties	Mesogenic (*Col*)	Mesogenic (*Col*)	Mesogenic (*Col*)

4.3 $[Co(L^n)_2](ClO_4)_2$

The second phase of this research was to compare the effect of a larger anion, namely ClO_4^- ion, with that of BF_4^- ion on the structure, spin crossover behavior and thermal properties of $[Co(L^n)_2]^{2+}$ ions.

4.3.1 $[Co(L^{12})_2](ClO_4)_2$

2,6-pyridinedicarboxaldehyde, 1-aminododecane and $Co(ClO_4)_2.6H_2O$ reacted in methanol to form a red-brick powder (**Complex 7**), in good yield (48.5%). The powder was readily soluble in solvents similar to **Complexes 1-6**.

(a) Deduction of structural formula

Based on the same instrumental analyses as previously discussed, it is proposed that the structure of **Complex 7** was similar to that of **Complexes 1-6** (**Figure 4.1**).

The results of **elemental analyses** for carbon, hydrogen and nitrogen (**Table 4.13**) were in excellent agreement with those calculated for chemical formula $[Co(L^{12})_2](ClO_4)_2$ ($C_{62}H_{110}Cl_2CoN_6O_8$; formula weight 1197.41 g mol^{-1}).

Table 4.13 Elemental analytical data for **Complex 7**

Element	(%)	
	Calculated	**Found**
Carbon	62.19	61.90
Hydrogen	9.26	9.25
Nitrogen	7.02	7.00

Its **ESI-MS** spectrum (**Figure 4.45**) shows peaks at m/z 1096.8 for $[Co(L^{12})_2](ClO_4)]^+$ ion (calculated, 1096.8), 1014.8 for $[Co(L^{12})_2(OH)]^+$ ion (calculated, 1014.8), and 498.9 for $[Co(L^{12})_2]^{2+}$ ion (calculated, 98.9). It is probable that the OH^- ion

found for the species at m/z 1014.8 may be formed from the hydrolysis of ClO_4^- ion, according to the following equation:

$$ClO_4^- + H_2O \rightleftharpoons HClO_4 + OH^-$$

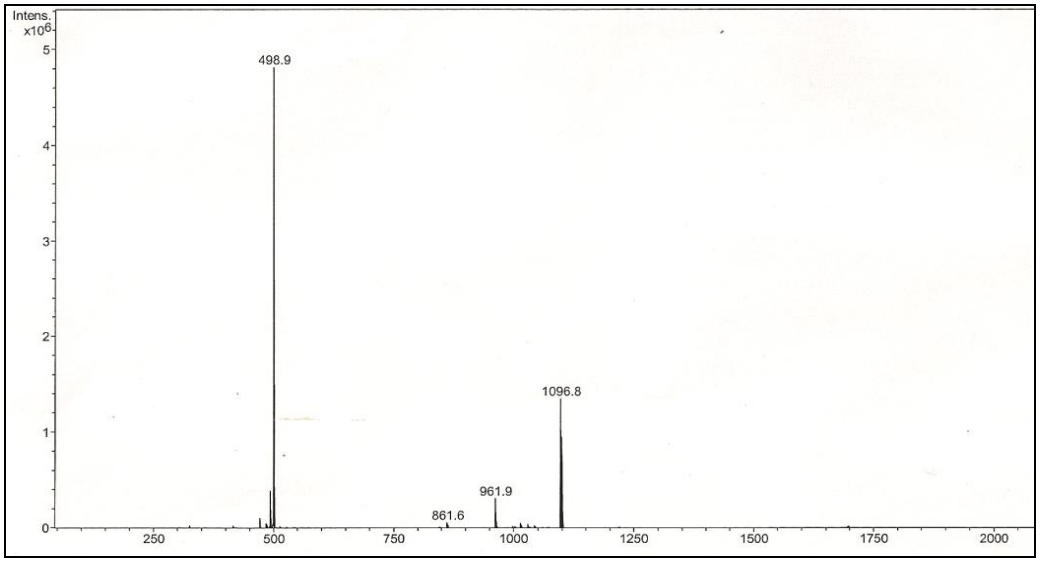

Figure 4.45 ESI-MS of **Complex 7**

Its **FTIR** spectrum (**Figure 4.46**) shows peaks similarly found for **Complexes 1-6** at 2919 cm^{-1}, 2850 cm^{-1} and 1591 cm^{-1}, and hence may be similarly assigned. Additionally, there are two overlapping peaks at 1082 cm^{-1} for C-N and ClO_4^- ion, and peaks at 958 $cm^{-1}$and 622 cm^{-1} for symmetric ClO_4^- stretch and asymmetric bend respectively [10].

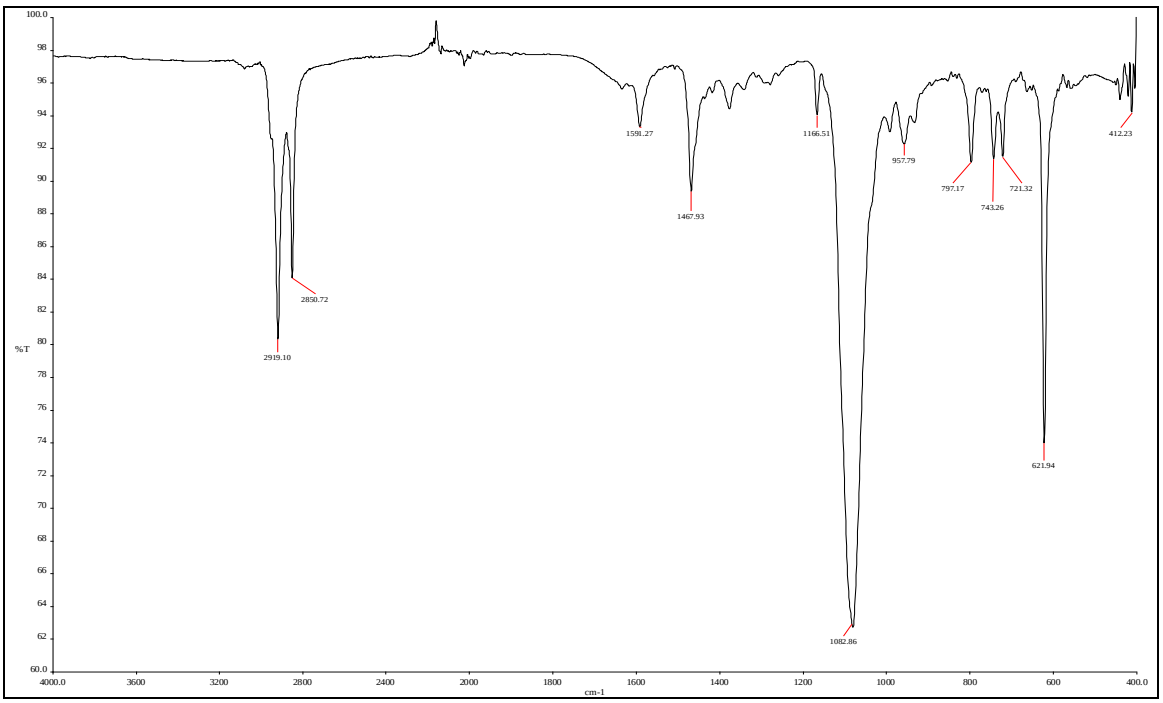

Figure 4.46 FTIR spectrum of **Complex 7**

Its **UV-visible** spectrum in CH_3Cl (**Figure 4.47**) shows broad bands at 770 nm (ε, 190 M^{-1} cm^{-1}), 643 nm (ε, 365 M^{-1} cm^{-1}), 476 nm (ε, 2270 M^{-1} cm^{-1}). These electronic transitions may be similarly assigned as for **Complex 4**.

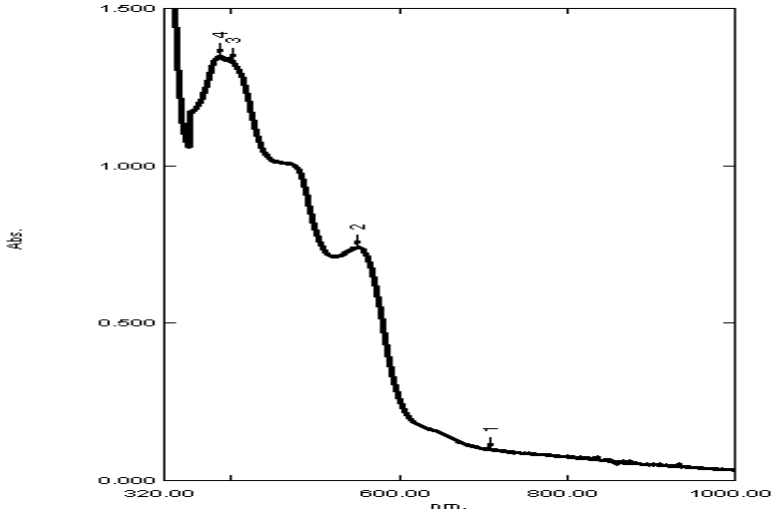

Figure 4.47 UV-visible spectrum of **Complex 7**

(b) Spin crossover behavior

The $\chi_M^{corr}T$ value for **Complex 7**, similarly calculated as previously done from its proposed chemical formula (**FW** = 1195.30 g mol^{-1}), χ_g (-0.24 x 10^{-5} cm^3 g^{-1}), χ_M (2.86 x 10^{-3} cm^3 mol^{-1}), χ_{dia} (-738.32 x 10^{-6} cm^3 mol^{-1}) and χ_M^{corr} (3.60 x 10^{-3} cm^3 mol^{-1}), is 1.07 cm^3 mol^{-1} K. Thus, this complex was made up of 46.3% HS and 53.7% LS Co(II) at room temperature. Hence, it has a lower percentage of HS Co(II) compared to **Complex 4** ($[Co(L^{12})_2](BF_4)_2$); 100% HS). This was due to smaller BF_4^- anion (compared to ClO_4^-) which stabilized the HS state [11], as similarly observed by Gütlich et al. [12]. It was proposed that the steric interactions involving groups closer to the metal center stabilize the HS state.

Its **temperature-dependence** ε_{max} values were similarly measured as for **Complex 4**. However, the results (**Figure 4.48**) were slightly different. During the initial cooling, the ε_{max} values remained almost unchanged at about 190 M^{-1} cm^{-1} from 298 to 283 K. Then, the value decreased abruptly to 100 M^{-1} cm^{-1} at 278 K. Upon heating, the ε_{max} value increased abruptly to about 225 M^{-1} cm^{-1} at 283 K, then decreased back to about 190 M^{-1} cm^{-1} at 288 K, and then remained unchanged on further heating to 328 K, followed by cooling to room temperature. The results suggest the occurrence of reversible HS-to-LS transition in the temperature range of 283 – 278 K, consistent with the effect of the larger ClO_4^- ion, proposed previously.

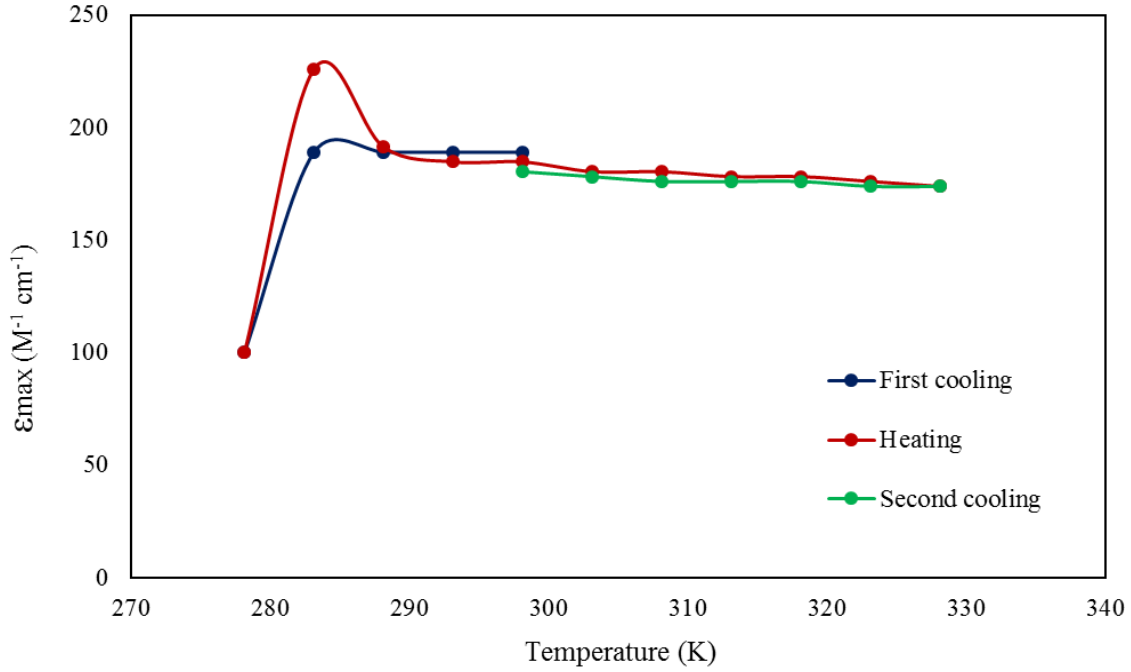

Figure 4.48 Temperature dependence of ε_{max} for **Complex 7** at766 nm

(c) Thermal and mesomorphic properties

The **TGA** trace of **Complex 7** (**Figure 4.49**) shows almost similar thermal behavior as **Complex 4**. It suffered an initial weight loss of 8.7% in the temperature range 161-245 °C, due to loss of three O_2 molecules (from ClO_4^- ions, expected 8.0%). This was followed by further loss of 80.4% in the temperature range 245 – 840 °C, due to a loss of another O_2 molecule and decomposition of two L^{12} ligands (expected, 81.1%). The amount of residue at temperatures above 840 °C was 10.9%, which is in good agreement with the expected amount of 10.8% (assuming pure $CoCl_2$). Hence, its decomposition temperature was almost similar to **Complex 4** (T_{dec} = 246 °C). Thus, the anionic size did not have any effect on the decomposition temperatures of these complexes.

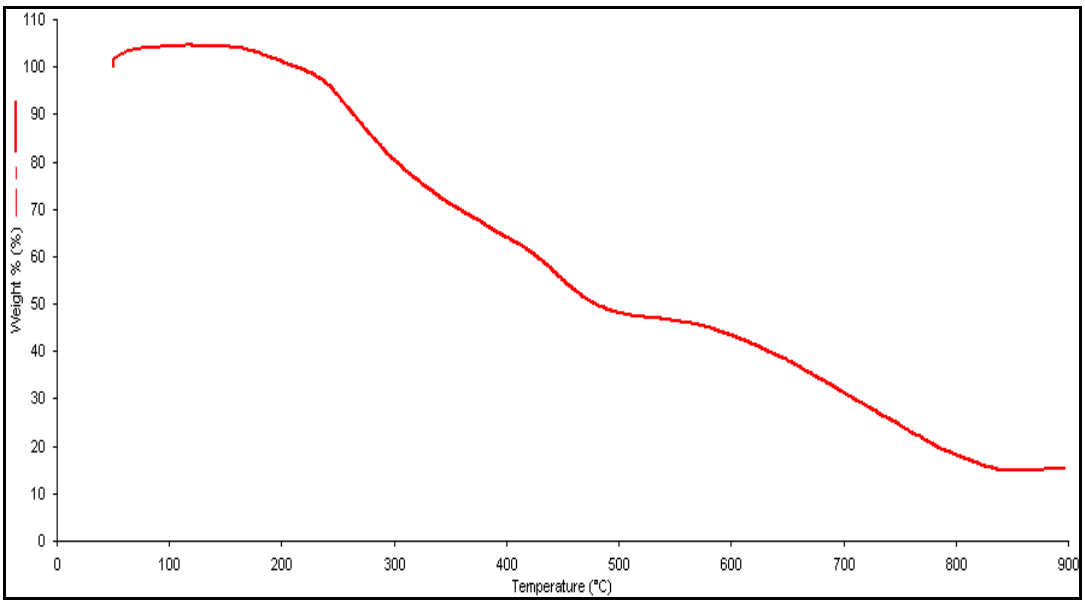

Figure 4.49 TGA of **Complex 7**

Its **DSC** scans (**Figure 4.50**) were similarly recorded as for **Complex 4**. On heating, there was an endothermic peak at 76.1 °C (ΔH = +40.8 kJ mol^{-1}), assigned to its melting temperature. However, there was no corresponding peak on cooling, which may indicate slow rate of phase formation.

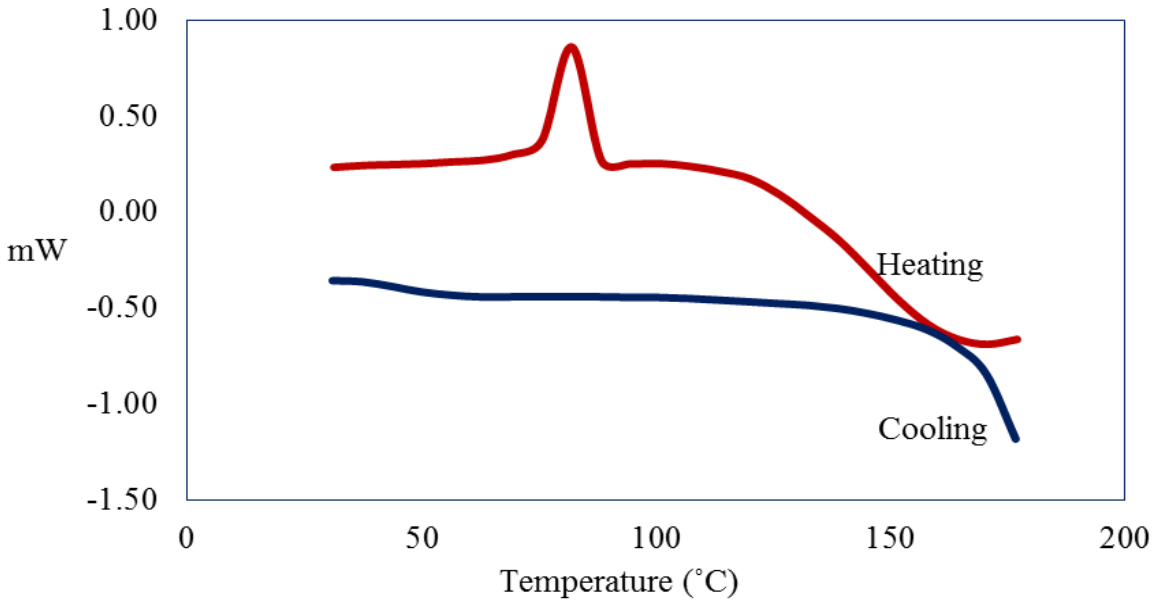

Figure 4.50 DSC of **Complex 7**

Viewed under **POM**, **Complex 7** was observed to melt at about 75 °C and to clear to an isotropic liquid at 160°C. However, on cooling from the isotropic liquid

phase, no optical textures were observed. Hence, in contrast to **Complex 4** ($Co(L^{12})_2](BF_4)_2$), **Complex 7** did not exhibit any mesomorphic properties, consistent with the stronger Co(II)-L^{12} bonds expected for the LS Co(II) in the latter complex.

4.3.2 $[Co(L^{16})_2](ClO_4)_2$

2,6-pyridinedicarboxaldehyde, 1-aminohexadecane and $Co(ClO_4)_2.6H_2O$ reacted in methanol to form a red-brick powder (**Complex 8**) in low yield (27.2%). The powder was readily soluble in solvents similar to **Complexes 1-7**.

(a) Deduction of structural formula

Based on the same instrumental analyses as previously discussed, it is proposed that the structure of **Complex 8** was similar to that of previously discussed complexes.

The results of **elemental analyses** for carbon, hydrogen and nitrogen (**Table 4.14**) are in excellent agreement with those calculated for chemical formula, $[Co(L^{16})_2](ClO_4)_2$ ($C_{78}H_{142}Cl_2CoN_6O_8$; formula weight 1419.90 g mol^{-1}).

Table 4.14 Elemental analytical data for **Complex 8**

Element	**(%)**	
	Calculated	**Found**
Carbon	65.89	65.95
Hydrogen	10.07	10.25
Nitrogen	5.91	5.95

Its **ESI-MS** spectrums (**Figure 4.51**) shows peaks at m/z 1321.0 for $\{[Co(L^{16})_2]ClO_4\}^+$ ion (calculated, 1321.0), m/z 1239.1 for $[Co(L^{16})_2(OH)]^+$ (calculated, 1239.1) and m/z 611.0 for $[Co(L^{16})_2]^{2+}$ ion (calculated, 611.0).

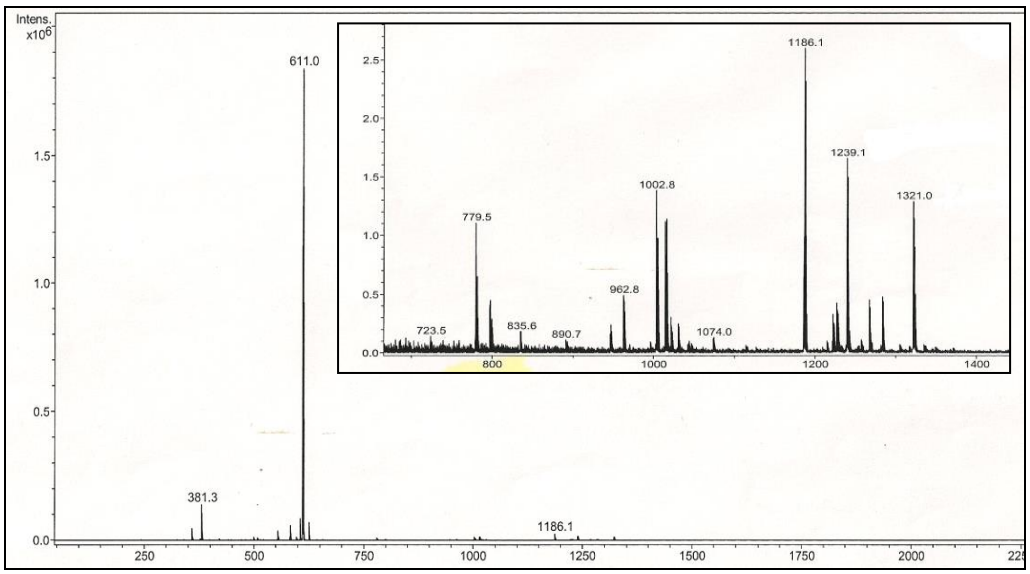

Figure 4.51 ESI-MS of **Complex 8**

Its **FTIR** spectrum (**Figure 4.52**) shows peaks at 2917 cm^{-1}, 2850 cm^{-1}, 1592 cm^{-1}, 1085 cm^{-1} and 622 cm^{-1}. These peaks may be similarly assigned as for **Complex 7**.

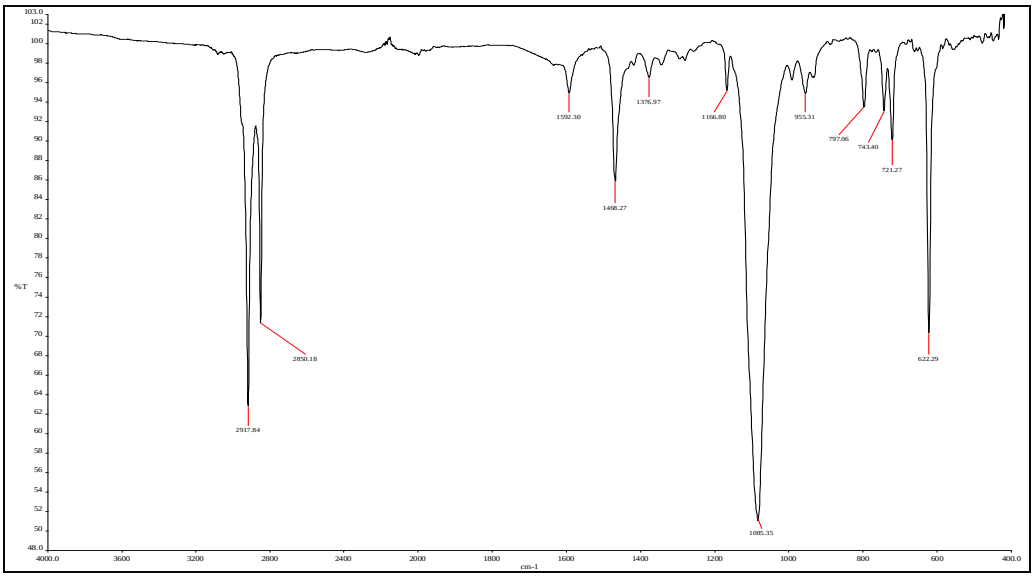

Figure 4.52 FTIR spectrum of **Complex 8**

Its **UV-visible** spectrum in chloroform (**Figure 4.53**) shows bands at 820 nm (ε, 105 M^{-1} cm^{-1}), 650 nm (ε, 248 M^{-1} cm^{-1}), 553 nm (ε, 1488 M^{-1} cm^{-1}), 466 nm (ε, 2011 M^{-1} cm^{-1}) and 396 nm (ε, 2655 M^{-1} cm^{-1}). These electronic transitions may be similarly assigned as for **Complex 7**.

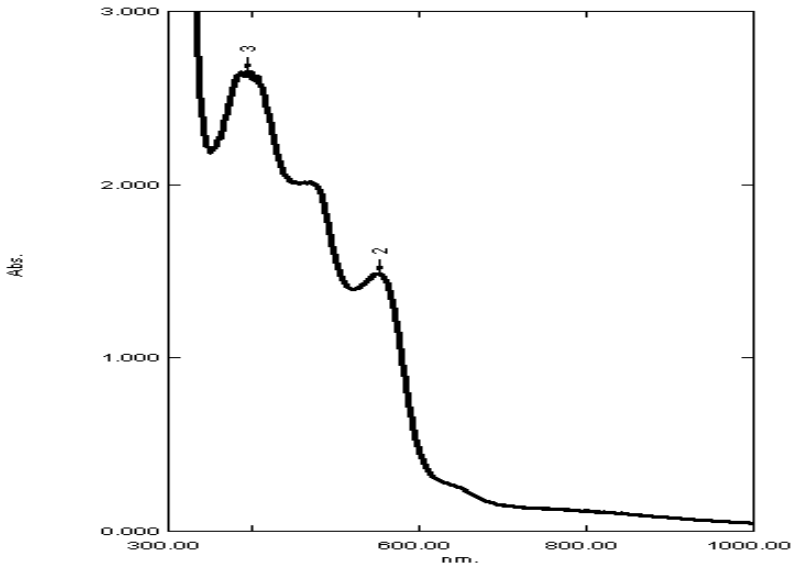

Figure 4.53 UV-visible spectrum of **Complex 8**

(b) Spin crossover behavior

The $\chi_M^{corr}T$ value for **Complex 8,** similarly calculated as previously done from its proposed chemical formula (FW = 1419.90 g mol^{-1}), χ_g (2.06 x 10^{-6} cm^3 g^{-1}), χ_M (2.92 x 10^{-3} cm^3 mol^{-1}), χ_{dia} (-1815.96 x 10^{-6} cm^3 mol^{-1}) and χ_M^{corr} (4.74 x 10^{-3} cm^3 mol^{-1}), was 1.39 cm^3 mol^{-1} K at 293 K. Thus, **Complex 8** was made up of 67.6% HS and 32.4% LS Co(II) at room temperature. Hence, similar to **Complex 7**, the lower percentage of HS Co(II) of this complex compared to **Complex 6** ($[Co(L^{16})_2](BF_4)_2.H2O$; 100% HS) arose from the bigger ClO_4^- ion.

Its **temperature-dependence ε_{max}** were similarly recorded as for **Complex 7**. The results (**Figure 4.54**) show almost similar behavior as **Complex 7**, and may be similarly explained.

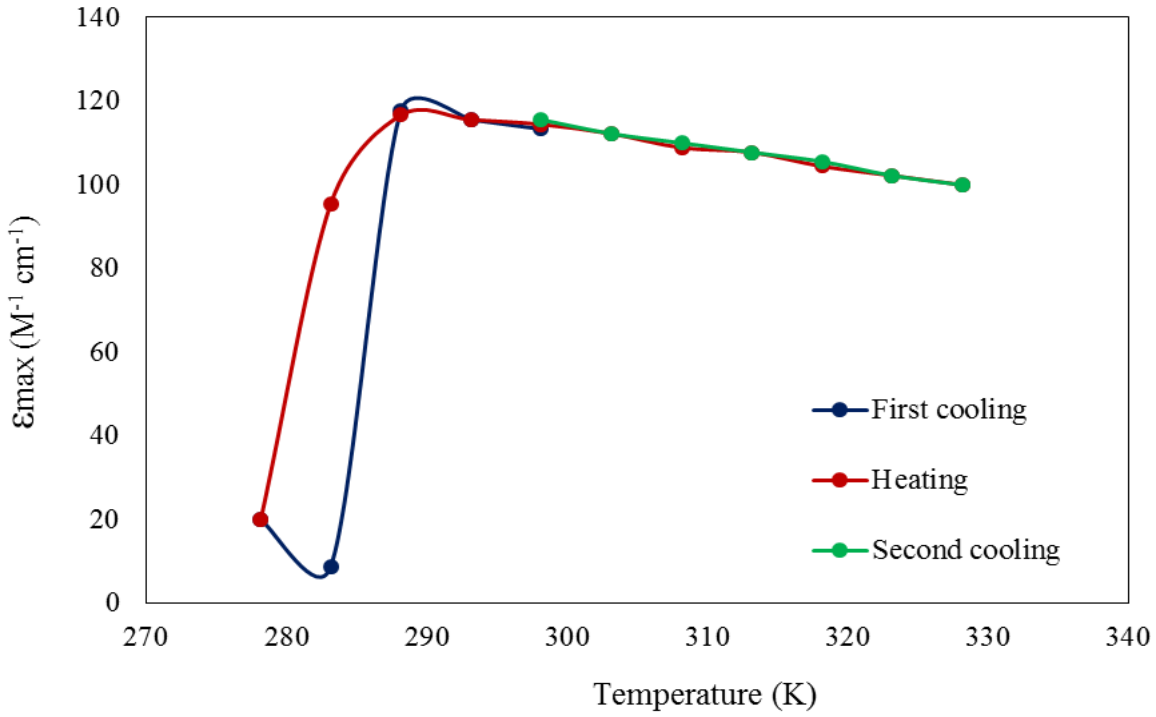

Figure 4.54 Temperature dependence of ε_{max} for **Complex 8** at 790 nm

(c) Thermal properties

The **TGA** trace of **Complex 8** (**Figure 4.55**) shows almost similar thermal behavior as **Complex 7**. The complex suffered a total weight loss of 91.3% in the temperature range 235 - 734 °C due to loss of eight O_2 molecules and two L^{16} ligands (expected, 90.9%). The amount of residue at temperatures above 734 °C was 8.7%, which is in good agreement with the expected amount of 9.0% (assuming pure $CoCl_2$). Its decomposition temperature was almost similar to **Complex 6** ($[Co(L^{16})_2](BF_4)_2.H_2O$, T_{dec} = 231 °C), which further enhanced the above proposal that anionic size has no effect on the thermal stabilities of these complexes.

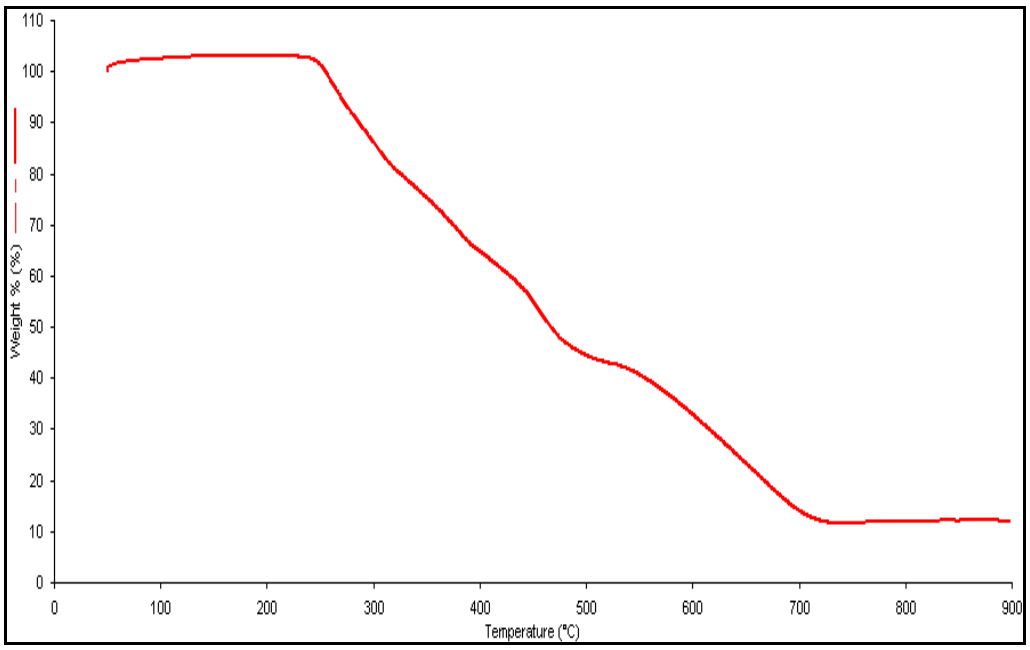

Figure 4.55 TGA of **Complex 8**

Its **DSC** scans (**Figure 4.56**) were similarly recorded for two heating-and-cooling cycles. The data and assignment were collected in **Table 4.15**.

Table 4.15 DSC data for **Complex 8**

Cycle		**Temperature (˚C)**	**ΔH (kJ mol^{-1})**	**Assignment**
1	Heating	88.7	+80.7	Melting temperature
	Cooling	45.0	-21.8	Cr-Cr transition
2	Heating	50.7	+21.0	Cr-Cr transition
		85.0	+62.2	Melting temperature
	Cooling	-	-	-

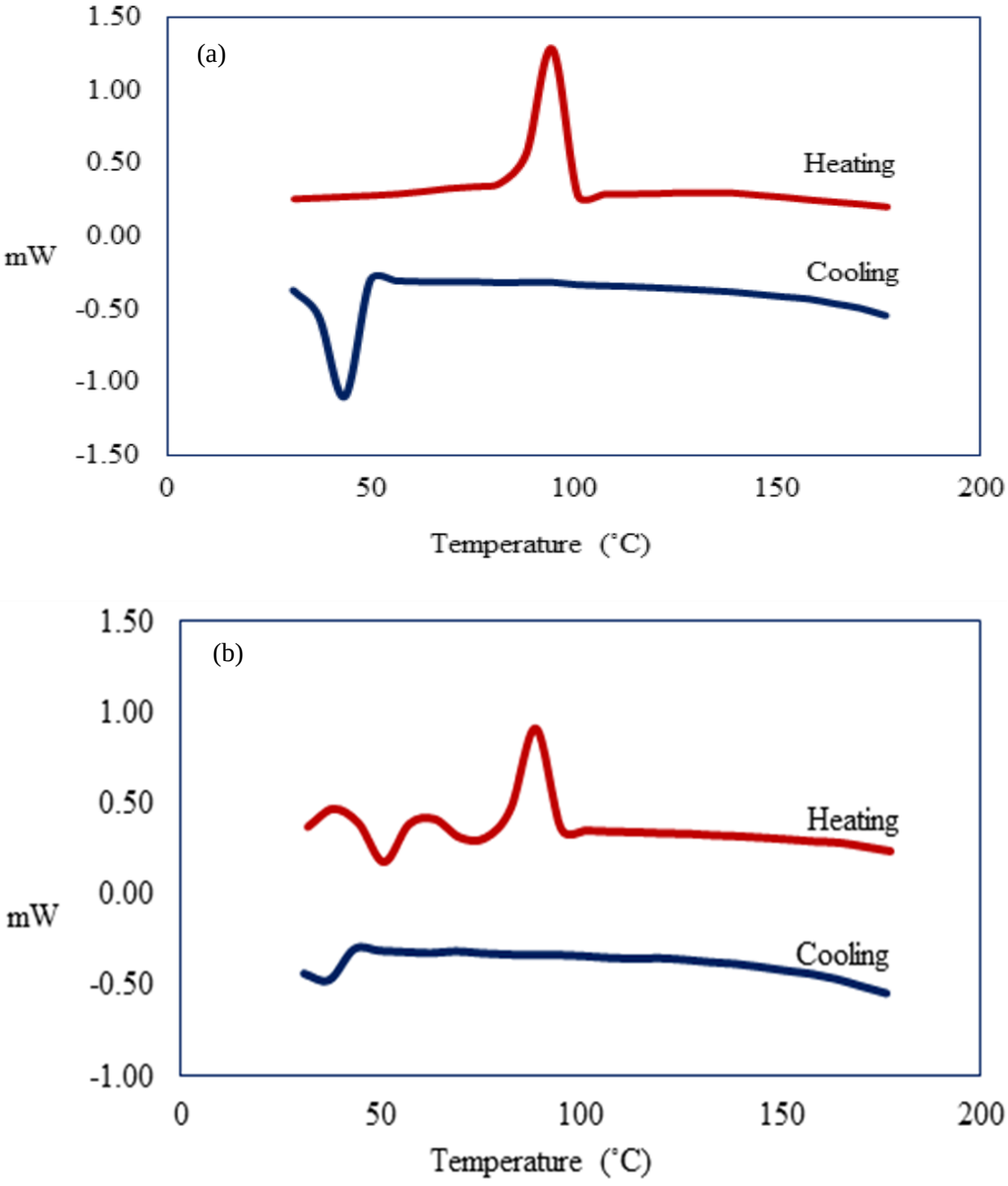

Figure 4.56 DSC of **Complex 8**: (a) first cycle; (b) second cycle. Endothermic peak up

Viewed under **POM**, **Complex 8** was observed to melt at about 86 °C and to clear to an isotropic liquid at 178 °C. However, on cooling from the isotropic liquid phase, no optical textures were observed. Hence, as for **Complex 7**, this complex also did not exhibit any mesomorphic properties. This is in contrast to the corresponding **Complex 6 ($[Co(L^{16})_2](BF_4)_2.H_2O$)**.

4.3.3 Summary

Summary of results for **Complexes 7** and **8** are collected in **Table 4.16**. Several general points for both complexes: (a) octahedral; (b) made up of HS Co(II) and LS Co(II) at 298 K; (c) decomposed at about 240 °C; and (d) did not exhibit liquid crystal properties.

Table 4.16 Summary for **Complex 7** in comparison with **Complex 8**

Complex	**7**	**8**
Structural formula	$[Co(L^{12})_2](ClO_4)_2$	$[Co(L^{16})_2](ClO_4)_2$
λ_{max}/nm (ε_{max}/M^{-1} cm^{-1})	770 (190), 643 (365)	820 (105), 650 (248)
T_{dec}/°C	245	235
$\chi_M T$ (cm^3 K mol^{-1})	1.07 (46.3% HS; 53.7% LS)	1.39 (67.6% HS; 32.4% LS)
Liquid crystal properties	Not mesogenic	Not mesogenic

4.4 $Co(L^6)_2]X_2$

The third phase of this project was to compare the effect of larger anions (PF_6^- ions) than BF_4^- ion, on the structure, spin crossover behavior and thermal properties of $[Co(L^6)_2]^{2+}$ ions.

4.4.1 $[Co(L^6)_2](PF_6)_2$

NH_4PF_6, $CoCl_2.4H_2O$, 2,6-pyridinedicarboxaldehyde and 1-aminohexane reacted in methanol to form a red-brick powder (**Complex 9**) in good yield (79.1%). The powder was readily soluble in solvents similar to **Complexes 1-8**.

(a) Deduction of structural formula

Based on the same instrumental analyses as previously discussed, it is proposed that the structure of **Complex 9** was similar to that of previously discussed complexes.

The results of **elemental analyses** for carbon, hydrogen and nitrogen (**Table 4.17**) are in excellent agreement with those calculated for chemical formula $[Co(L^6)_2](PF_6)_2$ ($C_{38}H_{62}CoF_{12}N_6P_2$, formula weight 951.80 g mol^{-1}).

Table 4.17 Elemental analytical data for **Complex 9**

Element	(%)	
	Calculated	**Found**
Carbon	47.95	47.50
Hydrogen	6.57	6.55
Nitrogen	8.83	8.85

Its **ESI-MS** spectrum (**Figure 4.57**) shows peaks at m/z 806.4 for $\{[Co(L^5)_2](PF_6)\}^+$ ion (calculated, 806.4) and m/z 331.2 for $[Co(L^5)_2]^{2+}$ ion (calculated, 330.7).

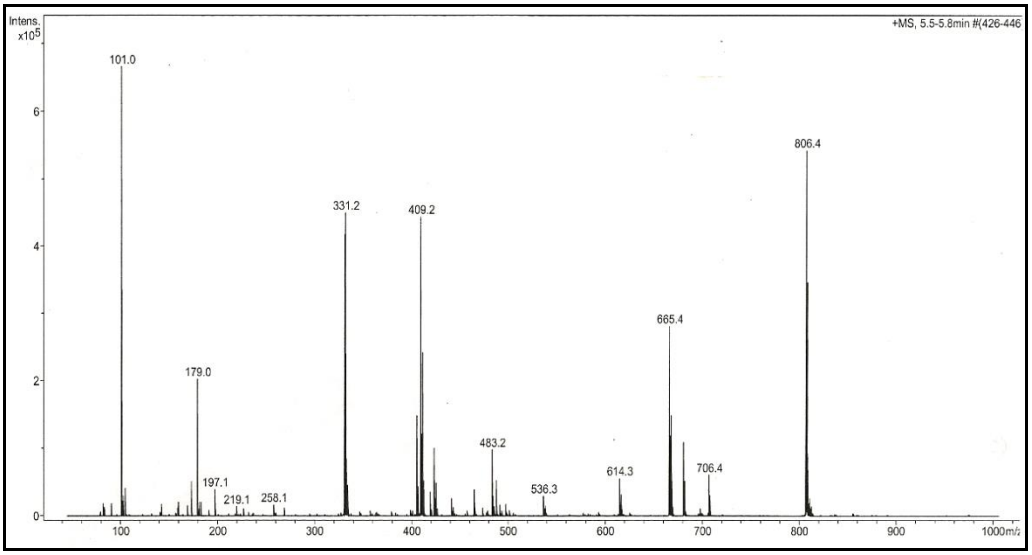

Figure 4.57 ESI-MS of **Complex 9**

Its **FTIR** spectrum (**Figure 4.57**) shows peaks at 2935 cm^{-1}, 2872 cm^{-1} and 1593 cm^{-1}. These may be similarly assigned as for **Complex 1**. Additionally, there is a strong peak at 837 cm^{-1} for PF_6^- ion [13].

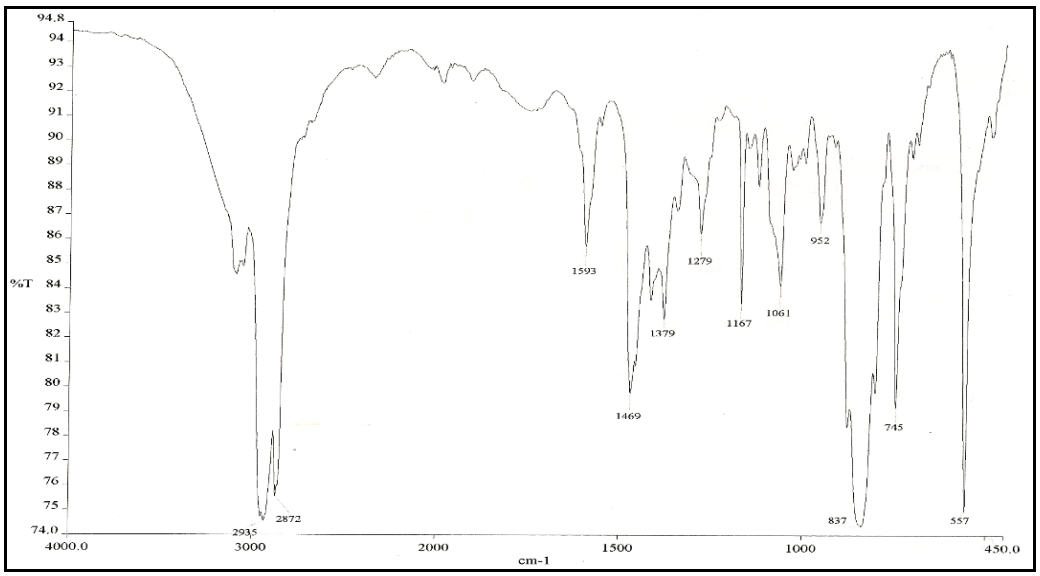

Figure 4.58 FTIR spectrum of **Complex 9**

Its **UV-vis** spectrum in CH_3Cl (**Figure 4.59**) shows broad *d-d* bands at 835 nm (ε, 118 M^{-1} cm^{-1}), 643 nm (ε, 162 M^{-1} cm^{-1}) and 473 nm (ε, 654 M^{-1} cm^{-1}). These electronic transitions may be similarly assigned as for **Complex 1**.

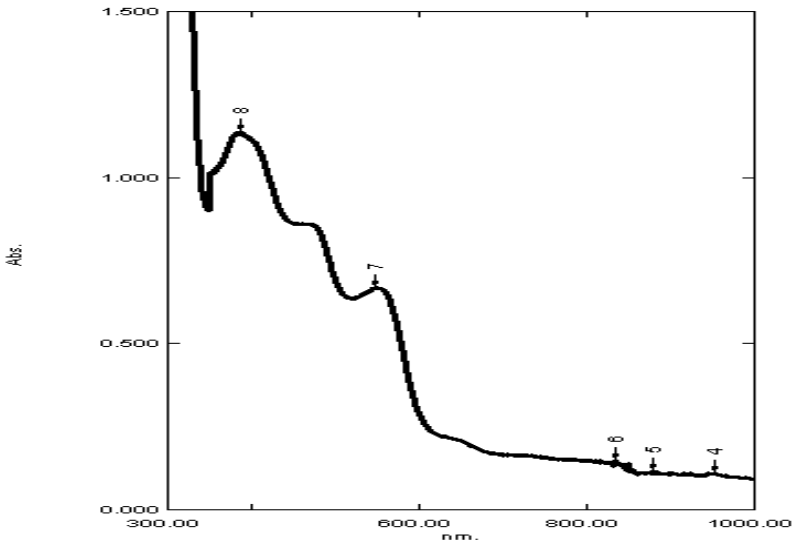

Figure 4.59 UV-visible spectrum of **Complex 9**

(b) Spin crossover behavior

The value $\boldsymbol{\chi_M^{corr}T}$ of **Complex 9**, calculated from its proposed chemical formula (FW = 951.80g mol^{-1}), χ_g (1.73 x 10^{-6} cm^3 g^{-1}), χ_M (1.65 x 10^{-3} cm^3 mol^{-1}), χ_{dia} (-504.88 x 10^{-6} cm^3 mol^{-1}) and χ_M^{corr} (2.15 x 10^{-3} cm^3 mol^{-1}), was 0.63 cm^3 K mol^{-1}

at 293 K. Thus, **Complex 9** was made up of 17.1% HS and 82.9% LS Co(II) at room temperature. Hence, it has a lower percentage of HS Co(II) compared to **Complex 1** (41% HS Co(II); 59% LS Co(II)). This is consistent with the larger size for PF_6^- ion, as proposed previously.

Its **temperature-dependence ε_{max}** were measured in DMSO at 643 nm. The results (**Figure 4.60**) show that on cooling, the ε_{max} value remained almost unchanged at about 250 M^{-1} cm^{-1} on cooling from 298 to 293 K. Upon heating from this temperature, the ε_{max} values decreased very gradually to about 170 M^{-1} cm^{-1} at 343 K, and then increased very gradually back to about 230 M^{-1} cm^{-1} on cooling to 298 K. This means that the amount of HS and LS Co(II) in this complex remained almost unaffected in the temperature range of 293 – 343 K.

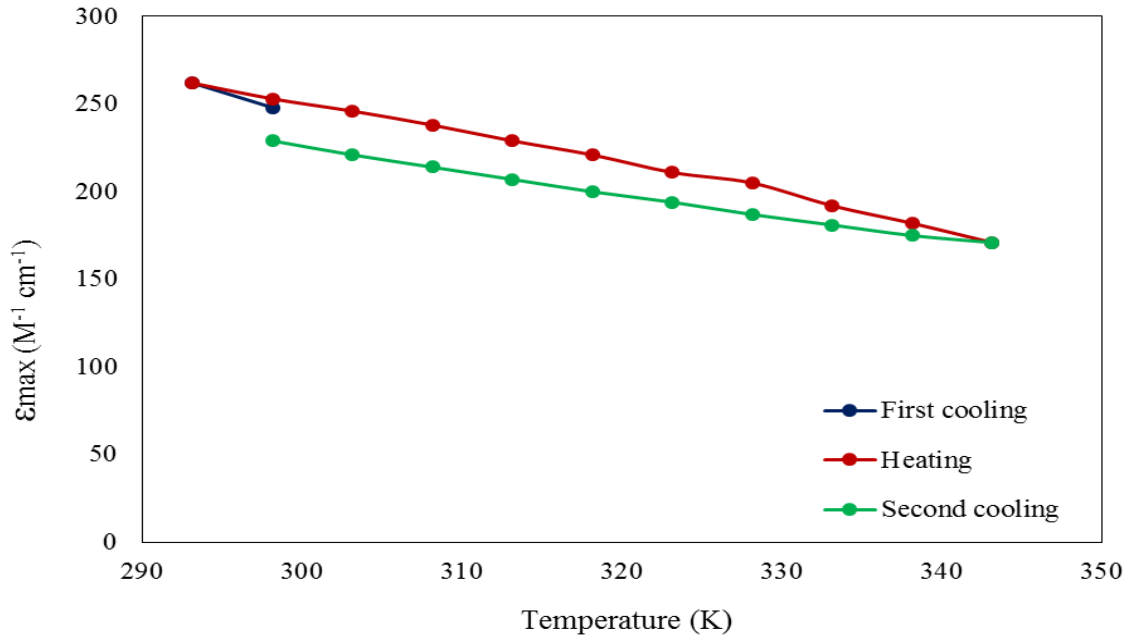

Figure 4.60 Temperature dependence of ε_{max} for **Complex 9** at 643 nm

(c) Thermal properties

The **TGA** trace of **Complex 9** (**Figure 4.61**) shows almost similar thermal behavior as for **Complex 1**. The complex suffered a total weight loss of 78.5% at 211 °C to 899 °C due to loss of one PF_5 molecule and two L^6 ligands (expected, 76.6%). The amount of residue at temperatures above 899 °C was 21.5%, which is in good agreement with the

expected amount of 23.4% (assuming mixture of one PF_5 molecule and CoF_2). Its decomposition temperature was almost similar to **Complex 1** (n = 6, T_{dec} = 261 °C). Hence, it was consistent with size of anion does not affect the decomposition temperature.

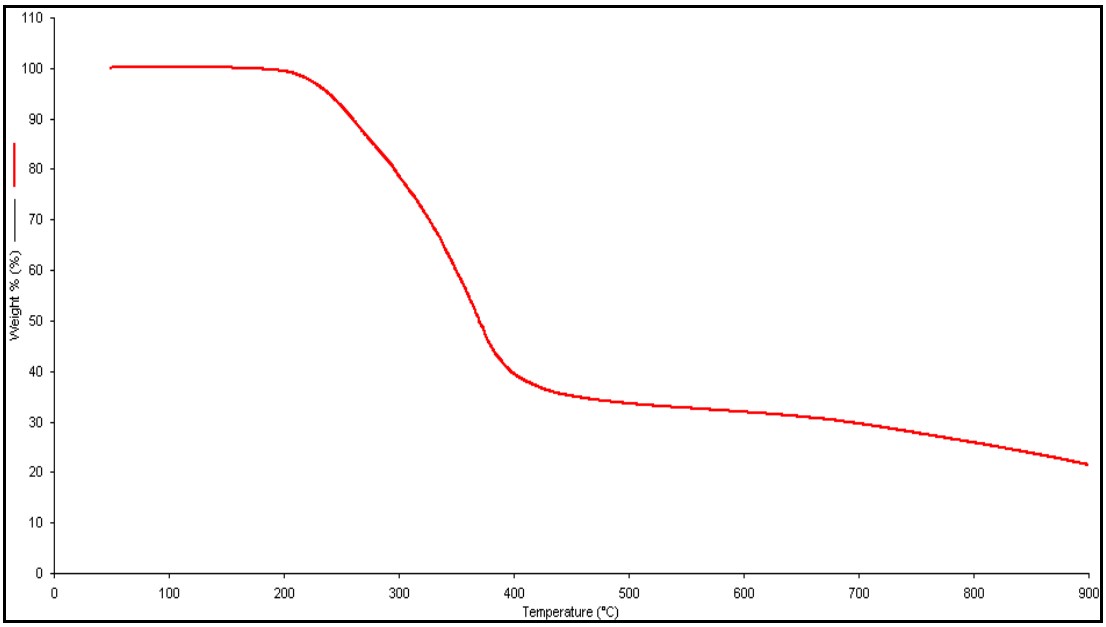

Figure 4.61 TGA trace of **Complex 9**

This complex did not exhibit any mesomorphic properties. Hence, its **DSC** data was not collected.

4.4.3 Summary

All experimental data for $[Co(L^6)_2]X_2$ in comparison with **Complex 1** are summarized in **Table 4.18**. Several general points are similar as previous discussed for **Complexes 7** and **8**: (a) both complexes were octahedral; (b) HS percentage were lowered by the larger size of anion (PF_6^-); (c) the decomposition temperatures were not affected by the size of anion; and (d) complexes with short alkyl chain length (n = 6) do not exhibit liquid crystal properties.

Table 4.18 Summary for **Complex 9** in comparison with **Complex 1**

Complex	**1**	**9**
Structural formula	$[Co(L^6)_2](BF_4)_2.½H_2O$	$Co(L^6)_2(PF_6)_2$
λ_{max}/nm (ε_{max}/M^{-1} cm^{-1})	650 (267), 545 (921)	835 (118), 643 (162), 473 (654)
T_{dec}/°C	97	211
$\chi_M T$ (cm^3 K mol^{-1})	0.99 (41.0% HS; 59.0% LS)	0.63 (17.1% HS; 82.9% LS)
Liquid crystal properties	Not mesogenic	Not mesogenic

4.5 $[Fe(L^n)_2](BF_4)_2$

The next phase of this research was to replace Co(II) with Fe(II) for M in $[M(L^n)_2](BF_4)_2$, where n = 6, 12, 16. The main objectives were to compare the effect of the different metal(II) ion the spin-crossover behavior and thermal properties of these structurally similar complexes.

Fe(II) ion was chosen because its valence electronic configuration in the LS state is t_{2g}^6 (no unpaired electron, diamagnetic), while in the HS state is t_{2g}^4 e_g^2 (4 unpaired electrons, paramagnetic), making it easy to state the spin state visually from the colors of its complexes (LS is purple, HS is colorless) or using simple instrumental techniques, such as electronic spectroscopy and magnetic susceptibility. However, more important factors are stronger Fe(II)-L bond compared to Co(II)-L bond as a result of insignificant Jahn-Teller (J-T) distortion for the former (especially LS complexes), and abrupt SCO due to the large entropy change in Fe(II) complexes (ΔS = 13.38 J $mol^{-1}K^{-1}$) compared to Co(II) complexes (ΔS = 5.76 J mol^{-1} K^{-1}), calculated from the relationship: ($\Delta S = 8.315 \{\ln[(2S+1)_{HS} - (2S+1)]_{LS}\}$[14].

4.5.1 $[Fe(L^6)_2](BF_4)_2$

2,6-Pyridinedicarboxaldehyde, 1-aminohexane and $Fe(BF_4)_2.6H_2O$ reacted in methanol to form a dark purple powder (**Complex 10**) in good yield (82.7%). The powder was readily soluble in solvents similar to previously discussed Co(II) complexes.

(a) Deduction of structural formula

Based on the same instrumental analyses, it is proposed that the structure of **Complex 10** was similar to those of previously discussed Co(II) complexes.

The results of **elemental analyses** for carbon, hydrogen and nitrogen (**Table 4.19**) are in excellent agreement with those calculated for chemical formula $[Fe(L^6)_2](BF_4)_2$ ($C_{38}H_{62}B_2FeF_8N_6$; formula weight 831.50 g mol^{-1}).

Table 4.19 Elemental analytical data for **Complex 10**

Element	**(%)**	
	Calculated	**Found**
Carbon	54.83	53.60
Hydrogen	7.51	7.35
Nitrogen	10.10	10.45

Its **ESI-MS** spectrum (**Figure 4.62**) shows peaks at m/z 757.4 for $\{[Co(L^6)_2](BF_4)\}^+$ ion (calculated, 757.4) and 329.7 for $[Co(L^6)_2]^{2+}$ ion (calculated, 329.2).

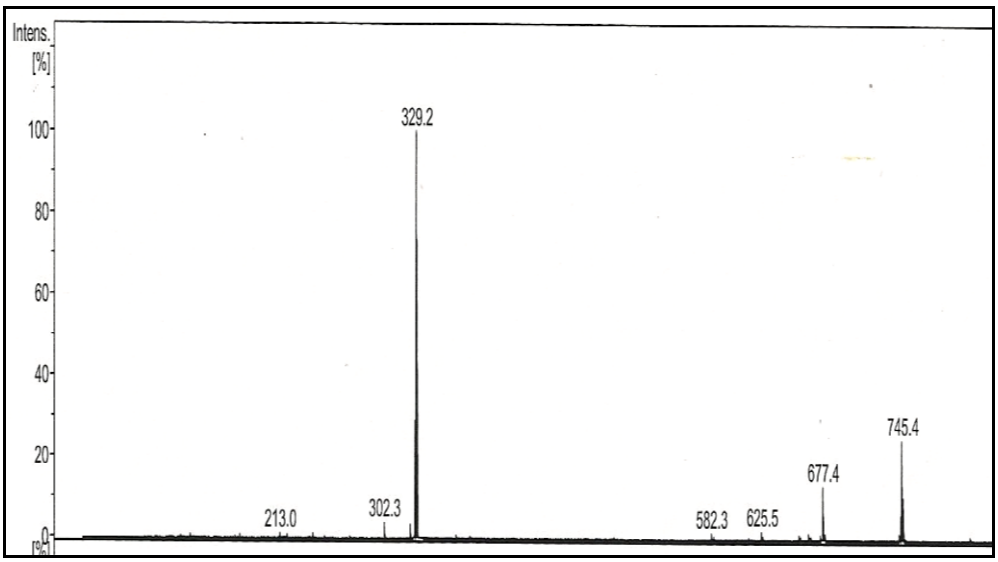

Figure 4.62 ESI-MS spectrum of **Complex 10**

Its **FTIR** spectrum (**Figure 4.63**) shows peaks at 2925 cm^{-1}, 2871 cm^{-1}, 1533 cm^{-1} and 1049 cm^{-1}. These peaks may be similarly assigned as for **Complexes 4** $[Co(L^{12})_2](BF_4)_2$, **5** $[Co(L^{14})_2](BF_4)_2$, and **6** $[Co(L^{16})_2](BF_4)_2$.

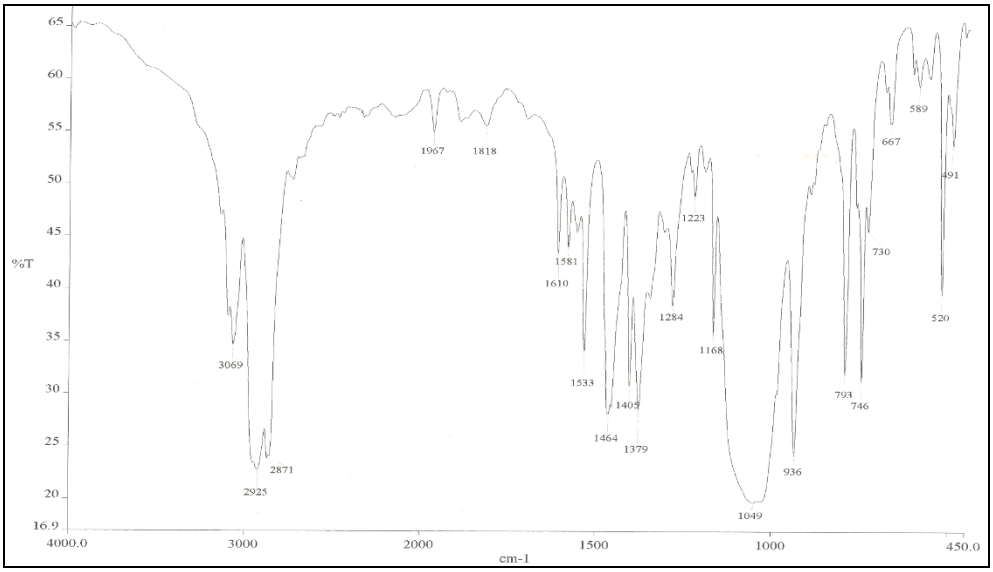

Figure 4.63 FTIR spectrum of **Complex 10**

Its **UV-visible** spectrum in CH_3Cl (**Figure 4.64**) shows a broad *d-d* band at 721 nm (ε, 560 M^{-1} cm^{-1}) and three MLCT bands at 597 nm (ε, 10210 M^{-1} cm^{-1}), 573 nm (ε, 8230 M^{-1} cm^{-1}) and 473 nm (ε, 7570 M^{-1} cm^{-1}). The *d-d* band suggests an octahedral LS complex. Accordingly, the broad *d-d* is assigned to overlapping $^1A_{1g} \rightarrow {}^1T_{1g}$ and $^1A_1 \rightarrow {}^1T_{2g}$ electronic transitions [15].

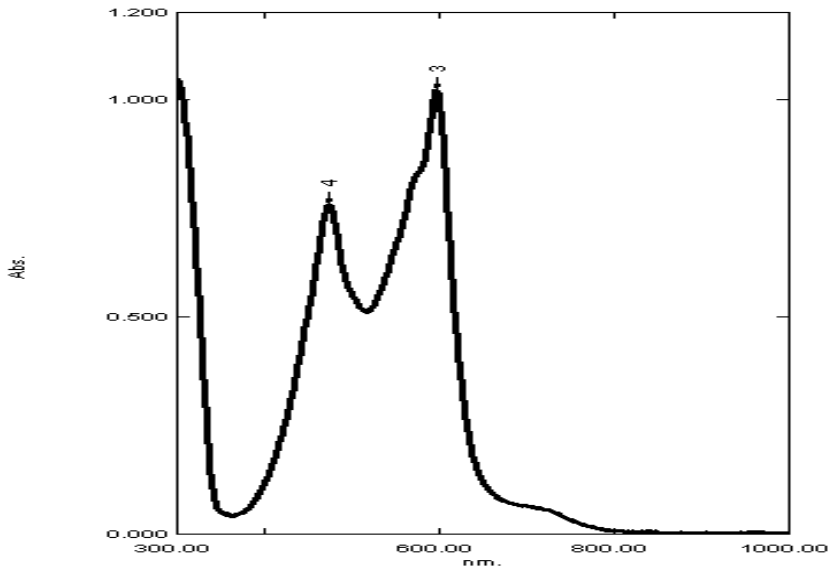

Figure 4.64 UV-visible spectrum of **Complex 10**

(b) Spin-crossover behavior

The $\chi_M^{corr}T$ value for **Complex 10**, calculated from its proposed chemical formula (FW = 831.50 g mol^{-1}), χ_g (1.60 x 10^{-7} cm^3 g^{-1}), χ_M (1.33x 10^{-4} cm^3 mol^{-1}), χ_{dia} (-441.88 x 10^{-6} cm^3 mol^{-1}) and χ_M^{corr} (5.75 x 10^{-4} cm^3 mol^{-1}), was 0.17 cm^3 K mol^{-1} at 298 K. The theoretical value is 3.00 cm^3 K mol^{-1} for a HS Fe(II) complex (S = 2), and 0 cm^3 K mol^{-1} for a LS Fe(II) complex (S = 0) [5]. From this, it may be inferred that this complex was made up of 5.6% HS and 94.4% LS Fe(II) at this temperature. Hence, the Fe(II) complex was mainly LS at room temperature compared to **Complex 1** ($[Co(L^6)_2)](BF_4)_2.½H_2O$; 41% HS, 59% LS). The result is consistent with the insignificant J-T effect for Fe(II).

Its **temperature-dependence** ε_{max} values were similarly measured as for previous complexes. The results (**Figure 4.65**) show that on cooling, the ε_{max} values remained almost unchanged at about 580 M^{-1} cm^{-1} from 298 K to 288 K, and then decreased abruptly to about 280 M^{-1} cm^{-1} (or the presence of 45.6% LS Fe(II)) at 278 K. Upon heating from this temperature, the values initially remained unchanged at 280 M^{-1} $cm^{-1,}$ then increased abruptly back to about 580 M^{-1} cm^{-1} at 298 K, and then

remained almost unchanged on further heating to 328 K followed by cooling back to 298 K. From these results, it may be inferred that **Complex 10** showed a reverse (LS-to-HS transition on cooling; HS-to-LS transition on heating) and reversible SCO behavior in solution.

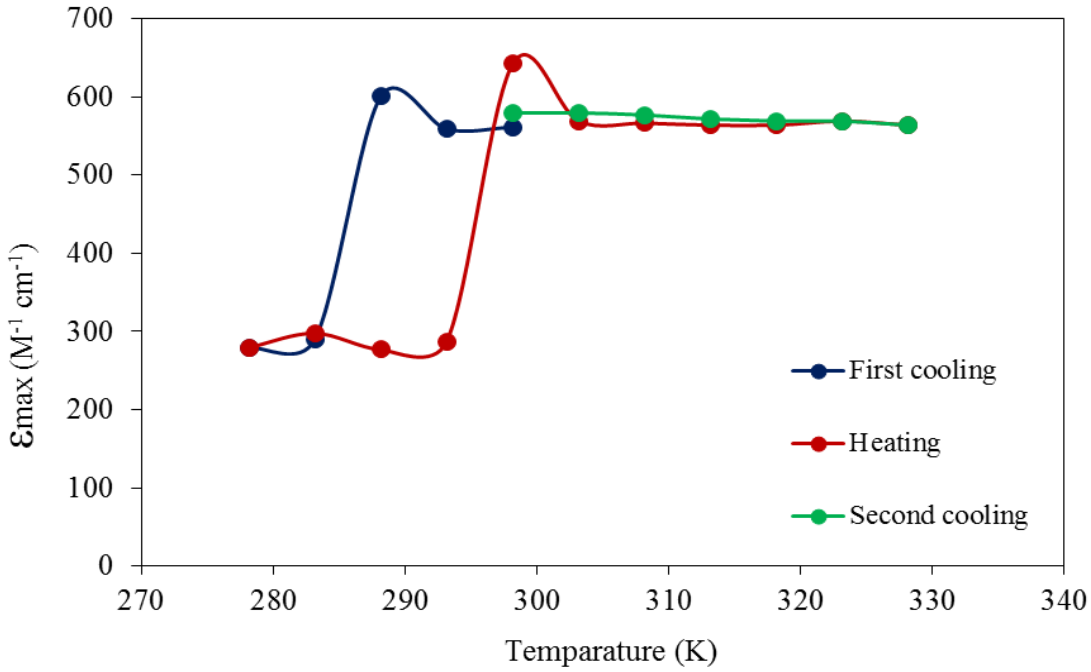

Figure 4.65 Temperature-dependence of ε_{max} values for **Complex 10** at 722 nm

(c) Thermal and mesomorphic properties

The **TGA** trace of **Complex 10** (**Figure 4.66**) shows almost similar thermal behavior as **Complex 1**. It suffered a total weight loss of 88.3% in the temperature range 225 - 761 °C due to loss of two BF_3 molecules and two L^6 ligands (expected, 88.7%). The amount of residue at temperatures above 761 °C was 11.7%, which is in good agreement with the expected amount of 11.3% (assuming pure FeF_2). Hence, its decomposition temperature was significantly higher than **Complex 1** (**[**$[Co(L^6)_2)](BF_4)_2.½H_2O$; T_{dec} = 97 °C). Two possible reasons were absence of lattice H_2O and stronger Fe-L bonds for **Complex 10**.

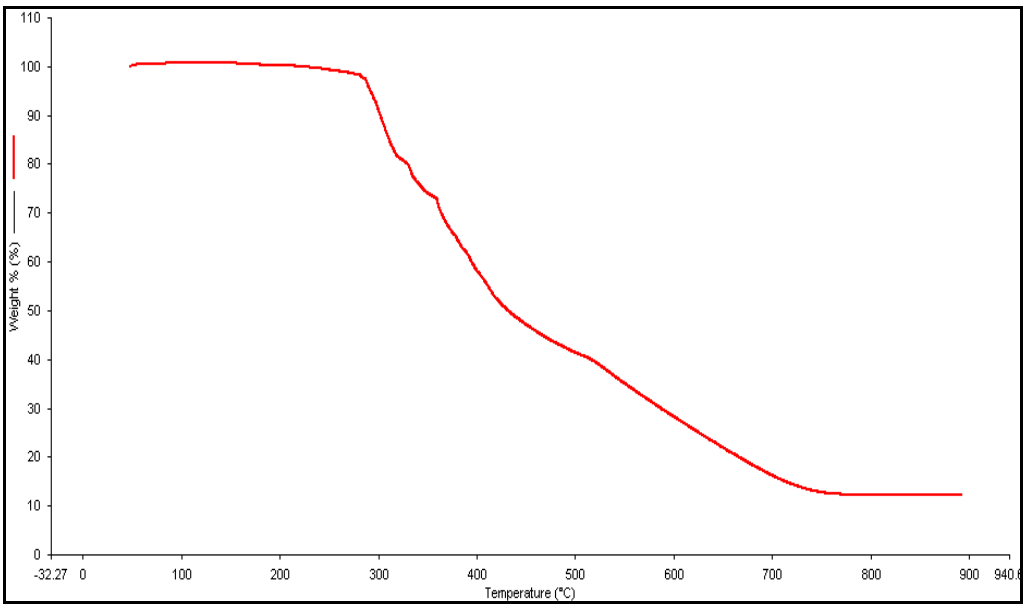

Figure 4.66 TGA trace of **Complex 10**

Its **DSC** scan (**Figure 4.67a** and **4.67b**) was performed on two heating-cooling cycles, in the temperature range from 25 – 200 °C. The data and assignment were collected in **Table 4.20**.

Table 4.20 DSC data for **Complex 10**

Cycle		**T (˚C)**	**ΔH (kJ mol^{-1})**	**Assignment**
1	Heating	36.7	+4.7	Cr-Cr transition
		146.8	+32.6	Cr-Col$_h$ transition
	Cooling	-	-	-
2	Heating	42.4	+3.1	Cr-Cr transition
		120.1	+0.9	Cr-Cr transition
		156.1	+14.3	Cr-Cr transition
	Cooling	-	-	-

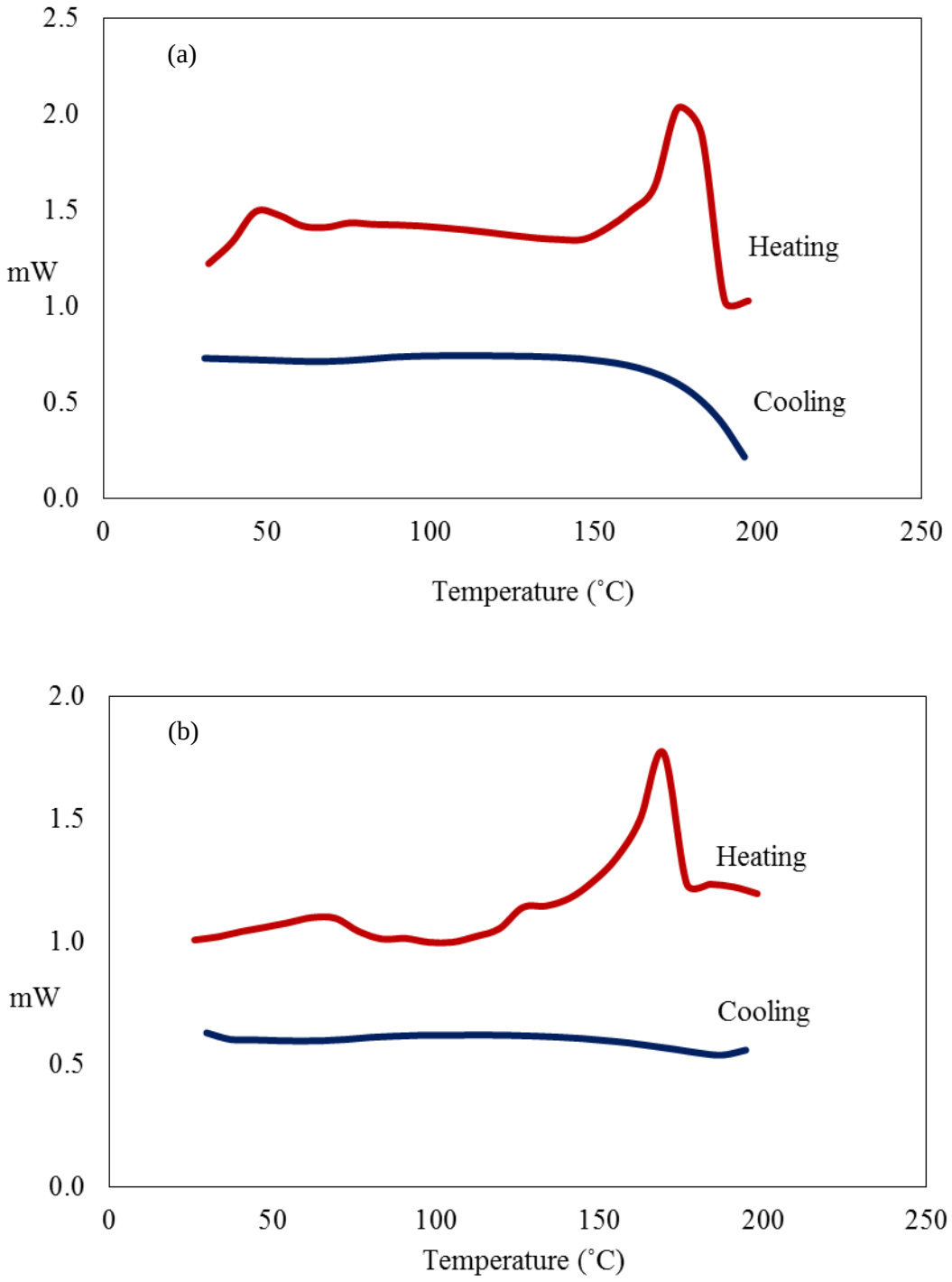

Figure 4.67 DSC of **Complex 10**: (a) first cycle; (b) second cycle. Endothermic peak up

Viewed under **POM**, **Complex 10** was observed to melt at about 146 °C and to clear to an isotropic liquid at 180°C. On cooling from the isotropic liquid, it developed a fern-like texture at 154 °C, corresponding to the formation of a columnar mesophase (**Figure 4.68**) [16]. Hence, this complex has mesomorphic properties of a discotic mesogen.

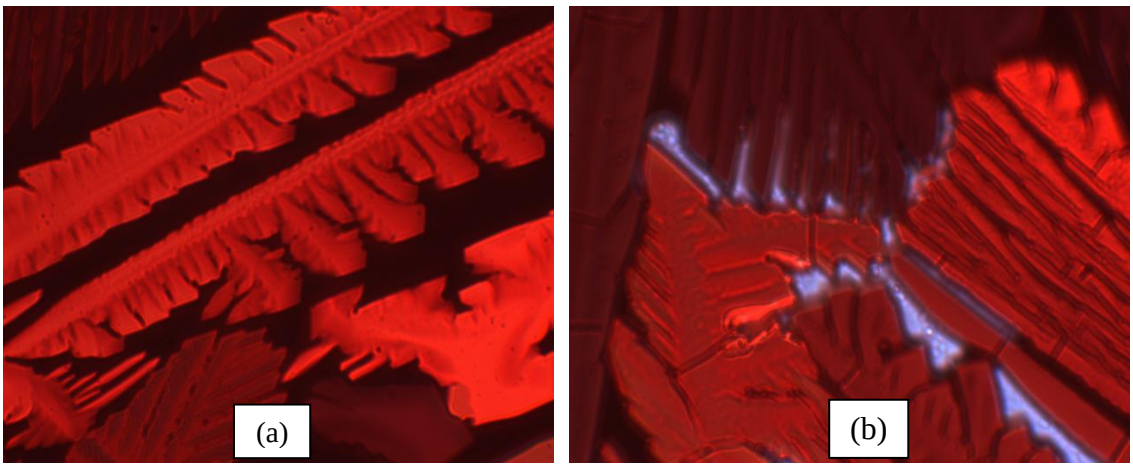

Figure 4.68 Photomicrographsof **Complex 10** on cooling at:(a) 154 ^{o}C; and (b) 44 ^{o}C

4.5.2 $[Fe(L^{12})_2](BF_4)_2.H_2O$

2,6-Pyridinedicarboxaldehyde, 1-aminododecane and $Fe(BF_4)_2.6H_2O$ reacted in methanol to form a dark purple powder (**Complex 11**) in good yield (78.4%). The powder was readily soluble in solvents similar to previously discussed complexes.

(a) Deduction of structural formula

Based on the same instrumental analyses, it is proposed that the structure of **Complex 11** was similar to those of previously discussed complexes.

The results of **elemental analyses** for carbon, hydrogen and nitrogen (**Table 4.21**) are in excellent agreement with those calculated for chemical formula $[Fe(L^{12})_2](BF_4)_2.H_2O$ ($C_{62}H_{112}B_2FeF_8N_6O$; formula weight 1187.03 g mol^{-1}).

Table 4.21 Elemental analytical data for **Complex 11**

Element	**(%)**	
	Calculated	**Found**
Carbon	62.73	62.35
Hydrogen	9.51	9.97
Nitrogen	7.08	7.04

Its **FTIR** spectrum (**Figure 4.69**) shows strong peaks at 2916 cm^{-1}, 2845 cm^{-1} and 1154 cm^{-1} which may be similarly assigned as for previously discussed complexes.

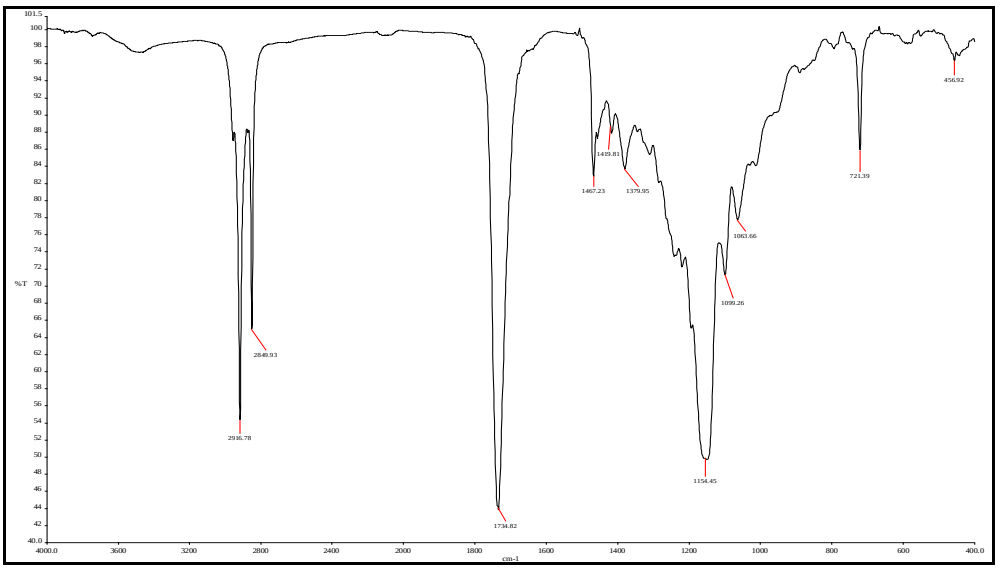

Figure 4.69 FTIR spectrum of **Complex 11**

Its **UV-visible** spectrum in CH_3Cl (**Figure 4.70**) shows a broad *d-d* band at 721 nm (ε, 510 M^{-1} cm^{-1}) and CT bands at 599 nm (ε, 9444 M^{-1} cm^{-1}), 573 nm (ε, 7610 M^{-1} cm^{-1}) and 472 nm (ε, 7083 M^{-1} cm^{-1}). These electronic transitions may be similarly assigned as for **Complex 10** ($[Fe(L^6)_2)](BF_4)_2$).

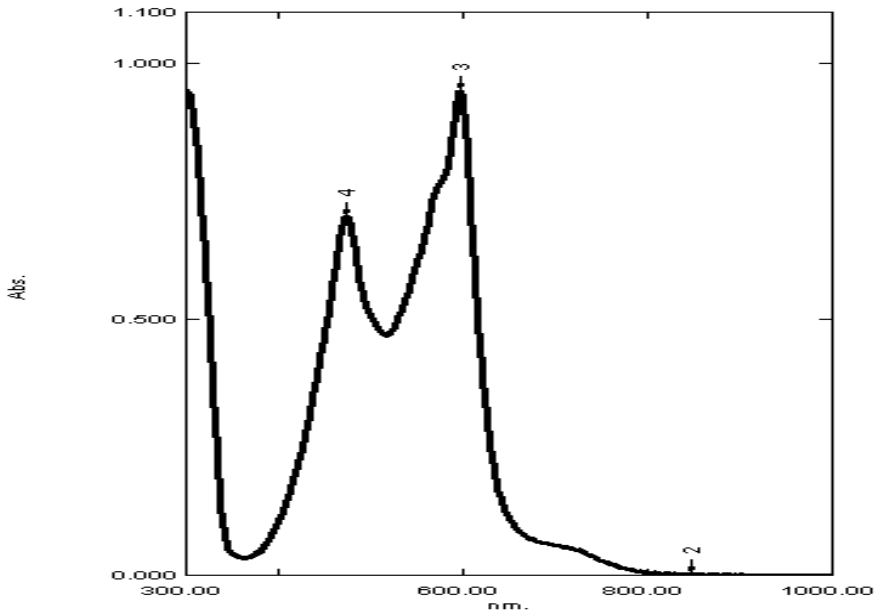

Figure 4.70 UV-visible spectrum of **Complex 11**

(b) Spin-crossover behavior

The $\chi_M^{corr}T$ value for **Complex 11**, calculated from its proposed chemical formula (FW = 1187.03 g mol^{-1}), χ_g (2.40 x 10^{-7} cm^3 g^{-1}), χ_M (2.85 x 10^{-4} cm^3 mol^{-1}), χ_{dia} (-739.52 x 10^{-6} cm^3 mol^{-1}) and χ_M^{corr} (1.02 x 10^{-3} cm^3 mol^{-1}), was 0.31 cm^3 K mol^{-1} at 298 K. Thus, **Complex 11** was made up of 10.3% HS and 89.7% LS Fe(II) at this temperature. These are similar to **Complex 10** ($[Fe(L^6)_2](BF_4)_2$; 5.6% HS, 94.4% LS), and may be similarly explained.

Its **temperature-dependence ε_{max}** values were similarly measured as previous complexes. However, the results (**Figure 4.71**) show different behavior from **Complex 10** ($[Fe(L^6)_2](BF_4)_2$. During initial cooling, the ε_{max} values remained almost unchanged at about 510 M^{-1} cm^{-1} from 298 K to 288 K, then increased abruption to about 1096 M^{-1} cm^{-1} (or the presence of 22.1% LS Fe(II))at 283 K, and then decreased to 755 M^{-1} cm^{-1} at 278 K. Upon heating from this temperature, the values followed similar trend as initial cooling and remained unchanged at 400 M^{-1} cm^{-1} on further heating to 328 K followed by cooling back to 298 K. From these results, it may be inferred that **Complex 11** showed a normal and reversible SCO behavior in solution.

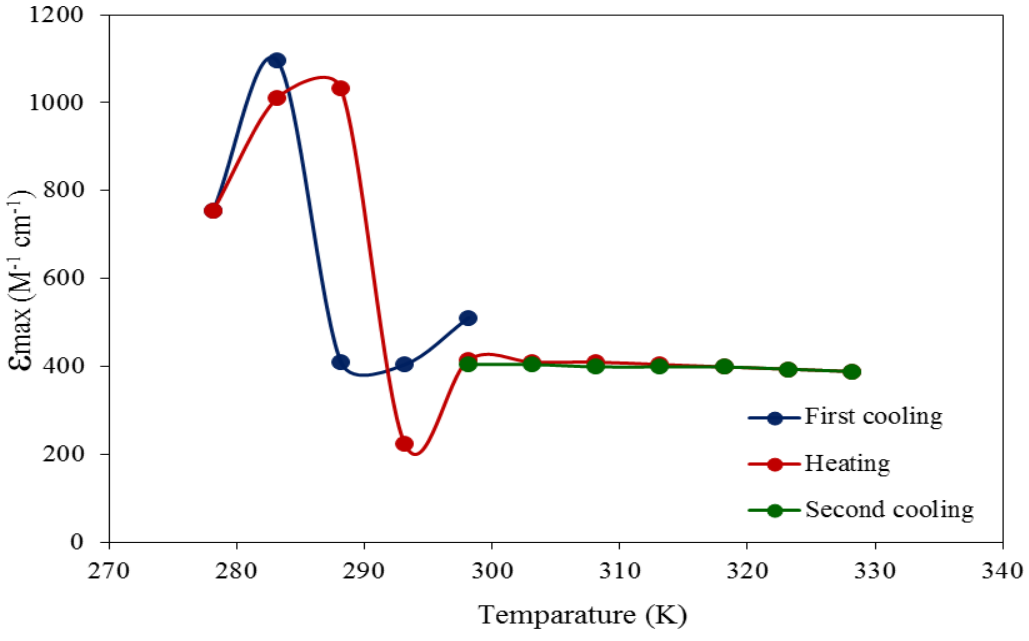

Figure 4.71 Temperature-dependence of ε_{max} values for **Complex 11** at 723 nm

(c) Thermal and mesomorphic properties

The **TGA** trace of **Complex 11** (**Figure 4.72**) The complex an initial weight loss of 0.8% from 84 °C to 240 °C due to loss of lattice H_2O (expected, 1.5%), followed by 91.4% in the temperature range 242 - 750 °C due to loss of two BF_3 molecules and two L^{12} ligands (expected, 90.6%). The amount of residue at temperatures above 750 °C was 7.8%, which is in good agreement with the expected amount of 7.9% (assuming pure FeF_2). Hence, its decomposition temperature was lower than **Complex 10** ($[Fe(L^6)_2](BF_4)_2$, T_{dec} = 275 °C), consistent with the presence of lattice water in **Complex 11** ($[Fe(L^{12})_2](BF_4)_2.H_2O$).

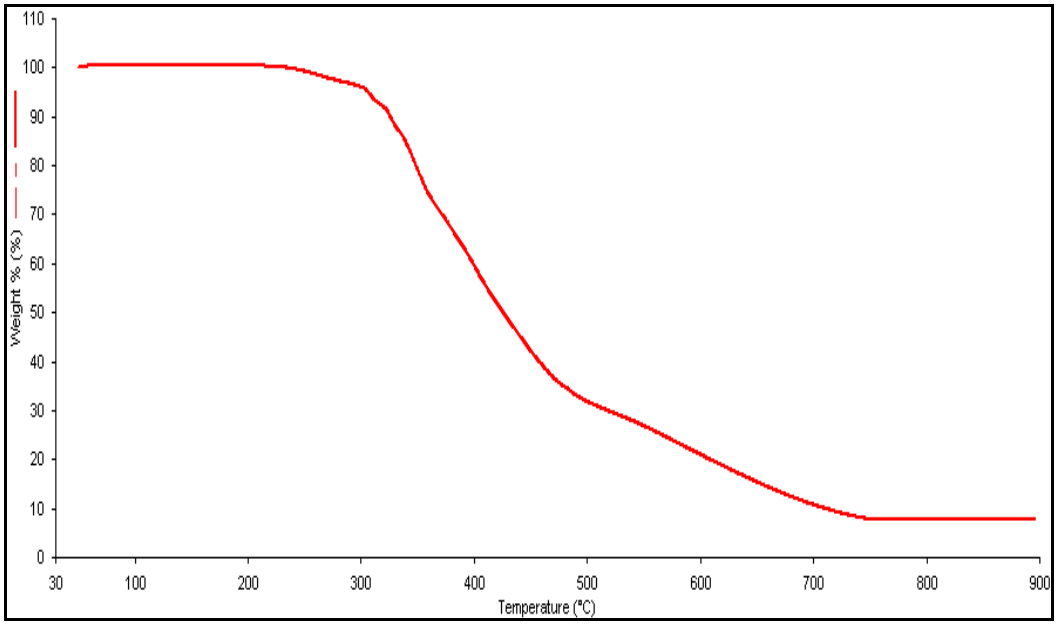

Figure 4.72 TGA of **Complex 11**

Its **DSC** scans (**Figure 4.73**), performed on one heating-cooling cycle in the temperature range of 25 – 200 °C, show a strong endothermic peak at 70.8 °C (ΔH = +65.1 kJ mol^{-1}) and a weaker endothermic peak at 111.2 °C (ΔH = +4.4 kJ mol^{-1}). These peaks maybe assigned as melting and clearing temperatures, respectively. However, no peaks were observed on cooling, indicating either very slow phase transitions or the sample had decomposed, as suggested earlier.

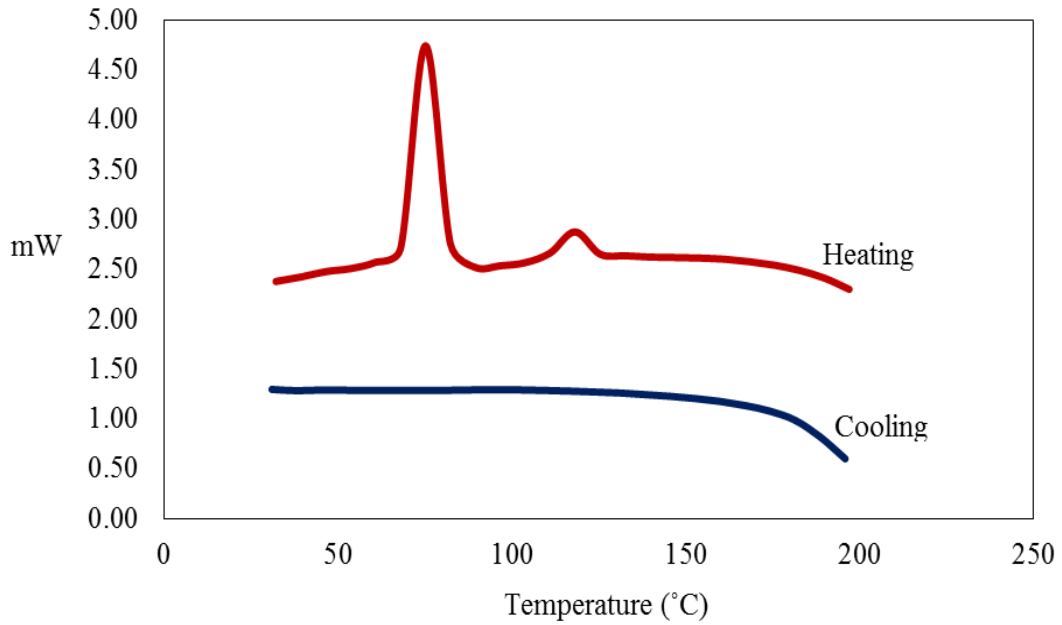

Figure 4.73 DSC of **Complex 11**. Endothermic peak up

Viewed under **POM**, **Complex 11** was observed to melt at about 70 °C and to clear at 129 °C. On cooling from the isotropic liquid, it developed dendritic-like textures at 125 °C which then transformed to mosaic textures at 111 °C (**Figure 4.74**). Similar texture was found for $(C_{16}H_{33}O)_8PcCo$ in Binnemans *et. al* [17]. Hence, as previous discussed complexes, this complex has liquid crystal properties of a *Col* mesogen.

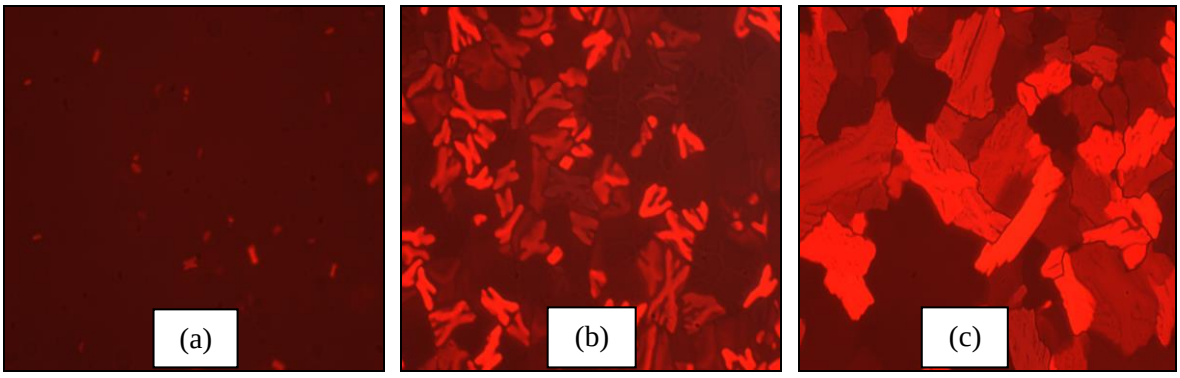

Figure 4.74 Photomicrographs of **Complex 11** at (a) 129°C, (b) 125 °C and (c) 111 °C

4.5.3 $[Fe(L^{16})_2](BF_4)_2$

2,6-Pyridinedicarboxaldehyde, 1-aminohexadecane and $Fe(BF_4)_2.6H_2O$ reacted in methanol to form a dark purple powder (**Complex 12**) in very good yield (93.2%). The powder was readily soluble in solvents similar to previously discussed complexes.

(a) Deduction of structural formula

Based on the same instrumental analyses as previously discussed, it is proposed that the structure of **Complex 12** was similar to that of previously discussed complexes.

The results of **elemental analyses** for carbon, hydrogen and nitrogen (**Table 4.22**) are in excellent agreement with those calculated for chemical formula $[Fe(L^{16})_2](BF_4)_2$ ($C_{78}H_{142}B_2FeF_8N_6$; formula weight 1393.46 g mol^{-1}).

Table 4.22 Elementalanalytical data for **Complex 12**

Element	**(%)**	
	Calculated	**Found**
Carbon	67.20	67.10
Hydrogen	10.27	11.43
Nitrogen	6.03	5.94

Its **FTIR** spectrum (**Figure 4.75**) shows peaks at 2917 cm^{-1}, 2850 cm^{-1}, 1468 cm^{-1} and 1054 cm^{-1}. These peaks may be similarly assigned as for **Complexes 10** ($[Fe(L^6)_2](BF_4)_2$ and **11** ($[Fe(L^{12})_2](BF_4)_2.H_2O$).

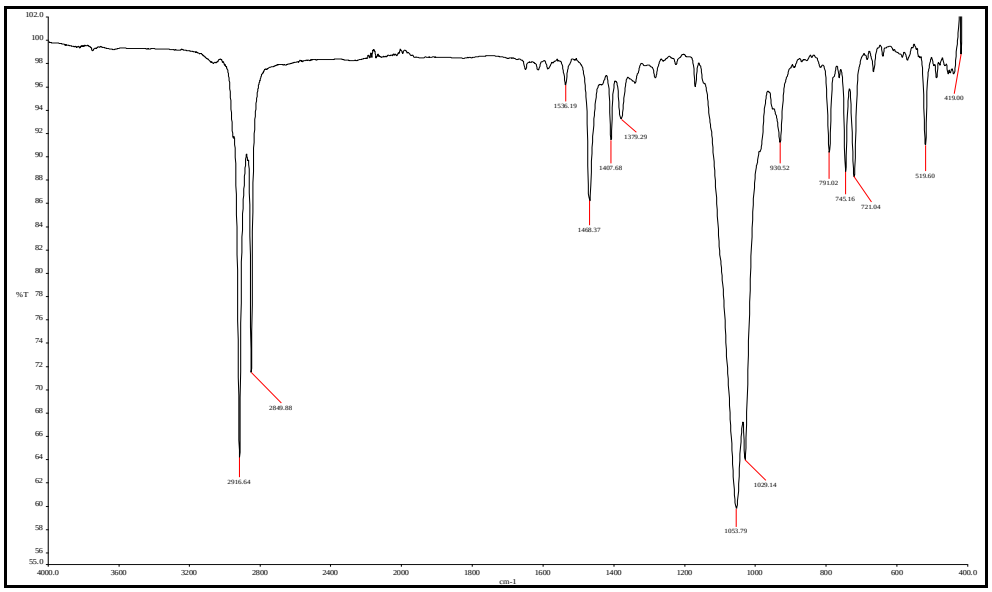

Figure 4.75 FTIR spectrum of **Complex 12**

Its **UV-visible** spectrum in CH_3Cl (**Figure 4.76**) shows broad *d-d* band at 721 nm (ε, 470 M^{-1} cm^{-1}), and CT bands 596 nm (ε, 8710 M^{-1} cm^{-1}), 576 nm (ε, 7100 M^{-1} cm^{-1}) and 473 nm (ε, 6475 M^{-1} cm^{-1}). These electronic transitions may be similarly assigned as for **Complexes 10** ($[Fe(L^6)_2](BF_4)_2$ and **11** ($[Fe(L^{12})_2](BF_4)_2.H_2O$).

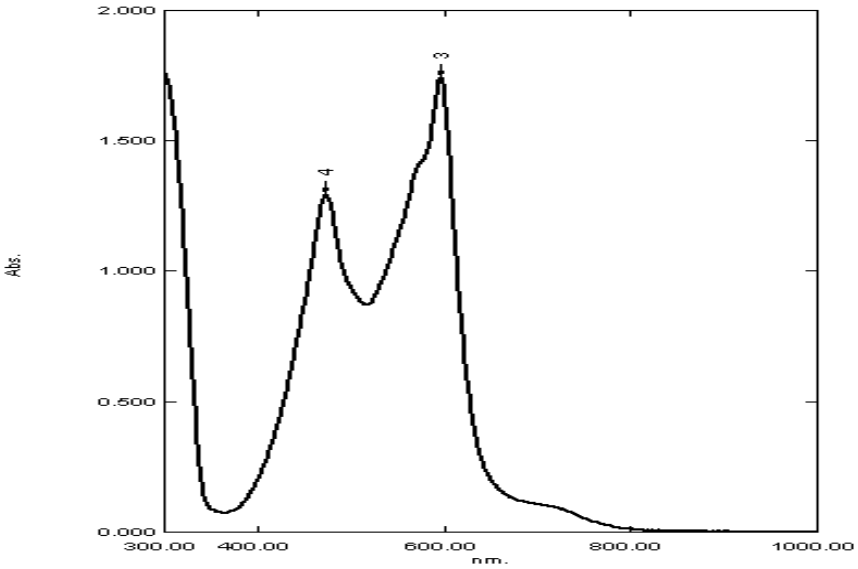

Figure 4.76 UV-visible spectrum of **Complex 12**

(b) Spin-crossover behavior

The $\chi_M^{corr}T$ value for **Complex 12**, calculated from its proposed chemical formula (FW = 1393.46 g mol^{-1}), χ_g (-0.16 x 10^{-7} cm^3 g^{-1}), χ_M (-2.23 x 10^{-5} cm^3 mol^{-1}), χ_{dia} (-916.28 x 10^{-6} cm^3 mol^{-1}) and χ_M^{corr} (8.94 x 10^{-4} cm^3 mol^{-1}), was 0.27 cm^3 K mol^{-1} at 298 K. Thus, **Complex 12** was made up of 9.0% HS and 91.0% LS Fe(II) at this temperature.

Its **temperature-dependence ε_{max}** values were similarly measured as previous complexes. The results (**Figure 4.77**) show almost similar behavior as **Complex 11** ($[Fe(L^{12})_2](BF_4)_2.H_2O$), and may be similarly explained.

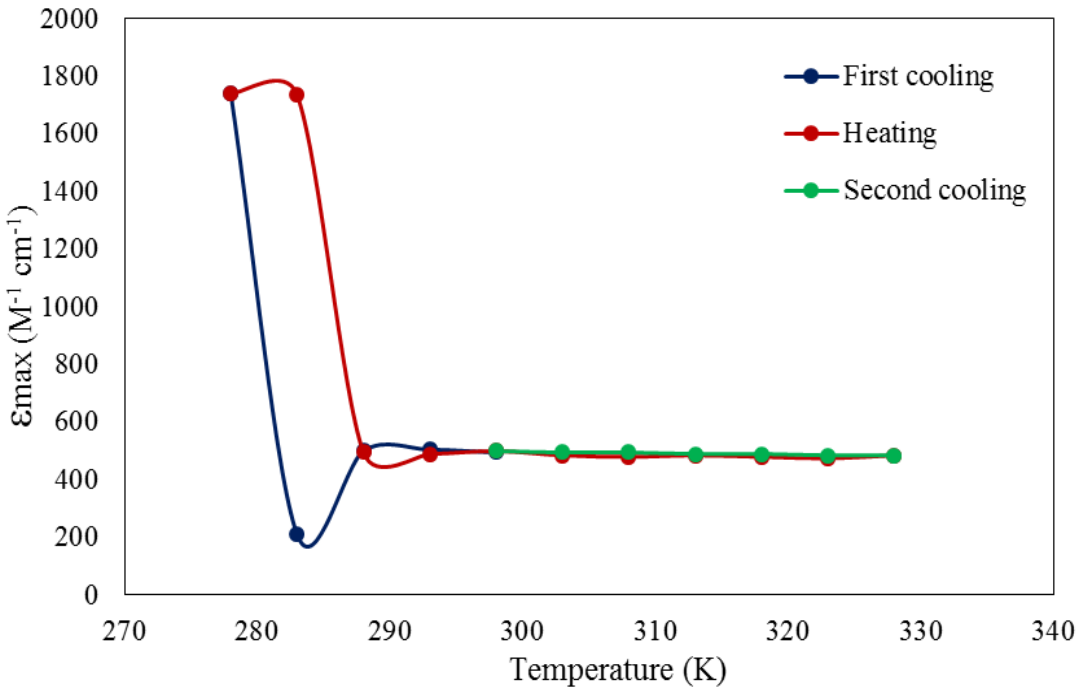

Figure 4.77 Temperature-dependence of ε_{max} values for **Complex 12** at 715 nm

(c) Thermal and mesomorphic properties

The **TGA** trace of **Complex 12** (**Figure 4.78**) shows a total weight loss of 92.4% in the temperature range 190 - 638 °C due to loss of two BF_3 molecules and two L^{16} ligands (expected, 93.3%). The amount of residue at temperatures above 638 °C was 7.6%, which is in good agreement with the expected amount of 6.7% (assuming pure FeF_2).

Hence, its decomposition temperature was lower compared to **Complex 6** ($[Co(L^{16})_2](BF_4)_2.H_2O$, T_{dec} = 245 °C). The results seem to suggest that Fe(II) ion caused a reduction in the thermal stability of these complexes compared to Co(II) ion.

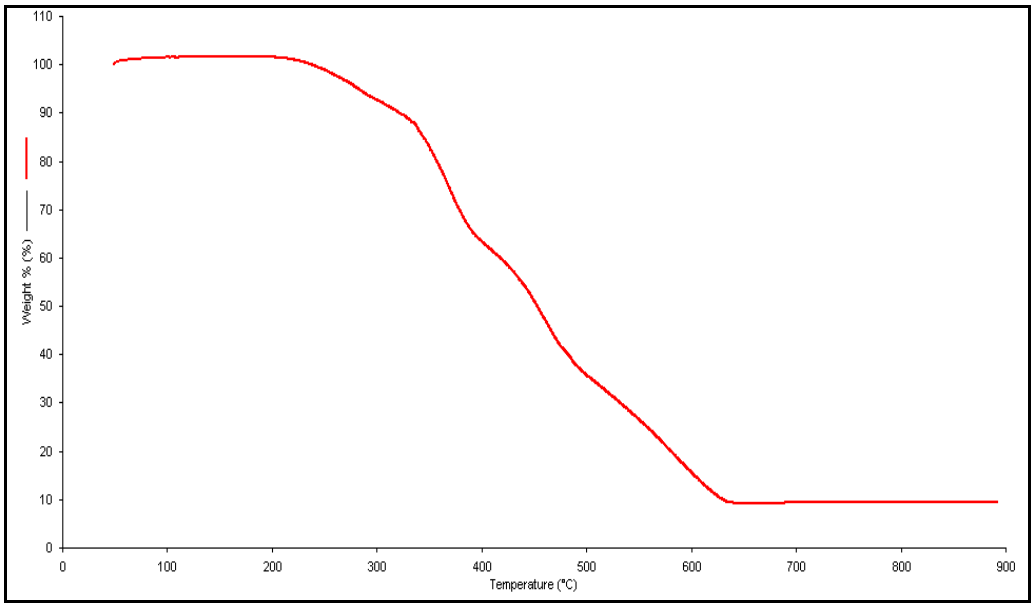

Figure 4.78 TGA trace of **Complex 12**

Its **DSC** scan (**Figure 4.79a** and **4.79b**) was performed on two heating-cooling cycles, in the temperature range from 25 – 150 °C. The data and assignment were collected in **Table 4.23**.

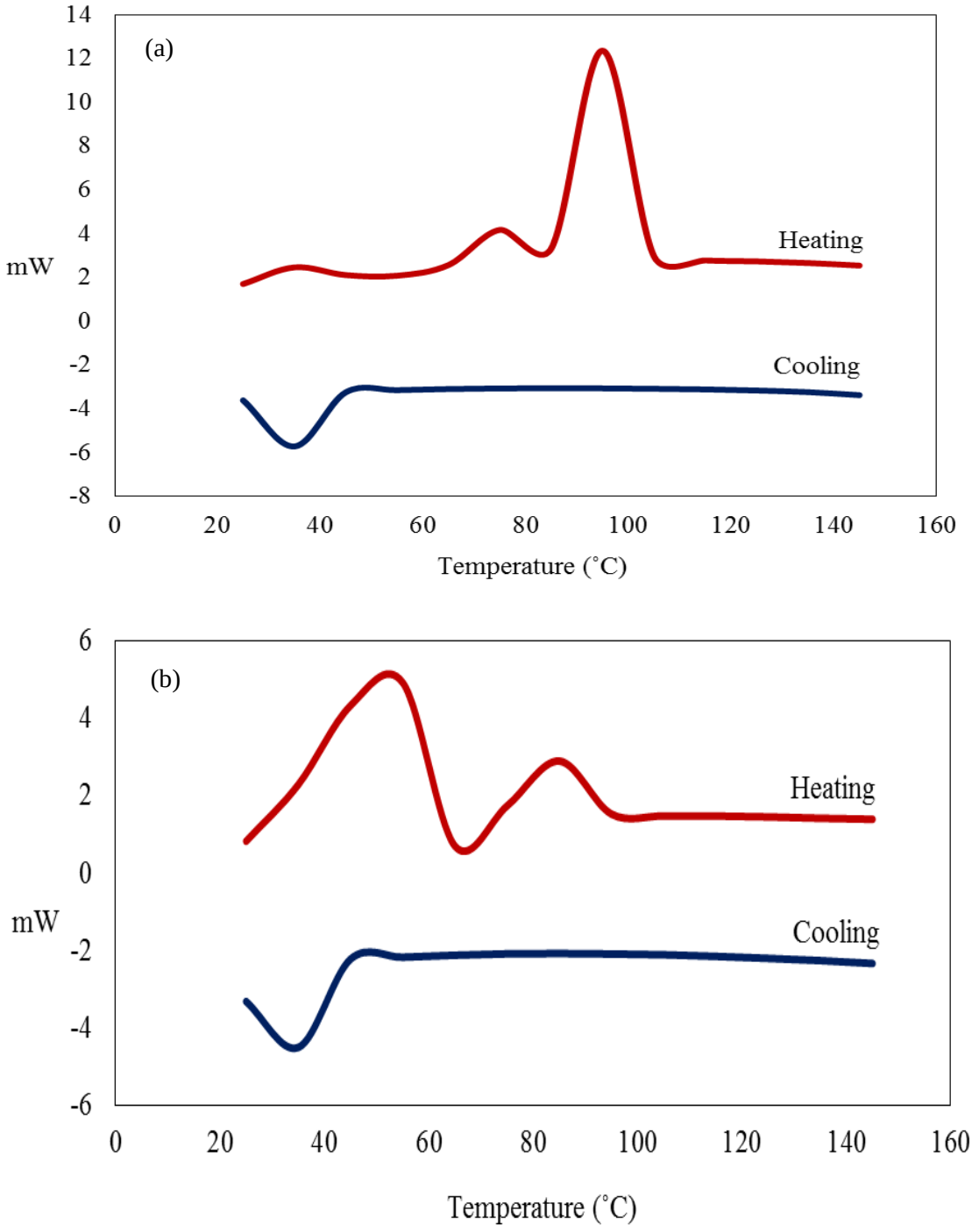

Figure 4.79 DSC of **Complex 12**: (a) first cycle; (b) second cycle. Endothermic peak up

Table 4.23 DSC data for **Complex 12** (M = mesophase)

Cycle		**Temperature (˚C)**	**ΔH (kJ mol^{-1})**	**Assignment**
1	Heating	62.6	+16.0	Cr-Cr transition
		89.6	+94.1	Melting temperature
	Cooling	44.5	-54.1	Recrystallization temperature
2	Heating	44.6	+79.2	Cr-M transition
		71.5	+22.9	M-M' transition
	Cooling	43.3	-32.2	Recrystallization temperature

Viewed under **POM** (**Figure 4.80**), **Complex 12** was observed to melt at about 89 °C and to clear at 199°C. On cooling from the isotropic liquid, it developed a focal conic texture at 124 °C [18]. The texture slowly disappeared on reheating from this temperature to its clearing temperature, but reformed at a lower temperature of 110 °C on cooling. However, on reheating, a different texture (fan-shape) formed at 124 °C, which transformed to another texture at 127 °C. On cooling, this texture changed back to the fan-shape at 124 °C, and then to the feather-like texture at 106 °C. These textures were assigned as *Col* mesophase. The different textures formed during the first and second heating-cooling cycles may arise from structural changes and/or dissociation when the complex was heated.

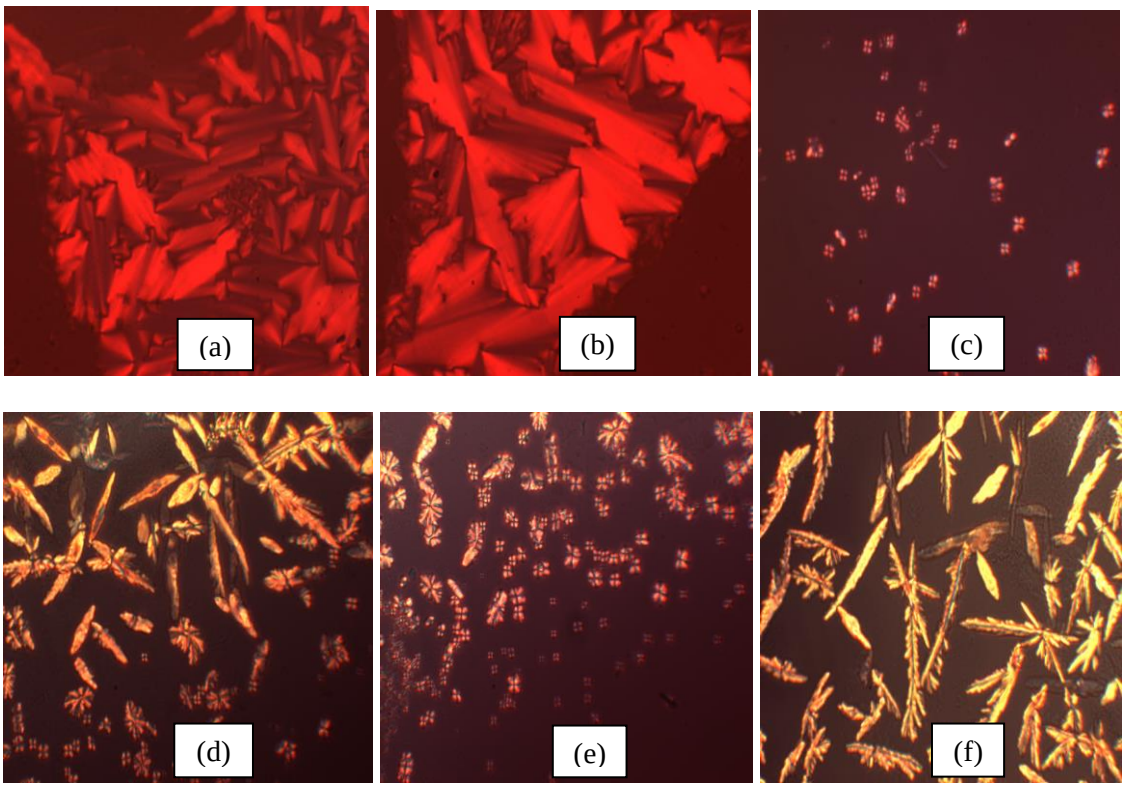

Figure 4.80 Photomicrographs of **Complex 12** on: (a) heating at 125 °C; (b) cooling at 110°C; (c) maintain at 124 °C; (d) heating at 127 °C; (e) cooling at 124 °C (f) cooling at 106 °C

4.5.4 Summary

The experimental data for $[Fe(L^n)_2](BF_4)_2$ are summarized in **Table 4.24**. Several general points are similar to previously discussed complexes, namely: (a) formed octahedral LS complexes, and except for **Complex 11**, were hydrated; (b) the decomposition temperatures were lower than the corresponding Co(II) complexes except for **Complex 10**; and (c) exhibited liquid crystal properties.

Table 4.24 Summary for **Complexes 10-12**

Complex	**10**	**11**	**12**
Structural formula	$[Fe(L^{6})_2](BF_4)_2$	$[Fe(L^{12})_2](BF_4)_2.H_2O$	$[Fe(L^{16})_2](BF_4)_2$
λ_{max}/nm (ε_{max}/M^{-1} cm^{-1})	721 (560)	721 (510)	721 (470)
T_{dec}/°C	225	242	190
$\chi_M T$ (cm^3 K mol^{-1}) (spin state)	0.17 (5.6% HS; 94.4% LS)	0.31 (10.3% HS; 89.7% LS)	0.27 (9.0% HS; 91.0% LS)
Liquid crystal mesophase	*Col*	*Col*	*Col*

4.6 $[Fe(L^6)_2]X_2$

The final phase of this research was to compare the effect of anions, namely ClO_4^- and PF_6^- ion on the structure, spin crossover behaviour, thermal, and mesogenic properties of $[Fe(L^6)_2]X_2$. These anions are bigger than BF_4^- ion, with the following order of increasing size: BF_4^-, ClO_4^-, PF_6^-.

4.6.1 $[Fe(L^6)_2](ClO_4)_2$

2,6-Pyridinedicarboxaldehyde, 1-aminohexane and $Fe(ClO_4)_2.6H_2O$ reacted in methanol to form a dark purple powder (**Complex 13**) with 52.1% yield. The powder was readily soluble in solvents similar to previously discussed complexes.

(a) Deduction of structural formula

The proposed structure of **Complex 13** was similar to previously discussed complexes, based on the same instrumental analyses presented below.

The results of **elemental analyses** for carbon, hydrogen and nitrogen (**Table 4.25**) are in excellent agreement with those calculated for chemical formula $[Fe(L^6)_2](ClO_4)_2$ ($C_{38}H_{62}Cl_2FeN_6O_8$; formula weight 856.80 g mol^{-1}).

Table 4.25 Elemental analytical data for **Complex 13**

Element	(%)	
	Calculated	**Found**
Carbon	53.21	53.50
Hydrogen	7.29	7.30
Nitrogen	9.80	9.75

Its **ESI-MS** spectrum (**Figure 4.81**) shows peaks at m/z 757.4 for $\{[Fe(L^6)_2](ClO_4)\}^+$ (calculated,757.4), and 329.7 assigned for $[Fe(L^6)_2]^{2+}$ ion (calculated, 329.2).

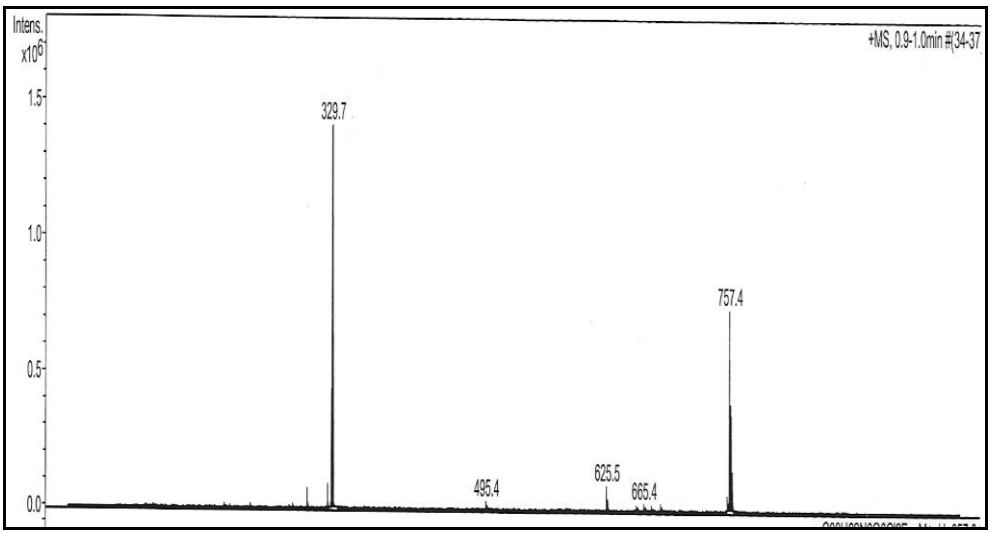

Figure 4.81 ESI-MS of **Complex 13**

Its **FTIR** spectrum (**Figure 4.82**) peaks at 2933 cm^{-1}, 2870 cm^{-1}, 1581 cm^{-1}, 1087 cm^{-1}, 935 cm^{-1} and 622 cm^{-1}.These peaks may be similarly assigned as for **Complexes 7** ($[Co(L^{12})_2](ClO_4)_2$) and **8** ($[Co(L^{16})_2](ClO_4)_2$).

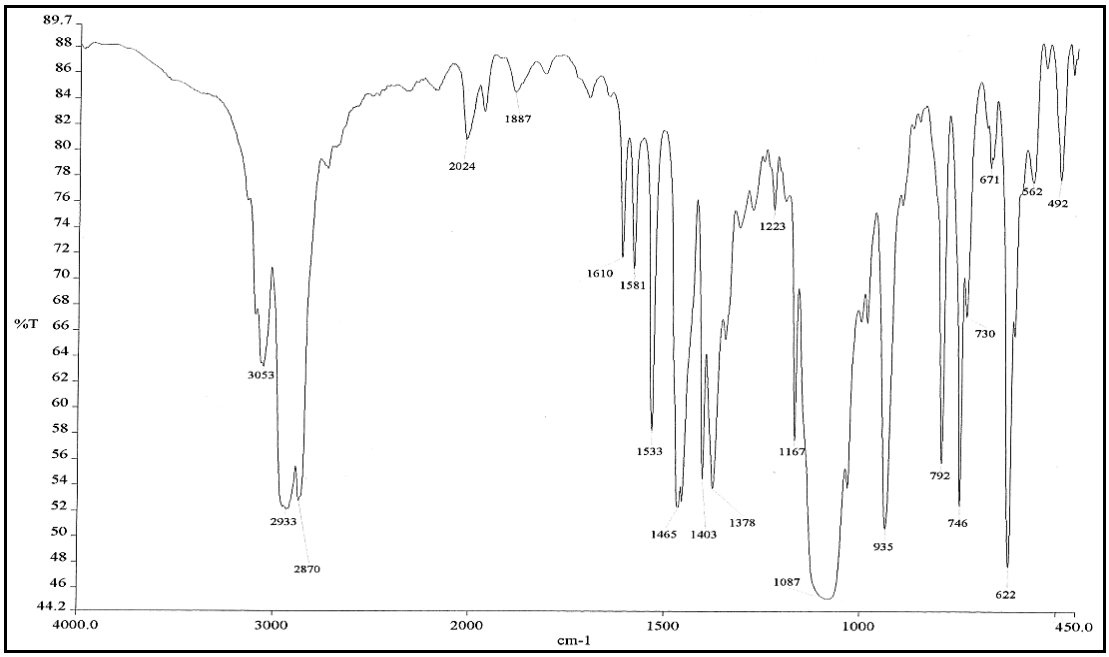

Figure 4.82 FTIR spectrum for **Complex 13**

Its **UV-visible** spectrum in $CHCl_3$ (**Figure 4.83**) shows a broad *d-d* band at 723 nm (ε, 390 M^{-1} cm^{-1}), and CT bands at 597 nm (ε, 7440 M^{-1} cm^{-1}), 574 nm (ε, 5880 M^{-1} cm^{-1}), 476 nm (ε, 5440 M^{-1} cm^{-1}). These electronic transitions may be

similarly assigned as for **Complexes 10** ($[Fe(L^6)_2](BF_4)_2$), **11** ($[Fe(L^{12})_2](BF_4)_2$), and **12** ($[Fe(L^{16})_2](BF_4)_2$).

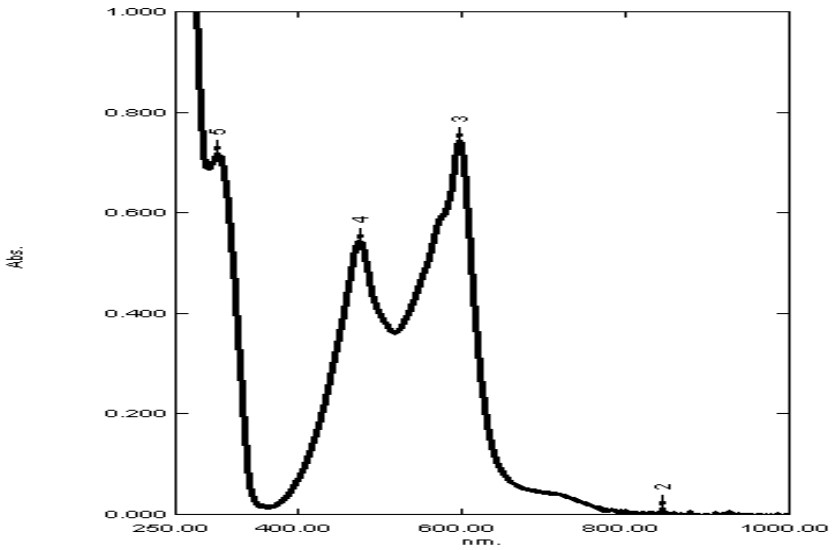

Figure 4.83 UV-visible spectrum of **Complex 13**

The powder formed thick needle-like dark purple crystals when it was dissolved in methanol followed by slow diffusion of diethyl ether. The single crystal **X-ray crystallography** of the needles (**Figure 4.84**) shows that the complex crystallized in the monoclinic system, $P2_1/n$ unit cells and that the iron(II) ion in $[Fe(L^6)_2]^{2+}$ was in an octahedral geometry, while the two ClO_4^- ions were not coordinated. Hence, its structure is similar to **Complex 4** ($[Co(L^{12})_2](BF_4)_2$). The packing pattern is shown on **Figure 4.85**.

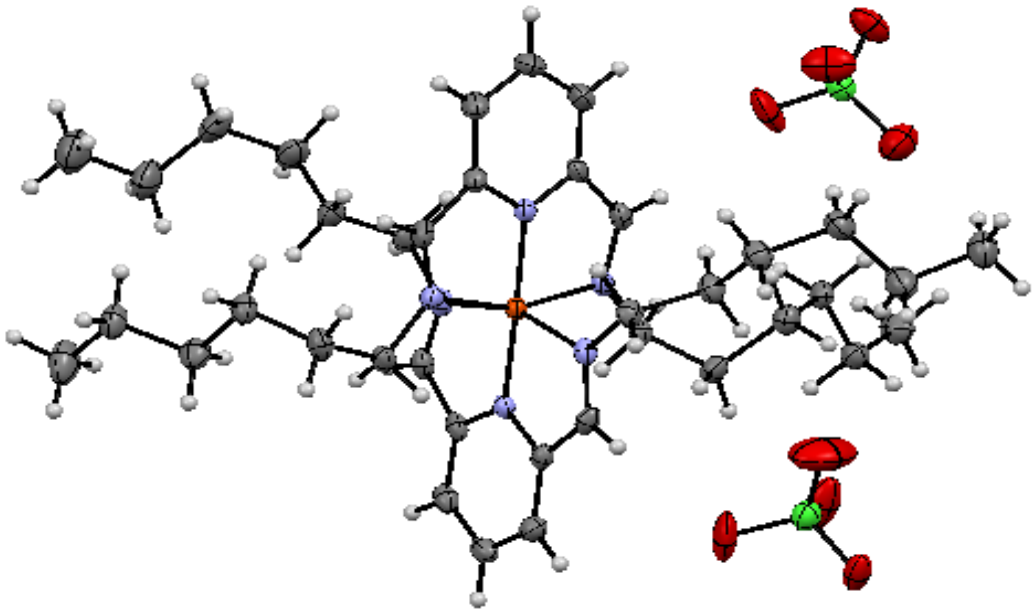

Figure 4.84 an ORTEP presentation of **Complex 13**

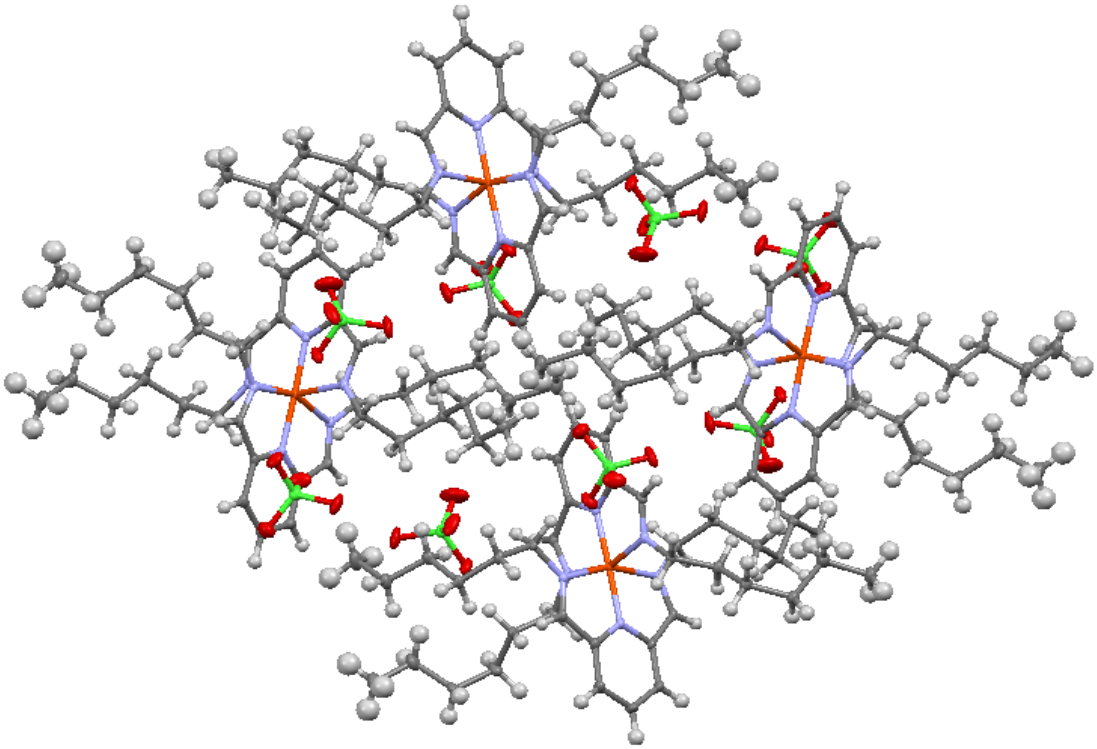

Figure 4.85 The packing pattern of **Complex 13**, viewed along the crystallographic *c*-direction rotated 90º at z-axis

The crystal data and structure refinement of **Complex 13** are shown in **Table 4.26**, while the selected bond lengths and bond angles data are shown in **Table 4.27**.

Table 4.26 Crystallography and refinement details of **Complex 13**

Empirical formula	$C_{38}H_{62}FeN_6ClO_8$
Formula weight	857.69
Temperature	150 K
Wavelength	0.71073 Å
Crystal system, space group	Monoclinic, $P2_1/n$
Unit cell dimension	a = 14.4640(9) Å α = 90˚ b = 18.9601(10) Å β = 111.607(2)˚ c = 16.6186(10) Å γ = 90˚
Volume	4237.2(4) A^3
Z, Calculated density	4, 1.344 g/cm^3
Absorption coefficient	0.538 mm^{-1}
F(000)	1824
Crystal size	0.08 x 0.16 x 0.45 mm
θ range for data collection	1.6, 26.4˚
Limiting indices (±*h*, ±*k*, ±*l*)	-18/12, -23/16, -19/20
Reflections collected / unique	48908 / 8291 [R_{int} = 0.066]
Absorption correction	None
Data / restrains / parameters	8291 / 500 /
Goodness-of-fit on F^2	1.08
Final R indices [I > 2σ(I)]	R1 = 0.0620, wR2 = 0.1455
$\Delta\rho_{max}$ and $\Delta\rho_{min}$	0.78 and -0.48 e $Å^{-3}$

Table 4.27 Selected bond lengths [Å] of **Complex 13**

Fe1 − N2	1.868(3)	N2 − C3	1.354(5)
Fe1 – N9	1.982(3)	N9 – C8	1.292(5)
Fe1 – N17	1.975(3)	N17 – C18	1.475(5)
Fe1 – N24	1.875(3)	N24 – C29	1.356(5)
Fe1 – N31	1.976(3)	N31 – C30	1.297(5)
Fe1 – N39	1.983(3)	N39 – C38	1.291(5)

(b) Spin-crossover behavior

The $\chi_M^{corr}T$ value for **Complex 13**, calculated from its proposed chemical formula (FW = 856.80 g mol^{-1}), χ_g (-0.04 x 10^{-5} cm^3 g^{-1}), χ_M (-3.43 x 10^{-4} cm^3 mol^{-1}), χ_{dia} (-454.48 x 10^{-6} cm^3 mol^{-1}) and χ_M^{corr} (1.11 x 10^{-4} cm^3 mol^{-1}), was 0.03 cm^3 K mol^{-1} at 293 K. Thus this complex was made up of 1.0% HS and 99.0% LS Fe(II) at room temperature. The result suggests insignificant effect of the size of the anion on the spin state of the complexes.

Its **temperature-dependence** ε_{max} values were similarly measured as for **Complex 10 (**$[Fe(L^6)_2](BF_4)_2$). Except for the absence of 'hysteresis loop' for **Complex 13,** the results (**Figure 4.86**) for both complexes were almost similar.

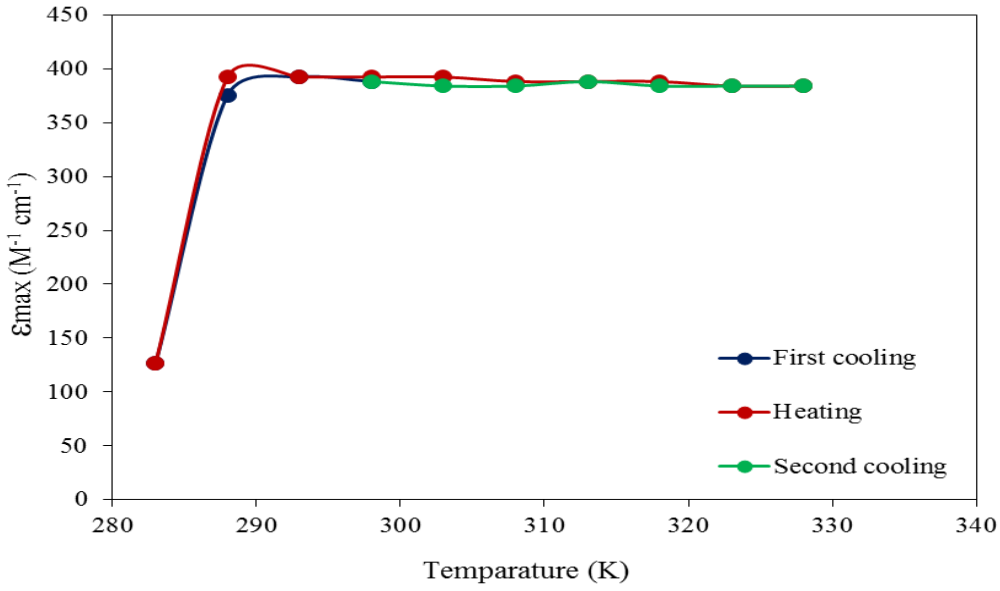

Figure 4.86 Temperature-dependence of ε_{max} values for **Complex 13** at 722 nm

(c) Thermal and mesomorphic properties

The TGA scan was not done for **Complex 13** as a precautionary measure since complexes with ClO_4^- ion may explode on heating.

Complex 13 did not show any optical textures when viewed under POM. Hence, it did not exhibit liquid crystal properties.

4.6.2 $[Fe(L^6)_2](PF_6)_2$

2,6-Pyridinedicarboxaldehyde, 1-aminohexane, $(NH_4)(PF_6)$ and $FeCl_2.4H_2O$ reacted in methanol to form a dark purple powder (**Complex 14**) in good yield (84.7%). The powder was readily soluble in solvents similar to **Complexes 1-13**.

(a) Deduction of structural formula

Based on the same instrumental analyses as previously discussed, it is proposed that the structure of **Complex 14** was similar to those of previously discussed complexes.

The results of **elemental analyses** for carbon, hydrogen and nitrogen (**Table 4.28**) are in excellent agreement with those calculated for chemical formula $[Fe(L^6)_2](PF_6)_2$ ($C_{38}H_{62}F_{12}FeN_6P_2$; formula weight 947.90 g mol^{-1}).

Table 4.28 Elemental analytical data for **Complex 14**

Element	**(%)**	
	Calculated	**Found**
Carbon	48.11	47.75
Hydrogen	6.59	6.55
Nitrogen	8.86	8.85

Its **ESI-MS** spectrum (**Figure 4.87**) shows peaks at m/z 807.4 for $\{[Fe(L^6)_2](PF_6)\}^+$ ion (calculated, 803.4), and 329.2 for $[Fe(L^6)_2]^{2+}$ ion (calculated, 329.2).

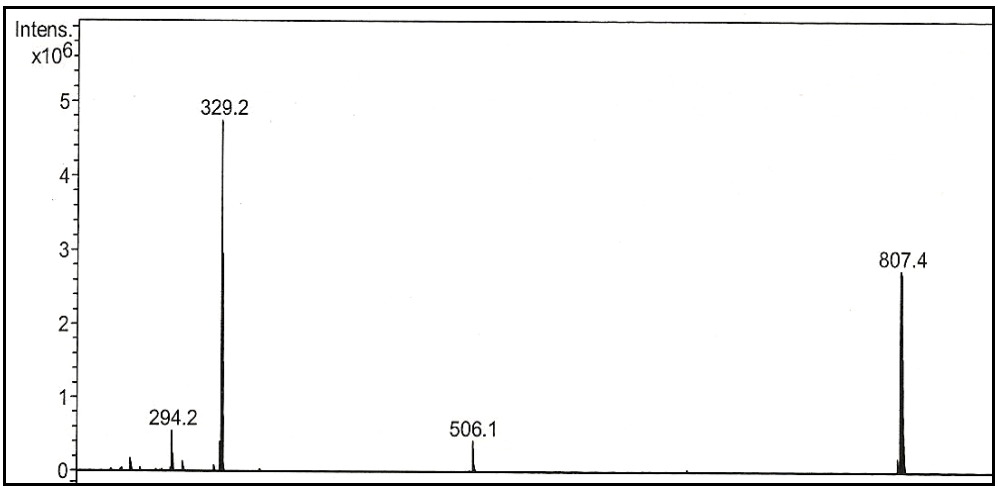

Figure 4.87 ESI-MS of **Complex 14**

Its **FTIR** spectrum (**Figure 4.88**) shows peaks at 2929 cm^{-1}, 2864 cm^{-1}, 1534 cm^{-1}, and 826 cm^{-1}. These peaks may be similarly assigned as for **Complex 9** ($[Co(L^6)_2](PF_6)_2$).

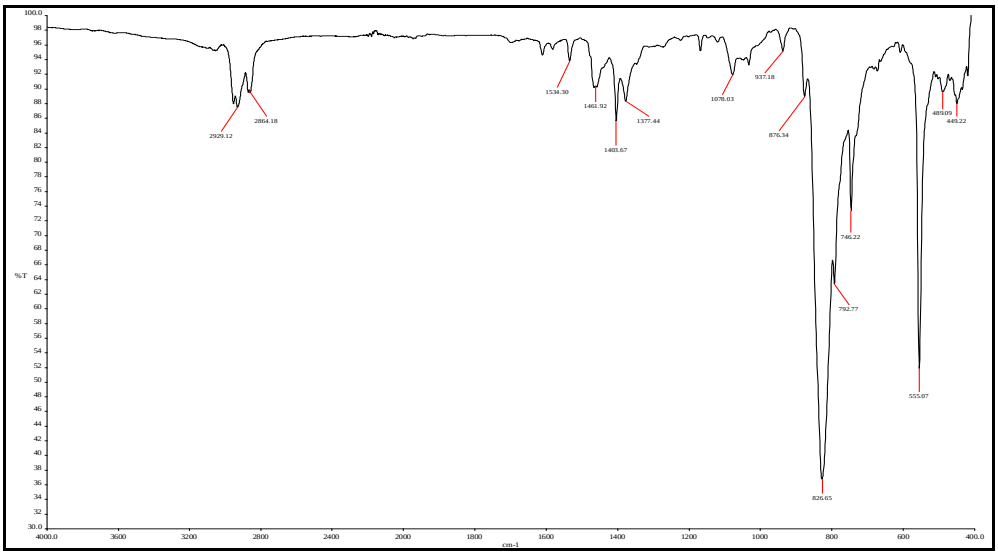

Figure 4.88 FTIR spectrum of **Complex 14**

Its **UV-visible** spectrum in chloroform (**Figure 4.89**) shows a broad *d-d* band at 715 nm (ε, 354 M^{-1} cm^{-1}), and CT bands 597 nm (ε, 5496 M^{-1} cm^{-1}), 572 nm (ε, 4276 M^{-1} cm^{-1}) and 474 nm (ε, 4064 M^{-1} cm^{-1}). These electronic transitions may be assigned similarly as for **Complexes 10** ($[Fe(L^6)_2](BF_4)_2$), **11** ($[Fe(L^{12})_2](BF_4)_2$), and **12** ($[Fe(L^{16})_2](BF_4)_2$).

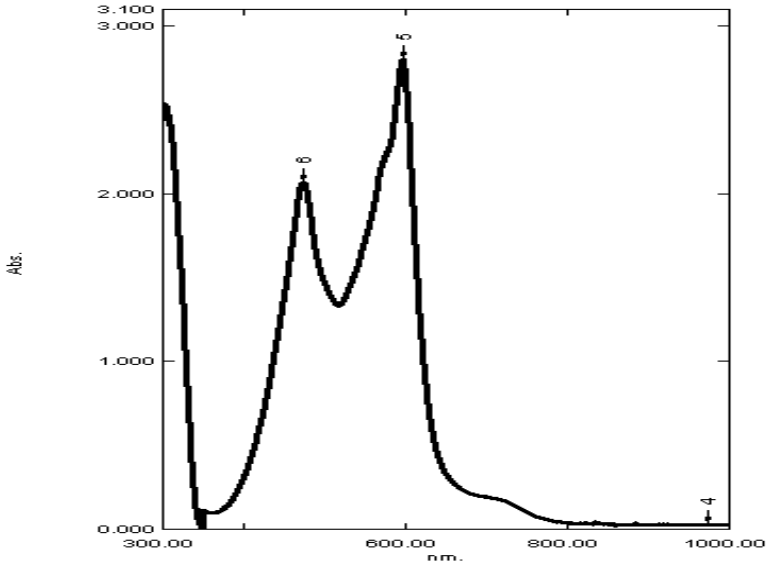

Figure 4.89 UV-visible spectrum of **Complex 14**

(b) Spin-crossover behavior

The $\chi_M^{corr}T$ value for **Complex 14**, calculated from its proposed chemical formula (FW = 947.90 g mol^{-1}), χ_g (2.40 x 10^{-7} cm^3 g^{-1}), χ_M (2.27 x 10^{-4} cm^3 mol^{-1}), χ_{dia} (-454.48 x 10^{-6} cm^3 mol^{-1}) and χ_M^{corr} (6.81 x 10^{-4} cm^3 mol^{-1}), was 0.20 cm^3 K mol^{-1} at 298 K. Thus, **Complex 14** was made up of 6.8% HS and 93.2% LS Fe(II) at room temperature. The result further supports the above suggestion that size of the anion did not have a significant effect on the spin state of these complexes.

Its **temperature-dependence ε_{max}** values were similarly measured as **Complex 13** ($[Fe(L^6)_2](ClO_4)_2$. The results (**Figure 4.90**) show that on heating, the ε_{max} values remained almost unchanged at about 360 M^{-1} cm^{-1} from 298 K to 328 K, and then decreased abruption to about 170 M^{-1} cm^{-1} at 343 K. Upon cooling from this temperature, the values remained almost unchanged at 170 M^{-1} cm^{-1} and increased abruption back to about 330 M^{-1} cm^{-1} at 293 K. From these results, it may be inferred that **Complex 14** showed a normal and reversible SCO behavior.

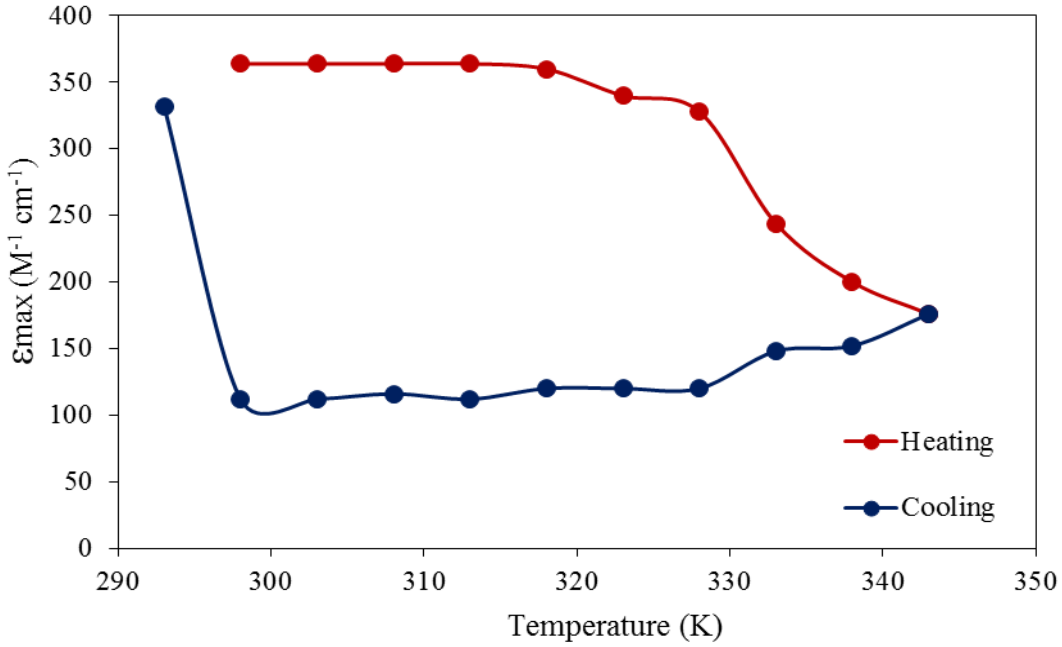

Figure 4.90 Temperature-dependence of ε_{max} values for **Complex 15** at 718 nm

(c) Thermal and mesogenic properties

The **TGA** trace of **Complex 14** (**Figure 4.91**) shows that complex suffered a total weight loss of 85.0% in the temperature range 204 - 848 °C due to loss of two PF_5 molecules and two L^6 ligands (expected, 90.1%). The amount of residue at temperatures above 850 °C was 15.0%, which is in good agreement with the expected amount of 9.9% (assuming pure FeF_2). Its decomposition temperature was almost similar to **Complex 9** ($[Co(L^6)_2](PF_6)_2$, T_{dec} = 211 °C).

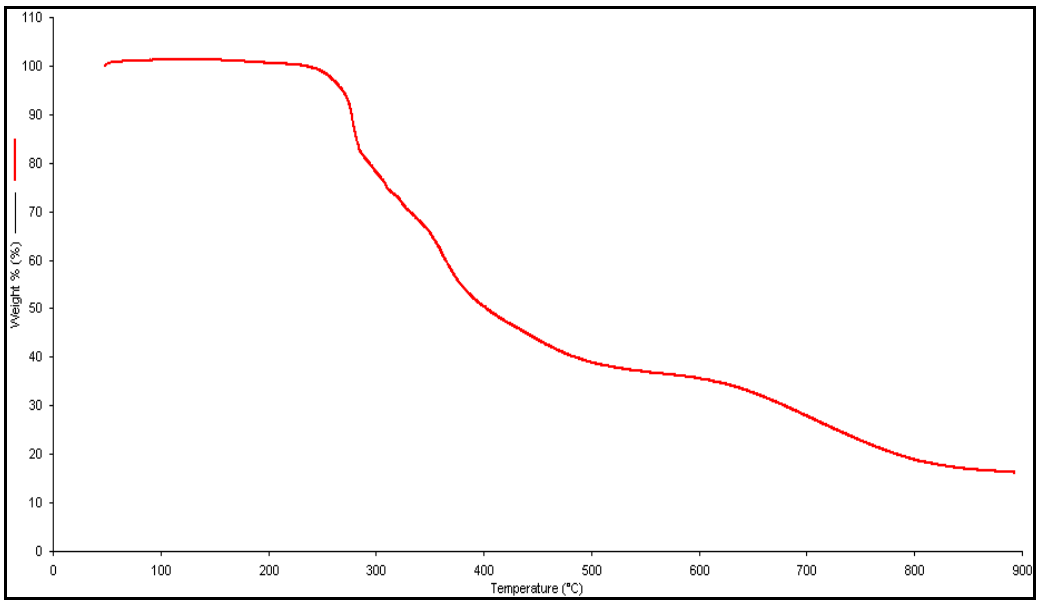

Figure 4.91 TGA trace of **Complex 14**

Complex 14 did not show any optical textures when viewed under POM. Hence, it did not exhibit liquid crystal properties.

4.6.3 Summary

The experimental data for $[Fe(L^6)_2]X_2$ (**Complexes 13** and **14**) are summarized in **Table 4.29**. Several general points for both complexes: (a) formed octahedral complexes with predominantly LS state; (b) did not exhibit liquid crystal properties.

Table 4.29 Summary for **Complexes 13** and **14**

Complex	**13**	**14**
Structural formula	$[Fe(L^6)_2](ClO_4)_2$	$Fe(L^6)_2(PF_6)_2$
λ_{max}/nm (ε_{max}/M^{-1} cm^{-1})	723 (390)	715 (354)
T_{dec}/°C	Not determined	204
$\chi_M T$ (cm^3 K mol^{-1})	0.03 (1.0% HS; 99.0% LS)	0.20 (6.8% HS; 93.2% LS)
Liquid crystal properties	Not mesogenic	Not mesogenic

References

[1] Y. Komatsu, K. Kato, Y. Yamamoto, H. Kamihata, Y. H. Lee, A. Fuyuhiro, S. Kawata and S. Hayami, *Eur. J. Inorg. Chem.*, vol. 2012, pp. 2769-2775, 2012.

[2] S.-T. M. Joobeom Seo, Jineun Kim, Shim Sung Lee, Ki-Min Park, *Bull. Korean Chem. Soc.*, vol. 24, pp. 1393-1395, 2003.

[3] A. B. P. Lever, *J. Chem. Educ.*, vol. 51, pp. 612-616, 1974.

[4] C. Enachescu, I. Krivokapic, M. Zerara, J. A. Real, N. Amstutz, and A. Hauser, *Inorg. Chim. Acta*, vol. 360, pp. 3945-3950, 2007.

[5] O. Kahn, *Molecular Magnetism*. New York: VCS Publishers Inc., 1993.

[6] R. Hogg and R. G. Wilkins, *J. Chem. Soc. (Resumed)*, pp. 341-350, 1962.

[7] J. S. Judge and W. A. Baker Jr, *Inorg. Chim. Acta*, vol. 1, pp. 68-72,1967.

[8] C.-W. Chien, K.-T. Liu, and C. K. Lai, *J. Mater. Chem.*, vol. 13, p. 1588, 2003.

[9] N. Maringa, J. Lenoble, B. Donnio, D. Guillon, and R. Deschenaux, *J. Mater. Chem.*, vol. 18, p. 1524, 2008.

[10] Y. Chen, Y.-H. Zhang, and L.-J. Zhao, *Phys. Chem. Chem. Phys.*, vol. 6, pp. 537-542, 2004.

[11] R. Clérac, M. Fourmigué, J. Gaultier, Y. Barrans, P. A. Albouy, and C. Coulon, *Eur. Phys. J. B - Condensed Matter and Complex Systems*, vol. 9, pp. 431-443, 1999/06/01 1999.

[12] P. Gütlich, A. B. Gaspar, and Y. Garcia, *Beilstein J. Org. Chem.*, vol. 9, pp. 342-391, 2013.

[13] T. Kizaki, T. Matsumoto, and S. Ogo, *Dalton Trans.*, vol. 39, pp. 1339-1344, 2010.

[14] G. Brehm, M. Reiher, and S. Schneider, *J. Phys. Chem. A*, vol. 106, pp. 12024-12034, 2002/12/01 2002.

[15] P. Gütlich, Y. Garcia, and H. Spiering, "Spin Transition Phenomena," in *Magnetism: Molecules to Materials IV*, ed: Wiley-VCH Verlag GmbH & Co. KGaA, 2003, pp. 271-344.

[16] Z. Wang, Y. Lan, K. Zhong, Y. Liang, T. Chen, and L. Y. Jin, *Int. J. Mol. Sci*, vol. 15, pp. 5634-48, 2014.

[17] T. Cardinaels, J. Ramaekers, P. Nockemann, K. Driesen, K. Van Hecke, L. Van Meervelt, *et al.*, *Soft Matter*, vol. 4, p. 2172, 2008.

[18] R. J. Bushby, N. Boden, C. A. Kilner, O. R. Lozman, Z. Lu, Q. Liu, *et al.*, *J. Mater. Chem.*, vol. 13, pp. 470-474, 2003.